FACULTY
OF MATHEMATICS
AND PHYSICS
Charles University

MASTER'S THESIS

Matěj Makeš

Mapping of Changes in Optical and Magneto-Optical Responses of Ni-Mn-Ga Thin Films across Martensitic Transformation and Strain Relaxation

Institute of Physics of Charles University

Supervisor of the master's thesis: RNDr. Martin Veis, Ph.D.
Study programme: Optics and optoelectronics
Study branch: FOOP

Prague 2024

I declare that I carried out this master's thesis independently and only with the cited sources, literature and other professional sources. It has not been used to obtain another or the same degree. I understand that my work relates to the rights and obligations under Act No. 121/2000 Coll., the Copyright Act, as amended, in particular, the fact that the Charles University has the right to conclude a license agreement on the use of this work as a school work pursuant to Section 60 Subsection 1 of the Copyright Act.

In .... date ....

Author's signature

First and foremost, I would like to thank my supervisor Martin Veis for his guidance and advice. Next, I thank Jakub Zázvorka for providing me with the thin film samples studied in this thesis, Carlos Verbeno for the magnetometry data and Oleg Heczko for the XRD out-of-plane lattice parameter measurements and a fruitful discussion concerning Ni-Mn-Ga. I am deeply grateful to Michal Vančík and Tomáš Maleček for their help with the experimental setup, my sister Bára for proofreading the text and Alexandra Elbakyan without whom I could not have accessed several key pieces of information. My gratitude also belongs to my friends and family for their support during my studies.

Title: Mapping of Changes in Optical and Magneto-Optical Responses of Ni-Mn-Ga Thin Films across Martensitic Transformation and Strain Relaxation

Author: Matěj Makeš

Institute: Institute of Physics of Charles University

Supervisor: RNDr. Martin Veis, Ph.D., Institute of Physics of Charles University

Abstract: This thesis studies optical and magneto-optical responses of thin epitaxial Ni-Mn-Ga films prepared by magnetron sputtering. The relative permittivity tensor spectra were computed from the spectroscopic ellipsometry data measured both without the external magnetic field and in the out-of-plane magnetic field configuration. For one of the thin film samples, measurements across martensitic transformation were performed and temperature-hysteresis was observed. The analysis of the obtained spectra for thickness-varied series of samples clearly demonstrated the influence of substrate-induced strain and revealed a strong correlation between the out-of-plane lattice parameter and the properties of the obtained spectra.

Keywords: epitaxial films, Ni-Mn-Ga, Heusler alloy, martensitic transformation, strain relaxation, spectroscopic ellipsometry, polar magneto-optical Kerr effect

Contents

Introduction

Since the first observation of a large 0.2 % magnetic-field-induced strain in unstressed Ni_2MnGa single crystals (Ullakko et al., 1996) associated with the superelastic motion of twin boundaries in the martensitic phase, this material has become the subject of intense study for its attractive application possibilities (Miyazaki et al., 2009) in micro-mechanical devices like micro-actuators or micro-pumps. Structural transformations in Ni-Mn-Ga alloys are yet to be fully understood. Therefore, we employ optical and magneto-optical spectroscopies that provide direct insight into the electronic structure. An overview of this material is provided in Chapter 1.

In Chapter 2, we derive a linear optical response of originally isotropic solids that are magnetized in the direction of an external static homogeneous magnetic field from symmetry arguments and microscopic models, using both classical and semiclassical theories.

In Chapter 3, we describe polarization states of fully polarized light (idealized as an ensemble of non-interacting transverse monochromatic plane waves), its parameters and how it is transformed by optical systems.

Chapter 4 serves as an introduction to ellipsometry, which is an optical technique (Azzam and Bashara, 1977, p. v) based on exploiting the polarization changes of the light that is reflected from or transmitted through the studied sample. With the invention of computers, allowing for an effective implementation of theoretical models to obtain material properties via regression analysis, it proved itself as a powerful non-invasive tool for material characterization. At the beginning of the chapter, ellipsometric parameters are defined, and their relationships to specific polarization changes are explained. Then, after an overview of common ellipsometer configurations, it is demonstrated how the ellipsometric parameters can be obtained in practice from intensity measurements. At the end of the chapter, for the simplest cases of optical systems, we will demonstrate how to analyze the ellipsometric data via basic theoretical models to gain information about the system properties.

In Chapter 5, these theoretical models are expanded to a stratified structure consisting of $\mathcal{N}$ homogeneous layers with plane-parallel boundaries. A 4×4 matrix formalism arising from the boundary conditions yields the theoretical values of generalized ellipsometric parameters that are compared to the experimental ones in order to obtain the off-diagonal relative permittivity tensor element spectra via regression analysis.

Chapter 6 summarizes the data collection processes, leading to the relative permittivity tensor spectra of the Ni-Mn-Ga layer in our samples. It also specifies what assumptions were made and what laboratory equipment was used.

Finally, in Chapter 7, we present our experimental results on thin epitaxial Ni-Mn-Ga films, prepared by magnetron sputtering and deposited on the Cr layer and the MgO substrate. In the first part, the analysis is focused on the spectral changes induced by the martensitic transformation, and in the second part, we analyze the spectral changes with respect to thickness variation and strain relaxation at room temperature.

1. Ni-Mn-Ga

1.1 Crystallographic structure

Ni-Mn-Ga (or NMG for short) is a ternary intermetallic alloy. Stoichiometric Ni_2MnGa is a full-Heusler alloy (Felser and Hirohata, 2015). High resolution neutron powder diffraction measurements (Brown et al., 2002) showed that its austenitic high-temperature phase (400 K–260 K) has a cubic $L2_1$ structure, belonging to the space group $Fm\bar{3}m$ (see Fig. 1.1a). Upon cooling, at $T_P \approx 260\,\mathrm{K}$ and $T_M \approx 200\,\mathrm{K}$, respectively, a pre-martensitic 6M and martensitic 14M phases with orthorhombic super-cells (see Fig. 1.2), belonging to the space group Pnnm, form. These low-temperature orthorhombic phases exhibit displacive modulation along the $[1\bar{1}0]_{\mathrm{cubic}}$ direction with 6 and 14 atomic planes $(110)_{\mathrm{cubic}}$ periods, respectively. Their lattice parameters were found to be: $a_{\mathrm{cubic}} = 5.822\,\mathrm{\mathring{A}}$, the cell parameter of the cubic phase at room temperature (300 K), $a_{\mathrm{ortho6M}} = a_{\mathrm{cubic}}/\sqrt{2}$, $b_{\mathrm{ortho6M}} = (3/\sqrt{2})a_{\mathrm{cubic}}$, $c_{\mathrm{ortho6M}} = a_{\mathrm{cubic}}$, the super-cell parameters of the 6M orthorhombic phase and $a_{\mathrm{ortho14M}} = a_{\mathrm{cubic}}/\sqrt{2}$, $b_{\mathrm{ortho14M}} = (7/\sqrt{2})a_{\mathrm{cubic}}$, $c_{\mathrm{ortho14M}} = a_{\mathrm{cubic}}$, the super-cell parameters of the 14M orthorhombic phase. The lattice parameters of the marked variants in Fig. 1.2 are geometrically related as follows: $a_{\mathrm{ortho6M}} \parallel a_{\mathrm{ortho14M}} \parallel [1\bar{1}0]_{\mathrm{cubic}}$, $b_{\mathrm{ortho6M}} \parallel b_{\mathrm{ortho14M}} \parallel [110]_{\mathrm{cubic}}$ and $c_{\mathrm{ortho6M}} \parallel c_{\mathrm{ortho14M}} \parallel [001]_{\mathrm{cubic}}$.

X-Ray diffraction (XRD) measurements (Martynov and Kokorin, 1992) of a single Ni_2MnGa crystal in the temperature range from 308 K to 77 K showed orthorhombic 10M and 14M and tetragonal NM phases induced by stress in the $[110]_{\mathrm{cubic}}$ direction. These stress-induced phases were reported to be stable under the temperatures of 298 K, 233 K and 193 K, respectively.

Each phase has a different number of possible unit cell orientations that are called variants. A shape-memory effect (SME) is associated with the reversible nature of the thermoelastic martensitic transformation in shape-memory alloys (SMA). After being deformed by the martensite variant domain redistribution, these alloys are able to return to their original shape when heated back to the austenitic phase (Miyazaki et al., 2009, Ch. 2.1).

1.2 Magnetic properties

Ni_2MnGa single crystals gain a ferromagnetic ordering at a Curie temperature $T_C \approx 376\,\mathrm{K}$ (Webster et al., 1984). Magnetization measurements (Webster et al., 1984) as well as predictions (Kart et al., 2008) from density functional theory (DFT) indicate that the magnetic moment is located predominantly on the Mn sites, and its value was reported to be approx. $3.4\,\mu_{\mathrm{B}}$. A smaller magnetic moment of approx. $0.3\,\mu_{\mathrm{B}}$ per atom is located on Ni sites and even smaller, in the order of $-0.01\,\mu_{\mathrm{B}}$ per atom, is located on Ga sites. All in all, the total magnetic moment per unit cell is expected to be slightly over $4\,\mu_{\mathrm{B}}$.

Apart from the conventional SME, which is thermally-induced, ferromagnetic SMA also exhibits a magnetic shape-memory effect (MSME). Two underlying mechanisms of MSME, resulting in a reversible magnetic-field induced strain (MFIS), were identified (Heczko, 2014):

1. Magnetically-induced phase transformation happens due to the magnetization difference between the martensitic and austenitic phases. It can occur only if this difference is large, while transformation energy and thermal hysteresis are small. In practice, it can be accomplished at temperatures in the vicinity of T_M or in large magnetic fields.
2. Magnetically-induced reorientation (MIR) of martensitic variants originates in the coupling of the magnetization direction to a certain crystallographic direction or plane, i.e. the easy axis or plane of magnetization (e.g. the short axis of the tetragonal unit cell). On applying the external magnetic field, some variants have lower energy and grow at the expense of other less favorable variants.

MSME enables significantly higher switching frequencies than conventional thermally induced SMA. Therefore, ever since the first observation of a large MFIS of nearly 0.2 % in unstressed Ni_2MnGa by Ullakko et al. (1996), many studies followed with currently the highest MFIS of 12 % reported by Sozinov et al. (2013) in $Ni_{46}Mn_{24}Ga_{22}Co_4Cu_4$ (a magnetic field in the order of 1 T).

1.3 Electronic structure

In order to characterize the structural changes, *ab initio* calculations of the electronic structure were made (Entel et al., 2006). The theoretical total electronic densities of states (EDOS) for cubic and tetragonal phases (see Fig. 1.3) predict, above the Fermi energy E_F, two significant peaks of minority-spin states and practically no majority-spin states. Hence, we can expect dipole-forbidden electron transitions between minority-spin d-states. Expected transition energies for the cubic (austenitic) phase are approx. 2 eV, 3 eV, possibly even 1.6 eV (if we consider the small peak right below the Fermi energy and the highest peak above the Fermi energy). For the tetragonal (martensitic) phase, transitions are expected at approx. 1.8 eV and 2.8 eV. Furthermore, while the highest minority-spin EDOS peak below E_F has the same magnitude for both phases, the highest and the second highest minority-spin EDOS peaks above E_F are evidently different. Therefore, intensities of these transitions are also expected to change during the martensitic transformation.

1.4 Stoichiometry

A study by Chernenko et al. (1995) revealed a strong sensitivity of the Ni-Mn-Ga alloy to the stoichiometric composition. It was concluded that T_M increases with Ni excess at the expense of both Mn (this trend can be seen in Fig. 1.4) and Ga. At constant value of Ni content, it increases with Mn excess. In other words, T_M is increasing with increasing Ni to Ga content ratio. Besides T_M, composition affects other material properties such as thermal hysteresis, transformation heat, T_C and lattice parameter.

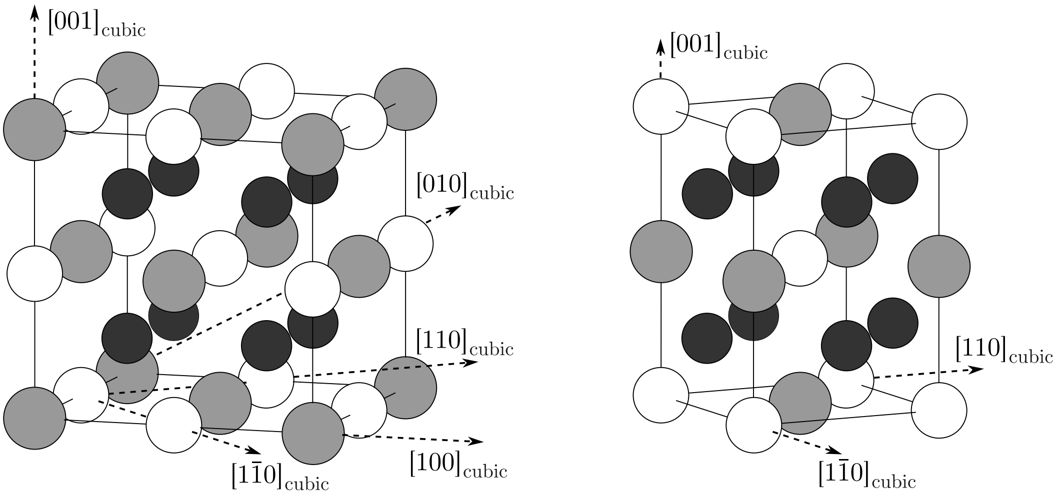

(a) (b)

Figure 1.1: (a) Cubic $L2_1$ structure of the full-Heusler alloy Ni_2MnGa in the austenitic phase. It consists of four interpenetrating fcc sublattices, namely, two Ni sublattices (dark grey), one Mn sublattice (white) and one Ga sublattice (grey). (b) Tetragonal cell generating the orthorhombic super-lattice of modulated phases.

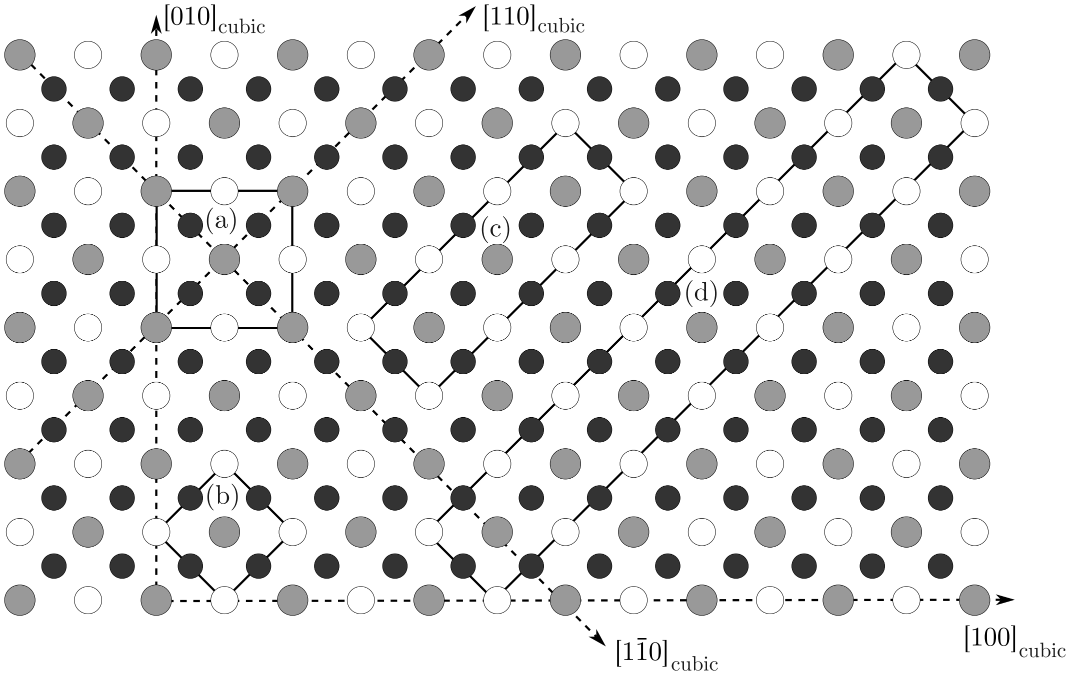

Figure 1.2: View of the Ni_2MnGa crystal along the $[00\bar{1}]_{\mathrm{cubic}}$ direction. Ni, Mn and Ga atoms are, respectively, dark grey, white and grey. Keeping in mind that the modulation of atoms in $(110)_{\mathrm{cubic}}$ planes in the $[1\bar{1}0]_{\mathrm{cubic}}$ direction is not explicitly shown, the unit cells of cubic (a), tetragonal NM (b), orthorhombic 6M (c) and orthorhombic 14M (d) phases are marked out. Note that there are 3 tetragonal and 6 orthorhombic variants, i.e. unit cell orientations.

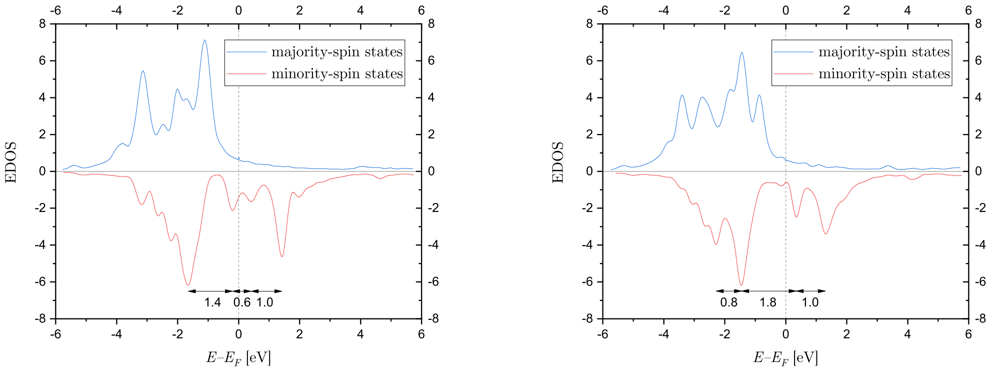

(a) cubic (b) tetragonal

Figure 1.3: Total electronic density of d-states of cubic (a) and tetragonal (b) Ni_2MnGa obtained from the first-principles calculations by Entel et al. (2006)

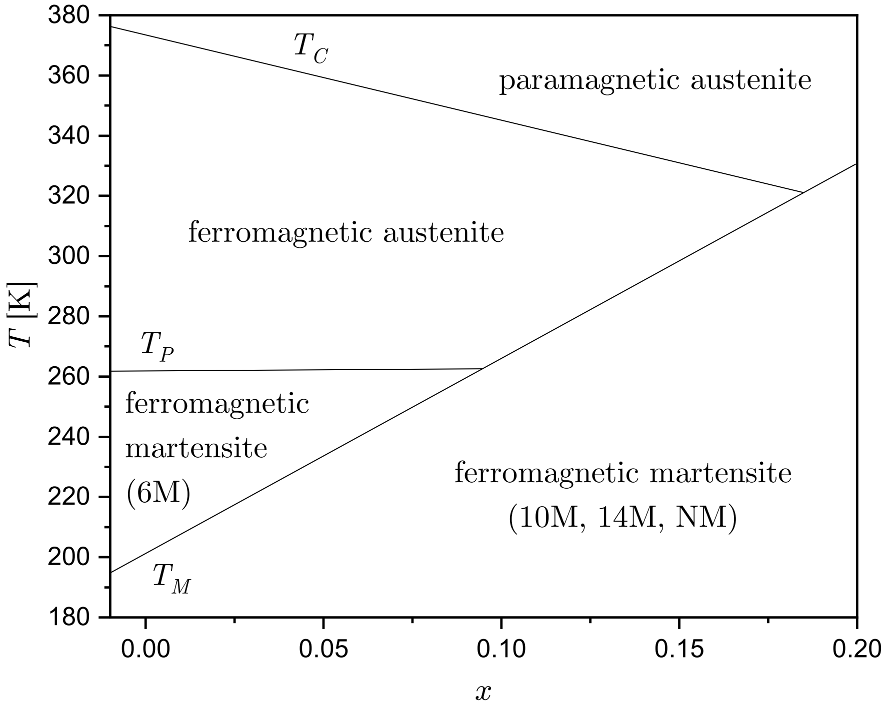

Figure 1.4: Linear interpolations of the the martensitic transformation temperature T_M, the pre-martensitic transformation temperature T_P and Curie temperature T_C as functions of Ni excess x for the stoichiometric composition $Ni_{2+x}Mn_{1-x}Ga$. Data adapted from Vasil'ev et al. (2003).

2. Light-Matter Interaction

In this chapter, we will introduce classical and semiclassical descriptions of light-matter interaction in solids. The introduced models can be used for the analysis of the measured optical and magneto-optical spectra. Relative permittivity tensor spectra will be of particular interest as they provide direct insight into the electronic structure.

We will limit our analysis only to time-harmonic plane waves, which can be justified in linear media, where the Fourier components do not interact (Malý and Troján ek, 2022).

2.1 Maxwell's equations and material tensors

The classical description of the electromagnetic field in linear media (in the time t domain) is provided by Maxwell's equations (Born and Wolf, 1999, Ch. 1.1)

$$\nabla \times \vec{H} - \frac{\partial \vec{D}}{\partial t} = \vec{j}, \tag{2.1a}$$

$$\nabla \times \vec{E} + \frac{\partial \vec{B}}{\partial t} = 0, \tag{2.1b}$$

$$\nabla \cdot \vec{D} = \rho, \tag{2.1c}$$

$$\nabla \cdot \vec{B} = 0. \tag{2.1d}$$

The medium is characterized by a free charge density ρ, a free current density $\vec{j}$ and material equations in the Fourier picture (i.e. the angular frequency ω domain)

$$\vec{D}(\omega) = \varepsilon_{vac}\hat{\varepsilon}(\omega)\vec{E}(\omega), \tag{2.2a}$$

$$\vec{B}(\omega) = \mu_{vac}\hat{\mu}(\omega)\vec{H}(\omega), \tag{2.2b}$$

$$\vec{j}(\omega) = \hat{\sigma}(\omega)\vec{E}(\omega), \tag{2.2c}$$

where a relative permittivity tensor $\hat{\varepsilon}$ binds an electric field $\vec{E}$ with an electric induction (also called electric displacement density) $\vec{D}$. A relative permeability tensor $\hat{\mu}$ binds a magnetic field $\vec{H}$ with a magnetic induction (also called magnetic flux density) $\vec{B}$. The (scalar) permittivity and permeability of a vacuum, together with the speed of light c, satisfy the identity

$$\varepsilon_{vac}\mu_{vac}c^2 = 1. \tag{2.3}$$

Eq. (2.2c) is Ohm's law, which expresses via an electric conductivity tensor $\hat{\sigma}$ the ability of the material to conduct electric current. Alternative formulation of Eq. (2.2a)

$$\vec{D}(\omega) = \varepsilon_{vac}\vec{E}(\omega) + \vec{P}(\omega) \tag{2.4}$$

defines an electric dipole moment density

$$\vec{P}(\omega) = \varepsilon_{vac}\hat{\chi}(\omega)\vec{E}(\omega), \tag{2.5}$$

where (electric) susceptibility tensor components χ_{ij} simply relate to the permittivity tensor as follows:

$$\varepsilon_{ij} = \delta_{ij} + \chi_{ij}. \tag{2.6}$$

The simplest case of magnetization dependence of material tensors is for an originally isotropic material subjected to an external magnetic field. The relative permittivity tensor must then be invariant under the spacial symmetry operations of this field (generating a point group denoted in Schönflies notation as $\mathcal{C}_{\infty h}$) (Višňovský, 2006, Ch. 1.2). Therefore, for the applied field as well as the induced magnetization vector in the z-direction, it must hold

$$\hat{C}_{\infty}^{-1}(\xi)\hat{\varepsilon}\hat{C}_{\infty}(\xi) = \hat{\varepsilon}, \quad \forall \xi \in \mathbb{R}, \tag{2.7}$$

where

$$\hat{C}_{\infty}(\xi) = \begin{pmatrix} \cos\xi & -\sin\xi & 0 \\ \sin\xi & \cos\xi & 0 \\ 0 & 0 & 1 \end{pmatrix} \tag{2.8}$$

is a matrix representation of a rotation about the z-axis by an angle ξ. Following this symmetry requirement, the relative permittivity tensor reduces to

$$\hat{\varepsilon} = \begin{pmatrix} \varepsilon_{xx} & \varepsilon_{xy} & 0 \\ -\varepsilon_{xy} & \varepsilon_{xx} & 0 \\ 0 & 0 & \varepsilon_{zz} \end{pmatrix}. \tag{2.9}$$

Other symmetry requirements, such as invariance under identity and reflection in the xy plane, which are described by their matrix representations

$$\hat{E} = \begin{pmatrix} 1 & 0 & 0 \\ 0 & 1 & 0 \\ 0 & 0 & 1 \end{pmatrix} \quad \text{and} \quad \hat{\Sigma}_h = \begin{pmatrix} 1 & 0 & 0 \\ 0 & 1 & 0 \\ 0 & 0 & -1 \end{pmatrix}, \tag{2.10}$$

respectively, are trivial and do not bring any new information. The reflection in an arbitrary horizontal plane[1], described by a matrix representation

$$\hat{\Sigma}_v(\beta) = \begin{pmatrix} \cos 2\beta & \sin 2\beta & 0 \\ \sin 2\beta & -\cos 2\beta & 0 \\ 0 & 0 & 1 \end{pmatrix}, \quad \beta \in \mathbb{R}, \tag{2.11}$$

is equivalent to a magnetization reversal, i.e.

$$\hat{\Sigma}_h^{-1}(\beta)\hat{\varepsilon}(\vec{M})\hat{\Sigma}_h(\beta) = \hat{\varepsilon}(-\vec{M}), \tag{2.12}$$

and therefore the diagonal elements must be even in magnetization while the off-diagonal elements must be odd, i.e.

$$\varepsilon_{xx}(\vec{M}) = \varepsilon_{xx}(-\vec{M}), \tag{2.13a}$$
$$\varepsilon_{zz}(\vec{M}) = \varepsilon_{zz}(-\vec{M}), \tag{2.13b}$$
$$\varepsilon_{xy}(\vec{M}) = -\varepsilon_{xy}(-\vec{M}). \tag{2.13c}$$

---

[1] This operation is not part of the symmetry group $\mathcal{C}_{\infty h}$ of an axial vector oriented along the z-axis.

For an arbitrary orientation of magnetization a more general Onsager's relation

$$\varepsilon_{ij}(\vec{M}) = \varepsilon_{ji}(-\vec{M}) \tag{2.14}$$

can be derived (Višňovský, 2006, Ch. 2.2). Also, it can be shown that bounded linear systems obeying causality and time invariance satisfy Kramers-Kronig's relations (Višňovský, 2006, Ch. 2.4)

$$\mathrm{Re}\{\varepsilon_{ij}(\omega)\} = \frac{2}{\pi}\mathrm{p.v.}\int_0^\infty \frac{\omega' \,\mathrm{Im}\{\varepsilon_{ij}(\omega')\}}{\omega'^2 - \omega^2}\,\mathrm{d}\omega' \,, \tag{2.15a}$$

$$\mathrm{Im}\{\varepsilon_{ij}(\omega)\} = \mathrm{Im}\{\varepsilon_{ij}(0)\} - \frac{2}{\pi}\mathrm{p.v.}\int_0^\infty \frac{\omega \,\mathrm{Re}\{\varepsilon_{ij}(\omega')\}}{\omega'^2 - \omega^2}\,\mathrm{d}\omega' \,. \tag{2.15b}$$

In practice, one of the complex components can be calculated from the other using Eqs. (2.15), where we integrate one of the components over a spectral range that is sufficiently large, in order for the change of integration limits to be justified.

2.2 Lorentz's model

In the previous, section we discussed the general macroscopic properties of the permittivity tensor originating from the linearity assumption as well as symmetries of polar geometry. Now we turn our focus to its spectral dependence, which has origin in the electronic structure of the material. Lorentz's model (Lorentz, 1906) treats atoms of a solid as small dipole oscillators consisting of a valence electron that is bound to its positively charged nucleus. Assuming an infinite mass of the nucleus, therefore, a stationary nucleus, a relative deviation of the electron from its nucleus $\vec{r}$ satisfies the equation of motion (Nývlt, 1996, Ch. 3.2)

$$m\frac{\mathrm{d}^2\vec{r}}{\mathrm{d}t^2} = q\vec{E} + q\frac{\mathrm{d}\vec{r}}{\mathrm{d}t} \times \vec{B}_{ext} - m\Gamma\frac{\mathrm{d}\vec{r}}{\mathrm{d}t} - m\omega_0^2\vec{r}, \tag{2.16}$$

where the left-hand side term represents the effect of a net force on $\vec{r}$ via Newton's second law of motion. On the right-hand side, the first two terms introduce a driving force, which is the Lorentz force. Considering that the electron velocity is much smaller than the speed of light (Born and Wolf, 1999, p. 28), the magnetic component of the incident wave can be neglected, and the two terms describe the incident light via its electric field $\vec{E}$ and a static external magnetic field, respectively. The third term describes a damping via a damping constant Γ and the fourth term is a linear elastic force that binds the dipole together (ω_0 is the eigenfrequency of a free oscillator). After dividing by an effective mass of the electron m and rearranging the terms in Eq. (2.16), it follows:

$$\frac{\mathrm{d}^2\vec{r}}{\mathrm{d}t^2} + \Gamma\frac{\mathrm{d}\vec{r}}{\mathrm{d}t} + \omega_0^2\vec{r} - \frac{q}{m}\frac{\mathrm{d}\vec{r}}{\mathrm{d}t} \times \vec{B}_{ext} = \frac{q}{m}\vec{E}. \tag{2.17}$$

Without any loss of generality we choose the z-axis to be parallel to the external magnetic field (i.e. $\vec{B}_{ext} = (0, 0, B_z)$) to obtain the set of equations

$$\frac{\mathrm{d}^2x}{\mathrm{d}t^2} + \Gamma\frac{\mathrm{d}x}{\mathrm{d}t} + \omega_0^2 x + \omega_c\frac{\mathrm{d}y}{\mathrm{d}t} = \frac{q}{m}E_x, \tag{2.18a}$$

$$\frac{\mathrm{d}^2y}{\mathrm{d}t^2} + \Gamma\frac{\mathrm{d}y}{\mathrm{d}t} + \omega_0^2 y - \omega_c\frac{\mathrm{d}x}{\mathrm{d}t} = \frac{q}{m}E_y, \tag{2.18b}$$

$$\frac{\mathrm{d}^2z}{\mathrm{d}t^2} + \Gamma\frac{\mathrm{d}z}{\mathrm{d}t} + \omega_0^2 z = \frac{q}{m}E_z, \tag{2.18c}$$

where

$$\omega_c = \frac{qB_z}{m} \tag{2.19}$$

denotes the cyclotron frequency. We shall conveniently use matrix notation for further manipulation with the set of equations above:

$$\begin{pmatrix} \frac{\mathrm{d}^2}{\mathrm{d}t^2} + \Gamma\frac{\mathrm{d}}{\mathrm{d}t} + \omega_0^2 & \omega_c\frac{\mathrm{d}}{\mathrm{d}t} & 0 \\ -\omega_c\frac{\mathrm{d}}{\mathrm{d}t} & \frac{\mathrm{d}^2}{\mathrm{d}t^2} + \Gamma\frac{\mathrm{d}}{\mathrm{d}t} + \omega_0^2 & 0 \\ 0 & 0 & \frac{\mathrm{d}^2}{\mathrm{d}t^2} + \Gamma\frac{\mathrm{d}}{\mathrm{d}t} + \omega_0^2 \end{pmatrix} \begin{pmatrix} x \\ y \\ z \end{pmatrix} = \frac{q}{m}\begin{pmatrix} E_x \\ E_y \\ E_z \end{pmatrix}. \tag{2.20}$$

For a harmonic field $\vec{E} = \vec{E}_0 \exp(i\omega t)$, we expect a harmonic solution in the form[2]

$$\vec{r} = \vec{r}_0 \exp(i\omega t). \tag{2.21}$$

Substitution of this *ansatz* to Eq. (2.20) yields

$$\begin{pmatrix} -\omega^2 + i\Gamma\omega + \omega_0^2 & i\omega_c\omega & 0 \\ -i\omega_c\omega & -\omega^2 + i\Gamma\omega + \omega_0^2 & 0 \\ 0 & 0 & -\omega^2 + i\Gamma\omega + \omega_0^2 \end{pmatrix} \begin{pmatrix} x_0 \\ y_0 \\ z_0 \end{pmatrix} = \frac{q}{m}\begin{pmatrix} E_{x0} \\ E_{y0} \\ E_{z0} \end{pmatrix}. \tag{2.22}$$

By inverting the matrix[3] on the left-hand side,

$$\begin{pmatrix} x_0 \\ y_0 \\ z_0 \end{pmatrix} = \frac{q}{m}\begin{pmatrix} \frac{\omega_0^2-\omega^2+i\Gamma\omega}{\left(\omega_0^2-\omega^2+i\Gamma\omega\right)^2-\omega_c^2\omega^2} & \frac{i\omega_c\omega}{\left(\omega_0^2-\omega^2+i\Gamma\omega\right)^2-\omega_c^2\omega^2} & 0 \\ \frac{-i\omega_c\omega}{\left(\omega_0^2-\omega^2+i\Gamma\omega\right)^2-\omega_c^2\omega^2} & \frac{\omega_0^2-\omega^2+i\Gamma\omega}{\left(\omega_0^2-\omega^2+i\Gamma\omega\right)^2-\omega_c^2\omega^2} & 0 \\ 0 & 0 & \frac{1}{\omega_0^2-\omega^2+i\Gamma\omega} \end{pmatrix} \begin{pmatrix} E_{x0} \\ E_{y0} \\ E_{z0} \end{pmatrix}, \tag{2.23}$$

and by comparing Eq. (2.5) to the expression of the electric dipole moment density $\vec{P}$ as a product of the electric dipole density N and the electric dipole moment of the system $q\vec{r}$, i.e.

$$\vec{P} = \varepsilon_{vac}\hat{\chi}\vec{E} = qN\vec{r}, \tag{2.24}$$

---

[2] Note that the chosen time variation $\exp(i\omega t)$ leads to a complex refractive index for absorbing materials in the form $n - ik$ (Wooten, 1972), where $n > 0, k > 0$, and which subsequently leads to a complex permittivity $\operatorname{Re}\varepsilon - i\operatorname{Im}\varepsilon$, if we want $\operatorname{Im}\varepsilon > 0$.

[3] For $a, b \in \mathbb{C}$ satisfying the condition $a\left(a^2 + b^2\right) = 0$ it holds

$$\begin{pmatrix} a & b & 0 \\ -b & a & 0 \\ 0 & 0 & a \end{pmatrix}^{-1} = \begin{pmatrix} \frac{a}{a^2+b^2} & \frac{b}{a^2+b^2} & 0 \\ \frac{-b}{a^2+b^2} & \frac{a}{a^2+b^2} & 0 \\ 0 & 0 & \frac{1}{a} \end{pmatrix}.$$

we have finally derived the susceptibility tensor

$$\hat{\chi} = \omega_p^2 \begin{pmatrix} \frac{\omega_0^2-\omega^2+i\Gamma\omega}{\left(\omega_0^2-\omega^2+i\Gamma\omega\right)^2-\omega_c^2\omega^2} & \frac{i\omega_c\omega}{\left(\omega_0^2-\omega^2+i\Gamma\omega\right)^2-\omega_c^2\omega^2} & 0 \\ \frac{-i\omega_c\omega}{\left(\omega_0^2-\omega^2+i\Gamma\omega\right)^2-\omega_c^2\omega^2} & \frac{\omega_0^2-\omega^2+i\Gamma\omega}{\left(\omega_0^2-\omega^2+i\Gamma\omega\right)^2-\omega_c^2\omega^2} & 0 \\ 0 & 0 & \frac{1}{\omega_0^2-\omega^2+i\Gamma\omega} \end{pmatrix}, \tag{2.25}$$

where

$$\omega_p = \sqrt{\frac{Nq^2}{\varepsilon_{vac}m}} \tag{2.26}$$

denotes the plasma frequency. Alternatively, using Eq. (2.6), we can rewrite this result in terms of permittivity tensor elements as

$$\varepsilon_{xx}(\omega) = \varepsilon_{yy}(\omega) = 1 + \omega_p^2 \frac{\omega_0^2 - \omega^2 + i\Gamma\omega}{\left(\omega_0^2 - \omega^2 + i\Gamma\omega\right)^2 - \omega_c^2\omega^2}, \tag{2.27a}$$

$$\varepsilon_{xy}(\omega) = -\varepsilon_{yx}(\omega) = \omega_p^2 \frac{i\omega_c\omega}{\left(\omega_0^2 - \omega^2 + i\Gamma\omega\right)^2 - \omega_c^2\omega^2}, \tag{2.27b}$$

$$\varepsilon_{zz}(\omega) = 1 + \frac{\omega_p^2}{\omega_0^2 - \omega^2 + i\Gamma\omega}. \tag{2.27c}$$

Without the external magnetic field ($\omega_c = 0$), there is no induced anisotropy and the scalar permittivity is given by Eq. (2.27c). A dispersive behavior of the real part and a dissipative behavior of the imaginary part are good classical approximations of an interband electron transition at the frequency ω_0 (see Fig. 2.1a).

2.3 Drude's model

Drude's model describes a solid as an ensemble of free electrons (Born and Wolf, 1999, Ch. 13.3). This situation is equivalent to Lorentz's model, where the electrons are not bound to their atoms, which corresponds to the eigenfrequency ω_0 being set to zero, i.e.

$$\varepsilon_{xx}(\omega) = \varepsilon_{yy}(\omega) = 1 + \omega_p^2 \frac{-\omega^2 + i\Gamma\omega}{\left(-\omega^2 + i\Gamma\omega\right)^2 - \omega_c^2\omega^2}, \tag{2.28a}$$

$$\varepsilon_{xy}(\omega) = -\varepsilon_{yx}(\omega) = \omega_p^2 \frac{i\omega_c\omega}{\left(-\omega^2 + i\Gamma\omega\right)^2 - \omega_c^2\omega^2}, \tag{2.28b}$$

$$\varepsilon_{zz}(\omega) = 1 + \frac{\omega_p^2}{-\omega^2 + i\Gamma\omega}. \tag{2.28c}$$

This model is a great classical approximation of low energy absorption caused by intraband transitions of conduction electrons in metals. Without the external magnetic field ($\omega_c = 0$), the scalar permittivity is given by Eq. (2.28c). As can bee seen in Fig. 2.1b, the imaginary part exhibits a decreasing behavior, while the real part is an increasing function, and both complex parts diverge at zero energy.

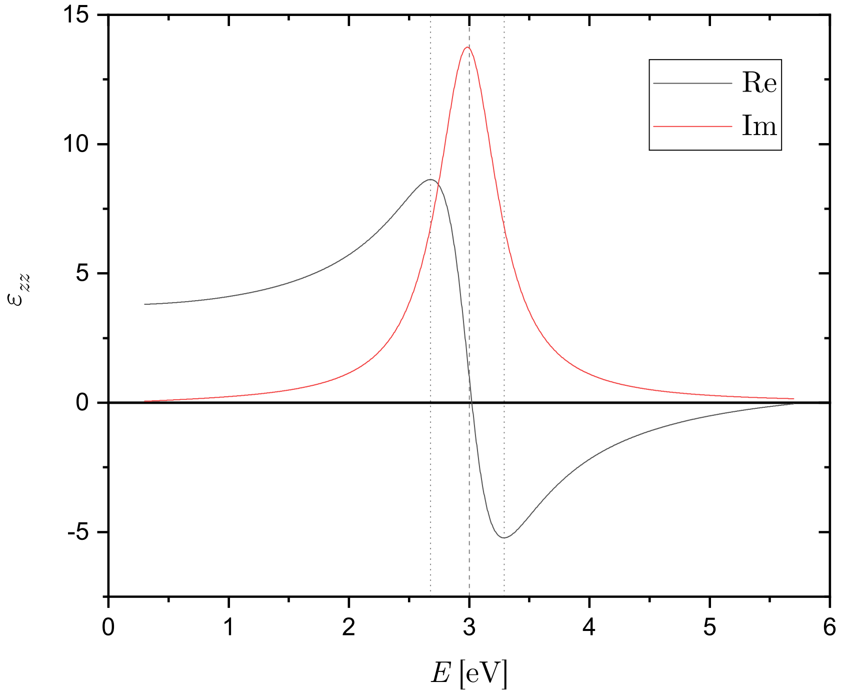

(a) Lorentz's model with $\hbar\omega_0/e = 3\,\text{eV}$

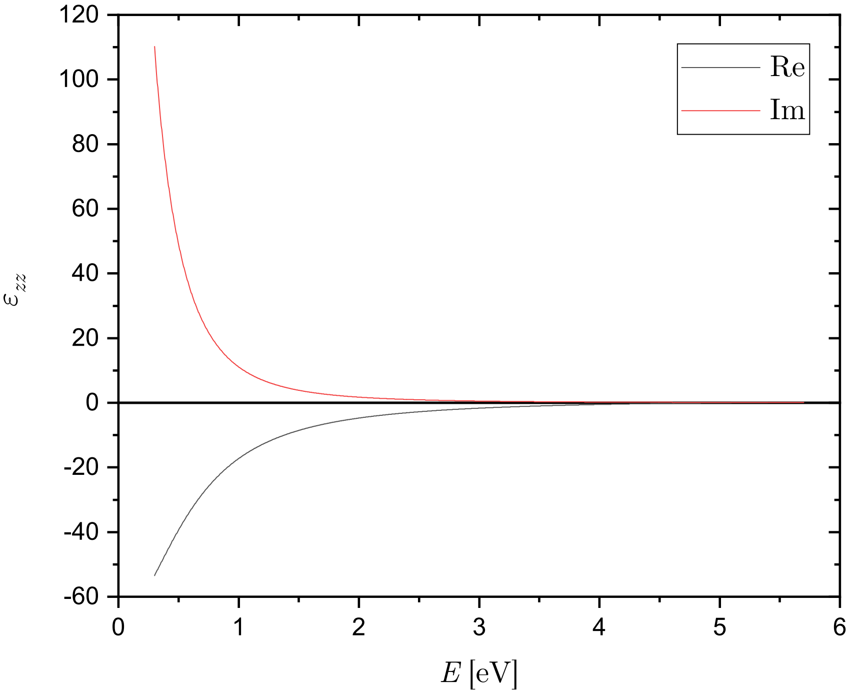

(b) Drude's model, i.e. $\hbar\omega_0/e = 0$

Figure 2.1: The relative permittivity tensor element ε_{zz} spectra ($E = \hbar\omega/e$, where $\hbar$ is reduced Planck's constant and e is the elementary charge) according to classical models with set parameters $\hbar\omega_p/e = 5\,\text{eV}$ and $\hbar\Gamma_0/e = 2\times10^{-8}\,\text{eV}$

2.4 Semiclassical model of electron transitions

Important consequence of quantum electrodynamics is the association of a spin angular momentum (SAM) of a photon with a polarization state (Zvezdin and Kotov, 1997, Ch. 2.5.1). Considering the unit of angular momentum to be $\hbar$, a photon is a spin-1 particle, and has two possible projections of its spin in the direction of its propagation, namely, ± 1. These projections can be identified with the LCP (projection $+1$) and RCP (projection -1) polarization states[4]. When a photon is absorbed, the angular momentum of matter must also change accordingly, so that the total angular momentum is conserved. Together, the splitting and the different populations of energy levels in matter with the selection rules, following from the angular momentum conservation, give rise to magneto-optical phenomena (Zvezdin and Kotov, 1997, Ch. 5). Following the work of Kahn et al. (1969), we can distinguish two special cases of magneto-optical transitions:

Type I double transitions (or so-called diamagnetic transitions) are spin- as well as electric-dipole-allowed transitions between an orbital singlet ground state $|g\rangle$ and two excited states $|e_-\rangle, |e_+\rangle$ that originate from a splitting of a degenerated exited state $|e\rangle$ caused by the effect of exchange field and spin-orbit coupling. This type of transition is described by a center frequency $\omega_0 = \frac{\omega_+ + \omega_-}{2}$, a frequency half-width at half-maximum (HWHM) Γ_0 of this transition in a $\mathrm{Im}\{\varepsilon_{xx}(\omega)\}$ spectrum and an excited state frequency splitting $\Delta\omega_0 = \frac{\omega_+ - \omega_-}{2}$, where ω_+ and ω_- are the frequencies of the transitions $|g\rangle \rightarrow |e_+\rangle$ and $|g\rangle \rightarrow |e_-\rangle$ corresponding to the absorption of LCP and RCP light, respectively. We also assume that the energy level splitting does not change oscillator strengths f_+, f_- related to the absorption of LCP and RCP light, respectively, and $f_+ \approx f_-$. The spectral dependence of the off-diagonal element of the permittivity tensor is then given by[5]

$$\varepsilon_{xy}(\omega) = -i\Gamma_0\Delta\omega_0 \,\mathrm{Im}\{\varepsilon_{xx}(\omega_0)\} \frac{(\omega_0 - \omega)^2 - (\Gamma_0^2 + \Delta\omega_0^2) + 2i\Gamma_0(\omega_0 - \omega)}{\left[(\omega_0 - \omega)^2 - (\Gamma_0^2 + \Delta\omega_0^2)\right]^2 + 4\Gamma_0^2(\omega_0 - \omega)^2}. \tag{2.29}$$

As we can see in Fig. 2.2a, the imaginary part of Eq. (2.29) is an even function of $(\omega_0 - \omega)$ and exhibits a dissipative behavior, while the real part is odd and has a dispersive behavior.

Type II single transitions (or so-called paramagnetic transitions) are, on the other hand, spin-forbidden as well as electric-dipole-forbidden transitions between a ground state $|g\rangle$ and an exited state $|e\rangle$. This situation can occur when the spin-orbit splitting of the ground state is negligible, i.e. $\Delta\omega_0 \approx 0$ ($\omega_+ \approx \omega_- \approx \omega_0$), and it only affects the oscillator strengths, resulting in a nonzero relative magnetic circular dichroism (also called fractional dichroism)

$$\xi = \frac{f_- - f_+}{f_- + f_+}. \tag{2.30}$$

The oscillator strength difference is a consequence of the difference in population for finite temperatures in the ground state energy levels. In this case, it can be

---

[4] The concept of polarization will be explained in detail in the next chapter.

[5] We are using the time variation $\exp(i\omega)$ instead of the time variation $\exp(-i\omega)$ used by Kahn et al. (1969). One is obtained from the other by a Hermitian conjugation.

shown that the spectral dependence of the off-diagonal element of the relative permittivity tensor is

$$\varepsilon_{xy}(\omega) = 2i\Gamma_0\xi\,\mathrm{Im}\{\varepsilon_{xx}(\omega_0)\}\frac{\omega(\omega_0^2-\omega^2-\Gamma_0^2)-i\Gamma_0(\omega_0^2+\omega^2-\Gamma_0^2)}{\left(\omega_0^2-\omega^2+\Gamma_0^2\right)^2+4\Gamma_0^2\omega^2}, \tag{2.31}$$

and the parities of the imaginary and real parts are opposite to those in Eq. (2.29), i.e. the imaginary part behaves dispersively, while the real part has a dissipative shape (see Fig. 2.2b).

In practice, the magneto-optical transitions are more complex and do not fall exclusively in either of those special cases, but rather manifest, to some extent, a behavior of both.

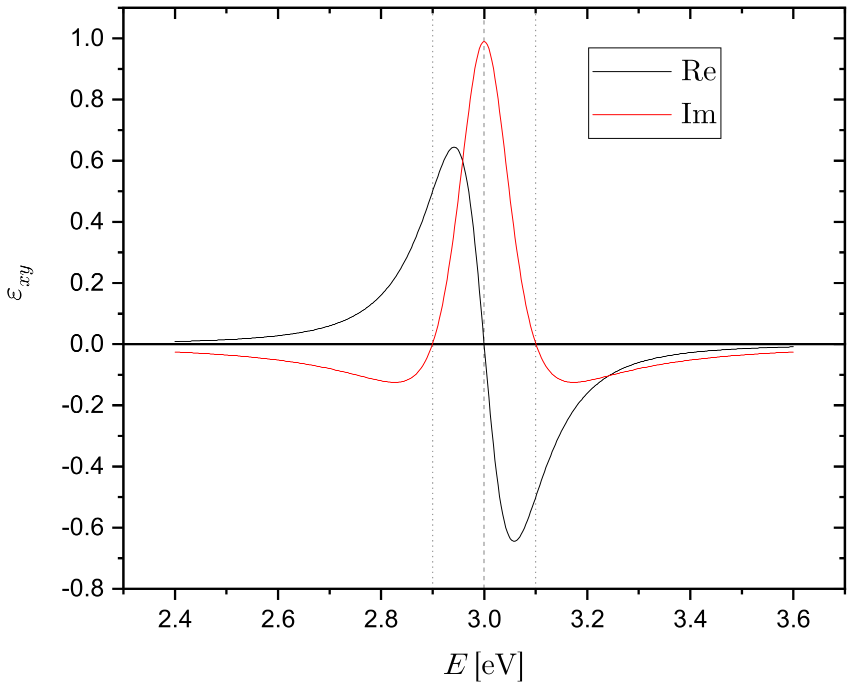

(a) Type I double transition with $\hbar\Delta\omega_0/e = 0.01\,\text{eV}$

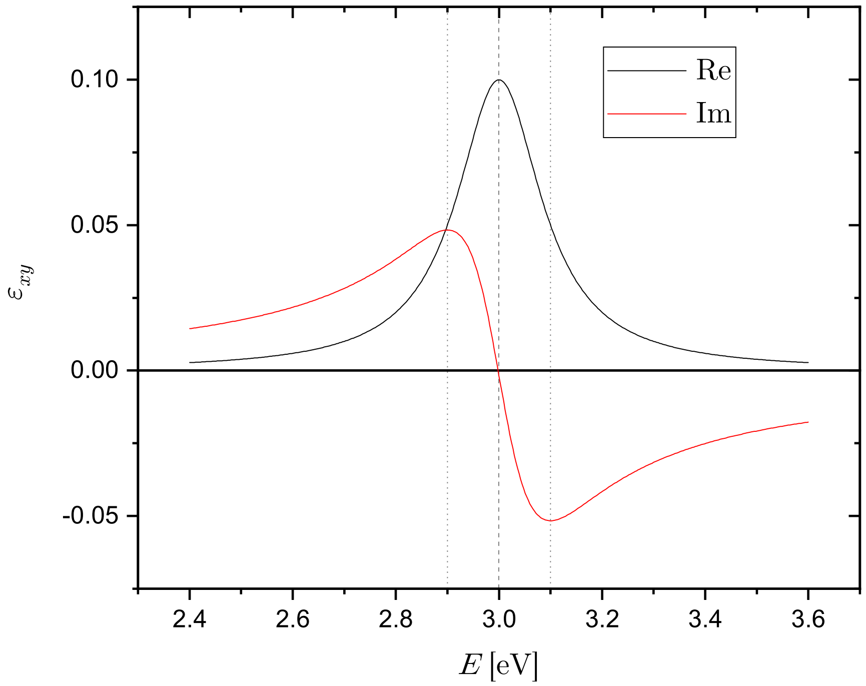

(b) Type II single transition with $\xi = 0.01$

Figure 2.2: The spectra ($E = \hbar\omega/e$, where $\hbar$ is reduced Planck's constant and e is the elementary charge) of the off-diagonal element of the relative permittivity tensor ε_{xy} computed from the semiclassical model, where we set $\hbar\omega_0/e = 3\,\text{eV}$, $\hbar\Gamma_0/e = 0.1\,\text{eV}$ and $\text{Im}\{\varepsilon_{xx}(\omega_0)\} = 10$

3. Description of Polarized Light

Polarization is a property of a vector wave that describes the behavior of its vector with time at a fixed point in space. A mathematical description of polarized light shall be introduced below. For more in-depth treatment, we refer to Azzam and Bashara (1977, Ch. 1).

From Maxwell's equations (2.1) in a non-absorbing isotropic homogeneous medium with no free charges, a wave equation

$$\nabla^2 \vec{E} - \frac{\varepsilon\mu}{c^2}\frac{\partial^2 \vec{E}}{\partial t^2} = 0 \tag{3.1}$$

can be derived, where both the relative permittivity ε and the relative permeability μ are real scalars. As was argued in Section 2.2, dedicated to the classical model of electron transitions, when considering that the electron velocity is much smaller than the speed of light the magnetic component of the incident wave can be neglected (Born and Wolf, 1999, p. 28). We are particularly interested in a solution of the wave equation that is also compatible with Maxwell's equations as a whole. Such a solution is the transverse monochromatic plane wave

$$\vec{E}(\vec{r},t) = \vec{E_0}\exp[i(\omega t - \vec{\gamma}\cdot\vec{r})] \tag{3.2}$$

that is characterized by its angular frequency ω and its propagation vector $\vec{\gamma}$, and it satisfies the two following conditions:

$$\gamma = \frac{\omega}{c}n, \tag{3.3a}$$

$$0 = \vec{\gamma}\cdot\vec{E}. \tag{3.3b}$$

We denoted $n = \sqrt{\varepsilon\mu}$ the real part of the index of refraction.

3.1 Jones formalism

Since we are only considering transverse waves, as required by Eq. (3.3b), the choice of the Cartesian coordinate system with the z-axis oriented in the direction of the propagation vector $\vec{\gamma}$, reduces the z-component of the electric field vector to zero. The polarization state is then fully described by the complex vector $\vec{E_0}$ in the xy-plane, and we can define the Jones vector

$$\vec{J} = \begin{pmatrix} E_{0x} \\ E_{0y} \end{pmatrix} = \begin{pmatrix} a_x e^{i\delta_x} \\ a_y e^{i\delta_y} \end{pmatrix} \in \mathbb{C}^2. \tag{3.4}$$

As we can see, 4 real parameters, the amplitudes a_x, a_y and the phases δ_x, δ_y of two orthogonal components of $\vec{E_0}$, are needed in order to provide a complete description of the behavior in the transverse plane. The knowledge of the relative phase difference $\delta = \delta_y - \delta_x$ is for most purposes sufficient, which reduces the number of necessary parameters to 3. If we are interested in the polarization states only, and we are not concerned about the absolute light intensity, the number of parameters can be then reduced to 2 by normalizing the Jones vector, i.e. setting

$$\left|\vec{J}\right|^2 = \vec{J}^+\vec{J} = \begin{pmatrix} J_x^* & J_y^* \end{pmatrix} \begin{pmatrix} J_x \\ J_y \end{pmatrix} = |J_x|^2 + |J_y|^2 = 1, \tag{3.5}$$

where the symbols * and $^+$ denote the complex and Hermitian conjugations, respectively.

Supposing no depolarization is present, the effect of a polarization device on a polarization state can be described using matrix notation as

$$\vec{J}_f = \mathbb{M}\vec{J}_i, \tag{3.6}$$

where

$$\mathbb{M} = \begin{pmatrix} M_{xx} & M_{xy} \\ M_{yx} & M_{yy} \end{pmatrix} \in \mathbb{C}^{2\times 2} \tag{3.7}$$

is the Jones matrix. $\vec{J}_i$, $\vec{J}_f$ are the Jones vectors of the initial and the final polarization states, respectively.

The optical system can be modeled as a series of such polarization devices, and the total effect is determined by the product of the Jones matrices of all the polarization elements. Examples of common polarization devices (Azzam and Bashara, 1977, Ch. 2.2.3) and their Jones matrices are provided in Table 3.1. The origins of the polarization effects can vary (Zvezdin and Kotov, 1997). For example, let us suppose that polarized light travels a finite distance through a material in a direction, along which optical properties are constant. This type of transmission device can then absorb, retard or both absorb and retard each of the basis polarization states[1] differently, causing changes in the ratio of their amplitudes and their phase difference. Special cases of these phenomena include linear and circular dichroisms (abbr. LD and CD), where, in the first case, the linear polarizations are absorbed differently for different values of azimuth and, in the second case, the right and left circular polarizations are absorbed differently. The other special phenomena are the linear and circular birefringences (abbr. LB and CB), where either the linear or circular components are delayed differently relative to each other.

3.2 Polarization ellipse parameters

It can be shown (Born and Wolf, 1999, ch. 1.4.2) that in the transverse plane (i.e. xy-plane, when considering propagation along the z-axis), the electric field vector $\vec{E}$ satisfies the equation of an ellipse

$$\left(\frac{\mathrm{Re}\{E_x\}}{a_x}\right)^2 - 2\left(\frac{\mathrm{Re}\{E_x\}}{a_x}\right)\left(\frac{\mathrm{Re}\{E_y\}}{a_y}\right)\cos\delta + \left(\frac{\mathrm{Re}\{E_y\}}{a_y}\right)^2 = \sin^2\delta, \tag{3.8}$$

which is inscribed into a rectangle with the sides $2a_x$ and $2a_y$. The sides of the rectangle are parallel to the coordinate axes and the diagonal makes an angle $\psi \in [0, \pi/2]$ with the x-axis (see Fig. 3.1). There are other important parameters

---

[1] Basis states are discussed in Section 3.5.

Table 3.1: Jones matrices of common polarization devices in both linear polarization states and circular polarization states bases

Pol. device	Ph.	$\mathbb{M}$	$[\mathbb{M}]^{\mathcal{B}_{CP}}$
linear polarizer[1]	LD	$\begin{pmatrix} 1 & 0 \\ 0 & e^{-\alpha} \end{pmatrix}$	$e^{-\frac{\alpha}{2}} \begin{pmatrix} \cosh\frac{\alpha}{2} & \sinh\frac{\alpha}{2} \\ \sinh\frac{\alpha}{2} & \cosh\frac{\alpha}{2} \end{pmatrix}$
circular polarizer[2]	CD	$e^{-\frac{\beta}{2}} \begin{pmatrix} \cosh\frac{\beta}{2} & -i\sinh\frac{\beta}{2} \\ i\sinh\frac{\beta}{2} & \cosh\frac{\beta}{2} \end{pmatrix}$	$\begin{pmatrix} 1 & 0 \\ 0 & e^{-\beta} \end{pmatrix}$
linear retarder[3]	LB	$\begin{pmatrix} 1 & 0 \\ 0 & e^{-i\Gamma} \end{pmatrix}$	$e^{-i\frac{\Gamma}{2}} \begin{pmatrix} \cos\frac{\Gamma}{2} & i\sin\frac{\Gamma}{2} \\ i\sin\frac{\Gamma}{2} & \cos\frac{\Gamma}{2} \end{pmatrix}$
circular retarder[4]	CB	$e^{i\frac{\Theta}{2}} \begin{pmatrix} \cos\frac{\Theta}{2} & -\sin\frac{\Theta}{2} \\ \sin\frac{\Theta}{2} & \cos\frac{\Theta}{2} \end{pmatrix}$	$\begin{pmatrix} 1 & 0 \\ 0 & e^{i\Theta} \end{pmatrix}$

Notes:

[1] for $\alpha \in \mathbb{R}$ and $\alpha > 0$ the polarization axis is parallel to the x-axis

[2] for $\beta \in \mathbb{R}$ and $\beta > 0$ the LCP component is exponentially attenuated

[3] for $\Gamma \in \mathbb{R}$ and $\Gamma > 0$ the fast axis is parallel to the x-axis; the linear retarder is usually referred to as a phase-plate

[4] for $\Theta \in \mathbb{R}$ and $\Theta > 0$ there is a phase difference between CP components of transmitted light causing azimuth change by $\Theta/2$, hence this device is also referred to as a rotator

of the ellipse. Namely, the lengths of its major and minor semiaxes a and b, respectively, the azimuth $\theta \in [0, \pi)$, which represents the angle the major semiaxis makes with the x-axis, and the ellipticity $\epsilon \in [-\pi/4, \pi/4]$, whose sign is indicative of either anticlockwise ($-$ sign) or clockwise ($+$ sign) sense, in which the ellipse is traced when looking in the opposite direction than the z-axis. These parameters are related to one another by the set of equations (Born and Wolf, 1999, pp. 26-27):

$$a_x^2 + a_y^2 = a^2 + b^2, \tag{3.9a}$$

$$\tan\psi = \frac{a_y}{a_x}, \tag{3.9b}$$

$$\tan\epsilon = \pm\frac{b}{a}, \tag{3.9c}$$

$$\tan 2\theta = \tan 2\psi \cos\delta, \tag{3.9d}$$

$$\sin 2\epsilon = \sin 2\psi \sin\delta. \tag{3.9e}$$

We can express the normalized Jones vector using the azimuth and the ellipticity as (Azzam and Bashara, 1977, p. 27)

$$\vec{J} = \begin{pmatrix} \cos\theta & -\sin\theta \\ \sin\theta & \cos\theta \end{pmatrix} \begin{pmatrix} \cos\epsilon \\ i\sin\epsilon \end{pmatrix} = \begin{pmatrix} \cos\theta\cos\epsilon - i\sin\theta\sin\epsilon \\ \sin\theta\cos\epsilon + i\cos\theta\sin\epsilon \end{pmatrix}, \tag{3.10}$$

where we simply rotated the normalized Jones vector with the given ellipticity by the azimuth.

3.3 Complex polarization parameter

An alternative representation of the polarization states is using the mapping onto the complex plane (Azzam and Bashara, 1977, ch. 1.7) by defining the complex polarization parameter as a ratio of the Jones vector components

$$\chi = \frac{J_y}{J_x} = \frac{a_y}{a_x} e^{i(\delta_y - \delta_x)} = \tan\psi e^{i\delta}. \tag{3.11}$$

Using Eqs. (3.9) and goniometric function identities

$$\tan 2\xi = \frac{2\tan\xi}{1-\tan^2\xi}, \tag{3.12}$$

$$\sin 2\xi = \frac{2\tan\xi}{1+\tan^2\xi}, \tag{3.13}$$

we can derive the equations

$$\tan 2\theta = \frac{2\,\mathrm{Re}\,\chi}{1-|\chi|^2}, \tag{3.14a}$$

$$\sin 2\epsilon = \frac{2\,\mathrm{Im}\,\chi}{1+|\chi|^2}, \tag{3.14b}$$

relating the azimuth and the ellipticity to the complex polarization parameter. The inverse relation

$$\chi = \frac{\tan\theta + i\tan\epsilon}{1 - i\tan\theta\tan\epsilon} \tag{3.15}$$

can be simply obtained from Eq. (3.10).

From Eqs. (3.8) and (3.6), the effect of a polarization device can also be expressed with the Jones matrix elements in the following way:

$$\chi_f = \frac{M_{yx} + M_{yy}\chi_i}{M_{xx} + M_{xy}\chi_i}. \tag{3.16}$$

3.4 Special polarization states

It is illustrative to highlight the values of the parameters we previously defined for a few special cases that are listed in Table 3.2. These states are usually referred to using their abbreviations. Namely, L*P are the *Linearly Polarized* states that are either *Horizontal*, *Vertical*, *Diagonal* or *Antidiagonal* (the corresponding letter is substituted for the asterisk). The remaining two states are the *Right* and *Left Circularly Polarized* states.

3.5 Basis states of polarization

We previously described a polarization state as a pair of two complex numbers E_{0x}, E_{0y} in the transverse plane. In doing so, we implicitly chose the basis $\mathcal{B}_{XY} = (\vec{x}, \vec{y})$, consisting of two orthonormal linear polarization states

$$\vec{x} = \begin{pmatrix} 1 \\ 0 \end{pmatrix} \quad \text{and} \quad \vec{y} = \begin{pmatrix} 0 \\ 1 \end{pmatrix}.$$

Sometimes, however, the choice of a different basis might prove itself useful when taking into consideration the symmetry of the problem at hand. The Jones vector can be expressed using different superpositions of base vectors, e.g.

$$\vec{J} = E_{0x}\vec{x} + E_{0y}\vec{y} = E_1\vec{b}_1 + E_2\vec{b}_2. \tag{3.17}$$

The representation of the Jones vector

$$\left[\vec{J}\right]^{\mathcal{B}} = \begin{pmatrix} E_1 \\ E_2 \end{pmatrix} \tag{3.18}$$

with respect to the basis $\mathcal{B} = \left(\vec{b}_1, \vec{b}_2\right)$ is related to the representation with respect to the basis $\mathcal{B}_{XY}$ via the transformation relation (Azzam and Bashara, 1977, Ch. 1.6.5)

$$\left[\vec{J}\right]^{\mathcal{B}} = \mathbb{B}^{-1}\vec{J}, \tag{3.19}$$

where

$$\mathbb{B} = \begin{pmatrix} b_{1x} & b_{2x} \\ b_{1y} & b_{2y} \end{pmatrix}. \tag{3.20}$$

The transformation relation between the bases $\mathcal{B}_{XY}$ and $\mathcal{B}$ for the Jones matrix representation is

$$[\mathbb{M}]^{\mathcal{B}} = \mathbb{B}^{-1}\mathbb{M}\mathbb{B}. \tag{3.21}$$

The complex polarization parameter in the basis $\mathcal{B}$, defined as

$$[\chi]^{\mathcal{B}} = \frac{E_2}{E_1}, \tag{3.22}$$

can be computed from the complex polarization parameter in the basis $\mathcal{B}_{XY}$ as follows:

$$[\chi]^{\mathcal{B}} = \frac{-b_{1y} + b_{1x}\chi}{b_{2y} - b_{2x}\chi}. \tag{3.23}$$

3.5.1 Circular polarization states basis

In many cases, the circular polarization states basis $\mathcal{B}_{CP} = \left(\vec{r}, \vec{l}\right)$, where

$$\vec{r} = \frac{1}{\sqrt{2}}\begin{pmatrix} 1 \\ i \end{pmatrix} \quad \text{and} \quad \vec{l} = \frac{1}{\sqrt{2}}\begin{pmatrix} 1 \\ -i \end{pmatrix} \tag{3.24}$$

are the RCP and LCP states, respectively, might prove itself useful. The representation of the normalized Jones vector of given azimuth and ellipticity in this basis (Azzam and Bashara, 1977, p. 28)

$$\left[\vec{J}\right]^{\mathcal{B}_{CP}} = \frac{1}{\sqrt{2}}\begin{pmatrix} (\cos\epsilon + \sin\epsilon)e^{-i\theta} \\ (\cos\epsilon - \sin\epsilon)e^{i\theta} \end{pmatrix} \tag{3.25}$$

provides, together with the linear representation in the form of Eq. (3.10), a quick insight into the changes of azimuth and ellipticity caused by the polarization devices in Table 3.1. The relationships between the complex polarization parameter in the basis $\mathcal{B}_{CP}$, the azimuth and the ellipticity are expressed by the set of equations (Azzam and Bashara, 1977, Ch. 1.7.2)

$$[\chi]^{\mathcal{B}_{CP}} = \cot\left(\epsilon + \frac{\pi}{4}\right)e^{2i\theta}, \tag{3.26a}$$

$$\theta = \frac{1}{2}\arg\,[\chi]^{\mathcal{B}_{CP}}, \tag{3.26b}$$

$$\tan\epsilon = \frac{1 - [\chi]^{\mathcal{B}_{CP}}}{1 + [\chi]^{\mathcal{B}_{CP}}}. \tag{3.26c}$$

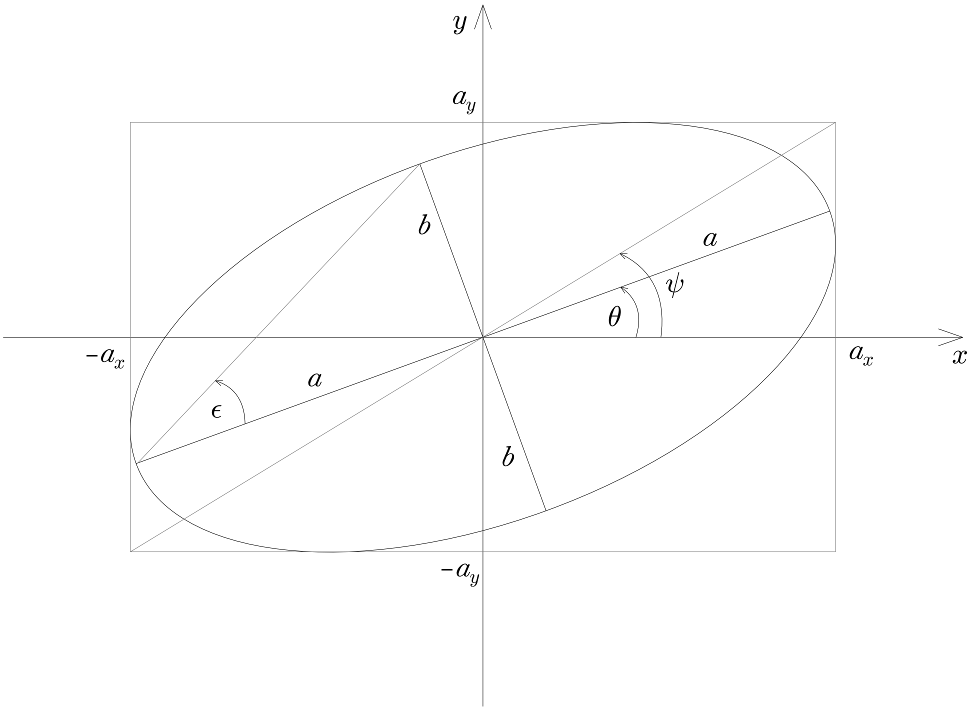

Figure 3.1: Polarization ellipse that is traced in the xy-plane by the end point of the electric field vector as time passes

Table 3.2: Special polarization states and their parameters

Pol. state	xy-plane	ψ	θ	δ	ϵ	$\vec{J}$	χ
LHP	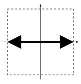	0	0	—	0	$\begin{pmatrix}1\\0\end{pmatrix}$	0
LVP	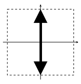	$\frac{\pi}{2}$	$\frac{\pi}{2}$	—	0	$\begin{pmatrix}0\\1\end{pmatrix}$	∞
LDP	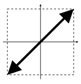	$\frac{\pi}{4}$	$\frac{\pi}{4}$	$2m\pi$	0	$\frac{1}{\sqrt{2}}\begin{pmatrix}1\\1\end{pmatrix}$	1
LAP	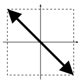	$\frac{\pi}{4}$	$\frac{3\pi}{2}$	$\pi + 2m\pi$	0	$\frac{1}{\sqrt{2}}\begin{pmatrix}1\\-1\end{pmatrix}$	-1
RCP	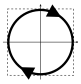	$\frac{\pi}{4}$	—	$\frac{\pi}{2} + 2m\pi$	$\frac{\pi}{4}$	$\frac{1}{\sqrt{2}}\begin{pmatrix}1\\i\end{pmatrix}$	i
LCP	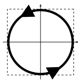	$\frac{\pi}{4}$	—	$-\frac{\pi}{2} + 2m\pi$	$-\frac{\pi}{4}$	$\frac{1}{\sqrt{2}}\begin{pmatrix}1\\-i\end{pmatrix}$	$-i$

Note: $m \in \mathbb{Z}$

4. Ellipsometry

This chapter will provide an introduction to ellipsometry and will be mainly focused on methods and configurations relevant to our experimental work.

By the words of Azzam and Bashara (1977, p. v): *"Ellipsometry is an optical technique for the characterization of, and observations of events at, an interface or film between two media and is based on exploiting the polarization transformations that occur as a beam of polarized light is reflected from or transmitted through the interface or film."*

4.1 Generalized complex ellipsometric parameters

In the previous chapter, we described the effect of the non-depolarizing linear optical system on the polarization state of the uniform transverse monochromatic EM plane-wave via Eq. (3.6), i.e.

$$\begin{pmatrix} E^f_{0x} \\ E^f_{0y} \end{pmatrix} = \begin{pmatrix} M_{xx} & M_{xy} \\ M_{yx} & M_{yy} \end{pmatrix} \begin{pmatrix} E^i_{0x} \\ E^i_{0y} \end{pmatrix},$$

from which the elements of the Jones matrix can be expressed as

$$M_{xx} = \left(\frac{E^f_{0x}}{E^i_{0x}}\right)_{E^i_{0y}=0}, \qquad M_{xy} = \left(\frac{E^f_{0x}}{E^i_{0y}}\right)_{E^i_{0x}=0}, \tag{4.1a}$$

$$M_{yx} = \left(\frac{E^f_{0y}}{E^i_{0x}}\right)_{E^i_{0y}=0}, \qquad M_{yy} = \left(\frac{E^f_{0y}}{E^i_{0y}}\right)_{E^i_{0x}=0}. \tag{4.1b}$$

Another way to describe the polarization change is via Eq. (3.16)

$$\chi_f = \frac{M_{yx} + M_{yy}\chi_i}{M_{xx} + M_{xy}\chi_i},$$

which is a bilinear transformation, containing neither the absolute phase nor the absolute amplitude (i.e. the intensity of light). For a unique description of this bilinear transformation, 3 complex parameters are needed (Azzam and Bashara, 1977, Ch. 3.2). One of the ways these so-called *generalized complex ellipsometric parameters* can be defined in the linear polarization states basis $\mathcal{B}_{XY} = (\vec{x}, \vec{y})$ is:

$$\rho = \frac{M_{yy}}{M_{xx}} = \left(\frac{E^f_{0y}}{E^i_{0y}}\right)_{E^i_{0x}=0} \left(\frac{E^i_{0x}}{E^f_{0x}}\right)_{E^i_{0y}=0} = \tan\Psi e^{i\Delta}, \tag{4.2a}$$

$$\rho_{xy} = \frac{M_{xy}}{M_{yy}} = \left(\frac{E^f_{0x}}{E^f_{0y}}\right)_{E^i_{0x}=0} = \left(\chi^{iy}_f\right)^{-1} = \tan\Psi_{xy} e^{i\Delta_{xy}}, \tag{4.2b}$$

$$\rho_{yx} = \frac{M_{yx}}{M_{xx}} = \left(\frac{E^f_{0y}}{E^f_{0x}}\right)_{E^i_{0y}=0} = \chi^{ix}_f = \tan\Psi_{yx} e^{i\Delta_{yx}}. \tag{4.2c}$$

As indicated above, the interpretation is straightforward. Firstly, ρ is the ratio of the relative LVP and LHP complex amplitude changes between the initial and final states. Secondly, the initial LVP state ($\chi_i^{iy} = \infty$) is transformed by the optical system to the final state χ_f^{iy}, which corresponds to the inverse value of ρ_{xy}. Thirdly, the initial LHP state ($\chi_i^{ix} = 0$) is transformed to the final state χ_f^{ix}, which corresponds to ρ_{yx}. Finally, $\Psi, \Delta, \Psi_{xy}, \Delta_{xy}, \Psi_{yx}$ and Δ_{yx} simply provide an alternative expression of the respective complex numbers and are called *generalized ellipsometric angles.*

The bilinear transformation can be rewritten in terms of these parameters as

$$\chi_f = \frac{\rho_{yx}\rho + \chi_i}{\rho^{-1} + \rho_{xy}\chi_i}. \tag{4.3}$$

When the two eigenpolarizations of the optical system are known, the Jones matrix representation in the basis of these eigenpolarizations $\mathcal{B} = \left(\vec{b}_1, \vec{b}_2\right)$ is diagonal, i.e.

$$\begin{pmatrix} E_1^f \\ E_2^f \end{pmatrix} = \begin{pmatrix} M_{11} & 0 \\ 0 & M_{22} \end{pmatrix} \begin{pmatrix} E_1^i \\ E_2^i \end{pmatrix}, \tag{4.4}$$

and the bilinear transformation becomes linear, i.e.

$$[\chi_f]^{\mathcal{B}} = \frac{M_{22}}{M_{11}} \left[\chi^i\right]^{\mathcal{B}} = [\rho]^{\mathcal{B}} [\chi_i]^{\mathcal{B}}. \tag{4.5}$$

In other words, the polarization transformation is in this case uniquely determined by two complex polarization parameters χ_1 and χ_2 (represented in the basis $\mathcal{B}_{XY}$) and $[\rho]^{\mathcal{B}}$, a *complex ellipsometric parameter* given by the ratio of diagonal elements of the Jones matrix represented with respect to the eigenpolarizations basis $\mathcal{B}$. It is important to note that the linear polarization basis is usually chosen in such a way that $\vec{x} = \vec{s}$ is normal to the plane of incidence on an interface of the optical system (i.e. *senkrecht* polarization) and $\vec{y} = \vec{p}$ is in the plane of incidence (i.e. *parallel* polarization). The keyword *generalized* refers to the situation when the Jones matrix in the linear polarization basis $(\vec{s}, \vec{p})$ is not diagonal.

4.2 Ellipsometer configurations

There are several possible experimental configurations of an ellipsometer (Azzam and Bashara, 1977, ch. 3). In the most basic configuration PSA, unpolarized light emitted from a source L is polarized by a linear polarizer P and interacts with a sample S, after which light passes through an analyzer A (another linear polarizer) and is finally detected by a detector D. Additional polarization devices are often placed in the optical system (see Fig. 4.1), such as compensators C (linear retarders) and phase modulators M (devices with time-varying phase retardation caused by either stress or alignment). The polarization state can be determined by the configuration, in which the outgoing intensity vanishes (*null ellipsometry*), or, in the case of *photometric ellipsometry*, it is deduced from a variation of the detected intensity as a function of configuration parameters, such as angle of incidence, phase retardation and orientations of polarizers or other optical elements with respect to coordinate axes. Depending on the parameter that is being varied, we talk about *Rotating Polarizaer* (RPE), *Rotating Analyzer* (RAE), *Rotating Compensator* (RCE) or *Phase Modulation* (PME) *Ellipsometries.*

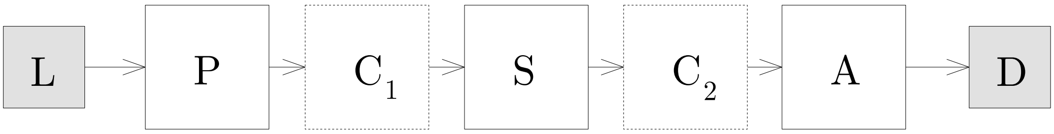

Figure 4.1: Ellipsometer configuration with two compensators (one before and the other after the sample)

4.2.1 RAE of a sample with linear eigenpolarizations in PSA configuration

Supposing the Jones matrix of a sample is diagonal, the polarization axes of a polarizer and an analyzer make the angles β, α, respectively, with the x-axis. Using the Jones formalism, we can compute the polarization transformation for an ellipsometer in the PSA configuration as

$$\begin{pmatrix} E^f_{0x} \\ E^f_{0y} \end{pmatrix} = \begin{pmatrix} \cos^2\alpha & \sin\alpha\cos\alpha \\ \sin\alpha\cos\alpha & \sin^2\alpha \end{pmatrix} \begin{pmatrix} M_{xx} & 0 \\ 0 & M_{yy} \end{pmatrix} \begin{pmatrix} E^i_0\cos\beta \\ E^i_0\sin\beta \end{pmatrix} \tag{4.6}$$

$$= E^i_0 M_{xx} \begin{pmatrix} \cos\beta\cos^2\alpha + \rho\sin\beta\sin\alpha\cos\alpha \\ \cos\beta\sin\alpha\cos\alpha + \rho\sin\beta\sin^2\alpha \end{pmatrix}. \tag{4.7}$$

The intensity detected by the detector is proportional to the norm of the Jones vector of the final state, therefore,

$$I = I_0\Big[\cos^2\beta\cos^2\alpha + |\rho|^2\sin^2\beta\sin^2\alpha + \frac{1}{2}\sin 2\beta\sin 2\alpha\,\mathrm{Re}\{\rho\}\Big]. \tag{4.8}$$

By setting $\beta = \pi/4$ and varying α, we obtain the intensity dependence

$$I(\alpha) = A\cos^2\alpha + B\sin^2\alpha + C\sin 2\alpha + D, \quad \text{with} \quad A, B, C, D \in \mathbb{R}, \tag{4.9}$$

that can be fitted to the data. From the ratios

$$\frac{B}{A} = |\rho|^2, \tag{4.10}$$

$$\frac{C}{A} = \mathrm{Re}\{\rho\} \tag{4.11}$$

of the fitted coefficients A, B and C the values of $|\rho|$ and $\mathrm{Re}\{\rho\}$ can be extracted, leaving only the sign of $\mathrm{Im}\{\rho\}$ unknown. This problem can be solved by adding another element to the system, as can be seen in the example in Sec. 4.2.2.

4.2.2 RAE of a sample with general elliptic eigenpolarizations in PSA and PSCA configurations

Let us consider an ellipsometer in the PSCA configuration (see Fig. 4.2) with all its elements fixed except for the analyzer A, which can be rotated about the z-axis by an angle α. The polarization axis of the polarizer P and the fast axis of the compensator C are parallel to the y-axis. The polarization transformation can be computed using the Jones formalism in the following way:

$$\begin{pmatrix} E_{0x}^f \\ E_{0y}^f \end{pmatrix} = \begin{pmatrix} \cos^2\alpha & \sin\alpha\cos\alpha \\ \sin\alpha\cos\alpha & \sin^2\alpha \end{pmatrix} \begin{pmatrix} e^{-i\Gamma} & 0 \\ 0 & 1 \end{pmatrix} \begin{pmatrix} M_{xx} & M_{xy} \\ M_{yx} & M_{yy} \end{pmatrix} \begin{pmatrix} 0 \\ E_{0y}^i \end{pmatrix} \tag{4.12}$$

$$= E_{0y}^i M_{yy} \begin{pmatrix} \rho_{xy} e^{-i\Gamma}\cos^2\alpha + \cos\alpha\sin\alpha \\ \rho_{xy} e^{-i\Gamma}\cos\alpha\sin\alpha + \sin^2\alpha \end{pmatrix}. \tag{4.13}$$

Again, we calculate the norm of the transformed Jones vector to obtain the intensity variation

$$I = I_0\Big[\sin^2\alpha + (\mathrm{Re}\{\rho_{xy}\}\cos\Gamma + \mathrm{Im}\{\rho_{xy}\}\sin\Gamma)\sin 2\alpha + |\rho_{xy}|^2\cos^2\alpha\Big]. \tag{4.14}$$

Measuring the intensity for different values of the angle α both in the PSA and PSCA configurations and fitting an intensity function

$$I(\alpha) = A\sin^2 + B\sin 2\alpha + C\cos^2\alpha + D \quad \text{with} \quad A, B, C, D \in \mathbb{R} \tag{4.15}$$

to these measurements allows for the determination of the generalized complex ellipsometric parameter ρ_{xy}. By comparison to Eq. (4.14), we gain the relation

$$K = \frac{B}{A} = \mathrm{Re}\{\rho_{xy}\}\cos\Gamma + \mathrm{Im}\{\rho_{xy}\}\sin\Gamma \tag{4.16}$$

that binds the fitted coefficients A and B to ρ_{xy} through the linear retardance Γ. To extract both complex parts of ρ_{xy}, first, we determine the ratio K in the PSA configuration when $\Gamma = 0$, to determine the real part

$$\mathrm{Re}\{\rho_{xy}\} = K_{PSA}, \tag{4.17}$$

then, the imaginary part can be computed from the measurement in the PSCA configuration ($\Gamma \neq 0$) as follows:

$$\mathrm{Im}\{\rho_{xy}\} = \frac{K_{PSCA} - K_{PSA}\cos\Gamma}{\sin\Gamma}. \tag{4.18}$$

The polarization change caused by the sample induces the azimuth and ellipticity changes

$$\theta_{iy} = \frac{1}{2}\arctan\frac{2\,\mathrm{Re}\{\rho_{xy}\}}{1 - |\rho_{xy}|^2}, \tag{4.19}$$

$$\epsilon_{iy} = \frac{1}{2}\arcsin\frac{2\,\mathrm{Im}\{\rho_{xy}\}}{1 + |\rho_{xy}|^2}, \tag{4.20}$$

respectively. These changes are usually referred to via the underlying phenomena that is being observed. When the optical anisotropy is induced by an external magnetic field and we observe polarization changes in the reflection setting, i.e. the magneto-optical Kerr effect (MOKE), they are referred to as the Kerr azimuth $\theta_{Ky} = \theta_{iy}$ and the Kerr ellipticity $\epsilon_{Ky} = \epsilon_{iy}$. Note that if we continued to follow the convention of describing the polarization state, when it is observed against the direction of propagation, we could account account for the change in the clockwise and anticlockwise directions due to the reflection by changing the sing of Eqs. 4.19 and 4.20. However, in Chapter 5, a fixed coordinate system is used, therefore, we will lean towards the definition without the sign change.

Supposing the polarization change is small, the absolute values $|\rho_{xy}|, |\rho_{yx}|$ are also small, and therefore its squares can be neglected (we can set $C \approx 0$ in Eq. (4.15)). It is also justified to use approximate relations

$$\theta_{iy} \approx \mathrm{Re}\{\rho_{xy}\}, \tag{4.21}$$

$$\epsilon_{iy} \approx \mathrm{Im}\{\rho_{xy}\}, \tag{4.22}$$

following from Eqs. (3.14a), (3.14b) or (3.15).

In the case of normal incidence ($\varphi^{(0)} = 0$), the Jones matrix of a sample $\mathbb{M}$ must be invariant under the rotation operation, i.e.

$$\begin{pmatrix} \cos\xi & \sin\xi \\ -\sin\xi & \cos\xi \end{pmatrix} \begin{pmatrix} M_{xx} & M_{xy} \\ M_{yx} & M_{yy} \end{pmatrix} \begin{pmatrix} \cos\xi & -\sin\xi \\ \sin\xi & \cos\xi \end{pmatrix} = \begin{pmatrix} M_{xx} & M_{xy} \\ M_{yx} & M_{yy} \end{pmatrix}, \tag{4.23}$$

therefore

$$M_{xx} = M_{yy}, \tag{4.24}$$

$$M_{xy} = -M_{yx}, \tag{4.25}$$

and subsequently from Eq. (4.2)

$$\rho_{xy} = -\rho_{yx} \tag{4.26}$$

must hold.

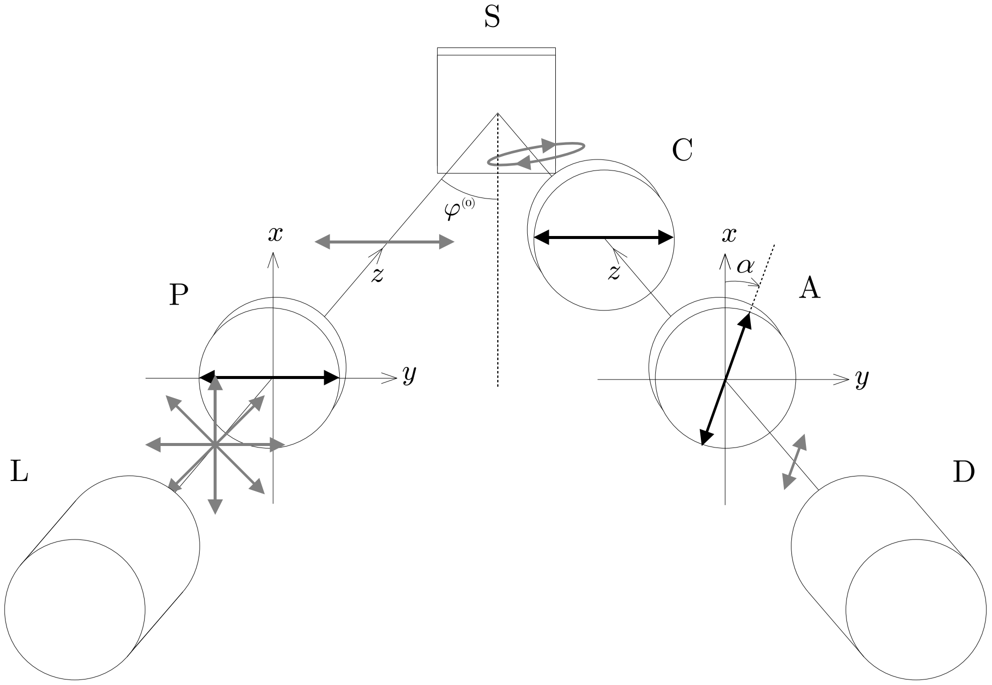

Figure 4.2: Reflection RAE setup in PSCA configuration

4.3 Analysis of ellipsometric measurements

The main goal of the analysis of ellipsometric data is to gain information about the sample properties. Only in a few special cases does the electro-magnetic theory provide a direct expression into which the data can be simply plugged and the unknown properties obtained.

One such example is a planar interface between two isotropic media (indexed i and j), where the reflection and transmission are governed by the Fresnel complex-amplitude reflection r and transmission t coefficients for $\vec{s}$ and $\vec{p}$ polarizations (Azzam and Bashara, 1977, Ch. 4.2)

$$r_s^{(ij)} = \frac{N^{(i)} \cos\phi^{(i)} - N^{(j)} \cos\phi^{(j)}}{N^{(i)} \cos\phi^{(i)} + N^{(j)} \cos\phi^{(j)}}, \quad r_p^{(ij)} = \frac{N^{(j)} \cos\phi^{(i)} - N^{(i)} \cos\phi^{(j)}}{N^{(j)} \cos\phi^{(i)} + N^{(i)} \cos\phi^{(j)}}, \tag{4.27a}$$

$$t_s^{(ij)} = \frac{2N^{(i)} \cos\phi^{(i)}}{N^{(i)} \cos\phi^{(i)} + N^{(j)} \cos\phi^{(j)}}, \quad t_p^{(ij)} = \frac{2N^{(i)} \cos\phi^{(i)}}{N^{(j)} \cos\phi^{(i)} + N^{(i)} \cos\phi^{(j)}}, \tag{4.27b}$$

where N denotes relevant complex indices of refraction and ϕ are angles of deviation from the normal of the interface in the relevant medium. The ratio of the amplitude reflection coefficients yield the ellpsometric parameter of the interface

$$\rho^{(ij)} = \frac{r_p^{(ij)}}{r_s^{(ij)}}$$

and with the help of Snell's law $N^{(i)} \sin\phi^{(i)} = N^{(j)} \sin\phi^{(j)}$, one can derive an explicit expression for the relative permittivity of the second medium

$$\varepsilon^{(j)} = \varepsilon^{(i)} \sin^2\phi^{(i)} \left[1 + \left(\frac{1-\rho^{(ij)}}{1+\rho^{(ij)}} \right)^2 \tan^2\phi^{(i)} \right]. \tag{4.28}$$

This expression is sufficiently accurate in many practical applications when multiple reflections need not to be considered, such as for absorbing bulk materials.

We will now add complexity to our previous example by considering a thin non-amplifying isotropic laterally infinite film (medium 1) with two plane-parallel boundaries between two isotropic half-spaces (media 0 and 2). For each interface (01 and 12), the Fresnel amplitude coefficients still apply individually. The multiple reflection in the film manifests itself in the form of a geometric series[1] in the expressions for the global reflection coefficients for s and p polarizations (Azzam and Bashara, 1977, Ch. 4.3)

$$r_s = r_s^{(01)} + t_s^{(01)} t_s^{(10)} r_s^{(12)} e^{-2i\beta} \sum_{m=0}^{\infty} \left(r_s^{(10)} r_s^{(12)} e^{-2i\beta} \right)^m, \tag{4.29a}$$

$$r_p = r_p^{(01)} + t_p^{(01)} t_p^{(10)} r_p^{(12)} e^{-2i\beta} \sum_{m=0}^{\infty} \left(r_p^{(10)} r_p^{(12)} e^{-2i\beta} \right)^m, \tag{4.29b}$$

where

$$\beta = \frac{\omega}{c} N^{(1)} d \tag{4.30}$$

---

[1] We implicitly assume full coherence of the interfering waves. Throughout this thesis we focus on monochromatic plane-waves, which are fully coherent.

is the phase thickness of the film (d is its thickness). After evaluating the sums and further algebraic manipulation from this model, one obtains the ellipsometric parameter

$$\rho = \frac{r_p}{r_s} = \frac{r_p^{(01)} + r_p^{(12)} e^{-2i\beta}}{1 + r_p^{(01)} r_p^{(12)} e^{-2i\beta}} \frac{1 + r_s^{(01)} r_s^{(12)} e^{-2i\beta}}{r_s^{(01)} + r_s^{(12)} e^{-2i\beta}}. \tag{4.31}$$

The unknown parameters of the film (thickness d and relative permittivity $\varepsilon^{(1)}$) cannot be simply expressed from Eq. (4.31), but one has to employ numerical methods.

It is common practice to extract unknown information about the system through a regression algorithm (see Fig. 4.3) that compares the experimental data to the theoretical model. More complex theoretical models can contain multiple isotropic or anisotropic layers (their thicknesses and permittivity tensor elements), such as the one introduced in Ch. 5. Other models can include surface oxidation or roughness (Hilfiker and Tompkins, 2016, Ch. 8) and more. For the regression analysis to be successful, the number of unknown properties should not exceed the amount of information stored in the experimental data. This requirement is, in most cases, met quite easily, while the problem is strongly overdetermined. When fitting the data, one should also consider the global behavior of an estimator like *Mean Squared Error* (MSE), which quantifies the agreement between the model data and the experimental data. The majority of local minima of MSE are usually distinguishable by eye from the desired global minimum.

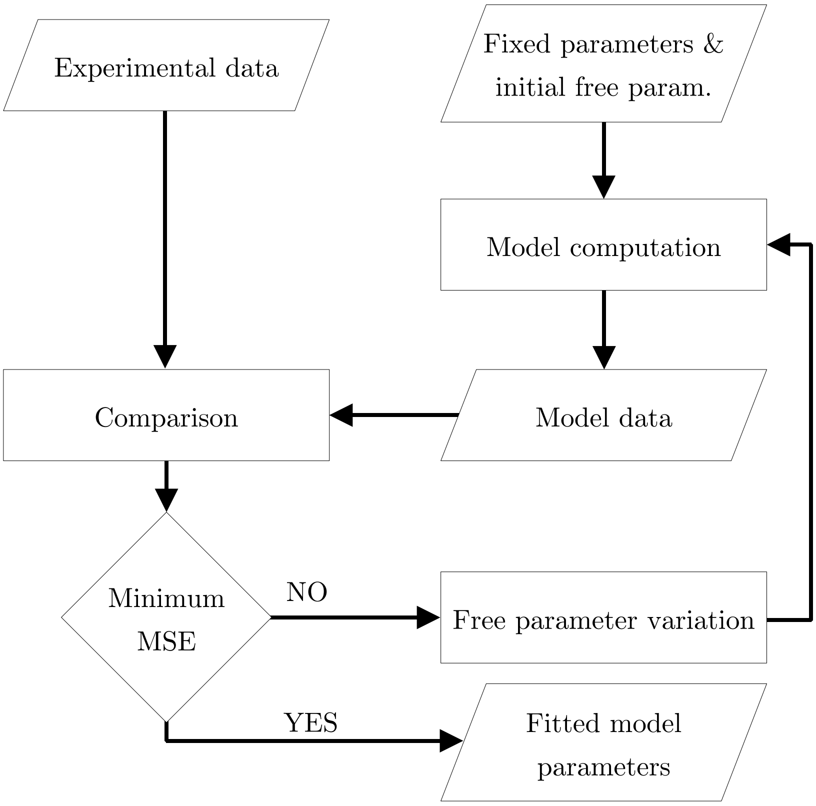

Figure 4.3: Regression algorithm flowchart for the analysis of ellipsometric data using a theoretical model with free and fixed parameters

5. Propagation of Light in Stratified Media

In this chapter, we will compute the magneto-optical response of a stratified structure consisting of $\mathcal{N}$ homogeneous layers with plane-parallel boundaries using a 4×4 matrix formalism introduced by Yeh (1980) that was originally intended to describe non-absorbing birefringent layered media (permittivity is a real symmetric tensor) and was later generalized to absorbing layered magnetically ordered media by Višňovský (1986). A brief overview of the latter formalism is provided below. For a more in-depth discussion, we refer to the textbooks (Yeh, 2005; Višňovský, 2006).

5.1 Monochromatic plane-wave solution

Without any loss of generality, we can choose a Cartesian coordinate system defined by the unit vectors $\vec{x}, \vec{y}$ and $\vec{z}$, where the z-axis is normal to the interfaces and the x-axis is normal to the plane of incidence (see Fig. 5.1). We also assume that the half-spaces denoted by 0 and $\mathcal{N}+1$ are isotropic, and the incident light is coming from the half-space 0. Each layer is characterized by its relative permittivity tensor

$$\hat{\varepsilon}^{(n)} = \begin{pmatrix} \varepsilon_{xx}^{(n)} & \varepsilon_{xy}^{(n)} & \varepsilon_{xz}^{(n)} \\ \varepsilon_{yx}^{(n)} & \varepsilon_{yy}^{(n)} & \varepsilon_{yz}^{(n)} \\ \varepsilon_{zx}^{(n)} & \varepsilon_{zy}^{(n)} & \varepsilon_{zz}^{(n)} \end{pmatrix}, \forall n \in \{1, ..., \mathcal{N}\} \tag{5.1}$$

and its thickness $d^{(n)}$.

As was discussed in the first chapter, at optical frequencies, the effect of the magnetic field of incident light can be neglected. The relative permeability tensor therefore assumes for all layers a simple form $\mu_{ij}^{(n)} = \delta_{ij}$. From Maxwell's equations

$$\nabla \times \vec{B} - \frac{1}{c^2}\frac{\partial}{\partial t}\left(\hat{\varepsilon}\vec{E}\right) = 0, \tag{5.2a}$$

$$\nabla \times \vec{E} - \frac{\partial \vec{B}}{\partial t} = 0, \tag{5.2b}$$

$$\nabla \cdot \left(\hat{\varepsilon}\vec{E}\right) = 0, \tag{5.2c}$$

$$\nabla \cdot \vec{B} = 0, \tag{5.2d}$$

a wave equation for the electric field in the n-th layer

$$\nabla^2 \vec{E}^{(n)} - \nabla\left(\nabla \cdot \vec{E}^{(n)}\right) - \hat{\varepsilon}\frac{1}{c^2}\frac{\partial^2 \vec{E}^{(n)}}{\partial t^2} = 0 \tag{5.3}$$

can be derived. A monochromatic plane-wave solution in the n-th layer of Eq. (5.3)

$$\vec{E}^{(n)} = \vec{E}_0^{(n)} \exp\left[i\left(\omega t - \vec{\gamma}^{(n)} \cdot \vec{r}\right)\right] \tag{5.4}$$

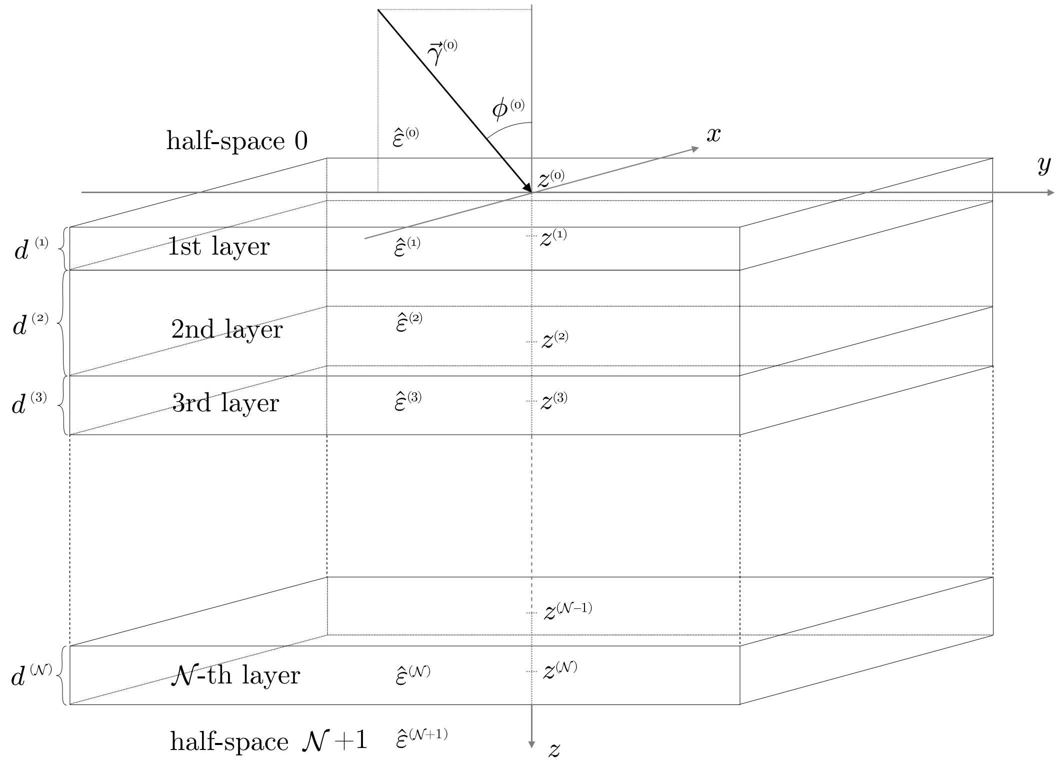

Figure 5.1: Stratified structure consisting of $\mathcal{N}$ (generally anisotropic) layers between two isotropic half-spaces

obeys the vector eigenmode equation

$$\gamma^{(n)2}\vec{E}_0^{(n)} - \vec{\gamma}^{(n)}\left(\vec{\gamma}^{(n)} \cdot \vec{E}_0^{(n)}\right) - \hat{\varepsilon}^{(n)}\frac{\omega^2}{c^2}\vec{E}_0^{(n)} = 0, \tag{5.5}$$

where

$$\vec{\gamma}^{(n)} = \frac{\omega}{c}\left(N_x^{(n)}\vec{x} + N_y^{(n)}\vec{y} + +N_z^{(n)}\vec{z}\right) \tag{5.6}$$

is the propagation vector in the n-th layer.

It is important to note that Eqs. (5.2) take into account only the linear response. Therefore, the Fourier components do not mix, and we can solve the problem individually for each frequency and propagation vector. Also, to avoid any confusion, we need to keep in mind that the chosen time variation $\exp(i\omega t)$ in Eq. (5.4) leads to a complex refractive index in the form $\operatorname{Re} N_i^{(n)} - i \operatorname{Im} N_i^{(n)}$, which subsequently lead to the complex permittivity tensor element in the form $\operatorname{Re}\varepsilon_{ij}^{(n)} - i \operatorname{Im}\varepsilon_{ij}^{(n)}$.

Using the complex indices of refraction N_i and Einstein's summation convention, we can rewrite Eq. (5.5) in Cartesian components as

$$\left(N_i^{(n)}N_i^{(n)} - N_i^{(n)}N_j^{(n)} - \varepsilon_{ij}^{(n)}\right)E_{0j}^{(n)} = 0, \quad i, j \in \{x, y, z\}. \tag{5.7}$$

For this system of equations to have a solution, its determinant must be zero

$$\begin{vmatrix} N_y^{(n)2} + N_z^{(n)2} - \varepsilon_{xx}^{(n)} & -N_x^{(n)}N_y^{(n)} - \varepsilon_{xy}^{(n)} & -N_x^{(n)}N_z^{(n)} - \varepsilon_{xz}^{(n)} \\ -N_y^{(n)}N_x^{(n)} - \varepsilon_{yx}^{(n)} & N_x^{(n)2} + N_z^{(n)2} - \varepsilon_{yy}^{(n)} & -N_y^{(n)}N_z^{(n)} - \varepsilon_{yz}^{(n)} \\ -N_z^{(n)}N_x^{(n)} - \varepsilon_{zx}^{(n)} & -N_z^{(n)}N_y^{(n)} - \varepsilon_{zy}^{(n)} & N_x^{(n)2} + N_y^{(n)2} - \varepsilon_{zz}^{(n)} \end{vmatrix} = 0. \tag{5.8}$$

The boundary conditions on each interface require a continuity of propagation vector components parallel to the interface, i.e. $\forall n \in \{0, ..., \mathcal{N}+1\}$:

$$\vec{\gamma}^{(n)} \cdot \vec{x} = \frac{\omega}{c} N_x, \tag{5.9}$$

$$\vec{\gamma}^{(n)} \cdot \vec{y} = \frac{\omega}{c} N_y, \tag{5.10}$$

where $N_x = 0$ (since we have chosen the x-axis to be normal to the plane of incidence) and $N_y = N_y^{(0)}$. Therefore, only the z-component of the propagation vector

$$\vec{\gamma}^{(n)} = \frac{\omega}{c}\Big(N_y \vec{y} + +N_z^{(n)} \vec{z}\Big) \tag{5.11}$$

is layer-dependent. This substantially simplifies the condition for the determinant

$$\begin{vmatrix} N_y^2 + N_z^{(n)2} - \varepsilon_{xx}^{(n)} & -\varepsilon_{xy}^{(n)} & -\varepsilon_{xz}^{(n)} \\ -\varepsilon_{yx}^{(n)} & N_z^{(n)2} - \varepsilon_{yy}^{(n)} & -N_y N_z^{(n)} - \varepsilon_{yz}^{(n)} \\ -\varepsilon_{zx}^{(n)} & -N_z^{(n)} N_y - \varepsilon_{zy}^{(n)} & N_y^2 - \varepsilon_{zz}^{(n)} \end{vmatrix} = 0 \tag{5.12}$$

and produces an algebraic equation of the 4th order. Therefore, we have four eigenvectors (modes) $\vec{E}_{0j}^{(n)} = E_{0j}^{(n)} \vec{e}_j^{(n)}$ that are characterized by their complex amplitude $E_{0j}^{(n)}$ at the interface between the n-th and the $(n+1)$-st layer (i.e. $z = z^{(n)}$) and the unit polarization vector

$$\vec{e}_j^{(n)} = C_j^{(n)} \begin{pmatrix} -\varepsilon_{xy}^{(n)}\Big(\varepsilon_{xy}^{(n)} - N_y^2\Big) + \varepsilon_{xz}^{(n)}\Big(\varepsilon_{zy}^{(n)} - N_y N_{zj}^{(n)}\Big) \\ \Big(\varepsilon_{zz}^{(n)} - N_y^2\Big)\Big(\varepsilon_{xx}^{(n)} - N_y^2 - N_{zj}^{(n)2}\Big) - \varepsilon_{xz}^{(n)}\varepsilon_{zx}^{(n)} \\ -\Big(\varepsilon_{xx}^{(n)} - N_y^2 - N_{zj}^{(n)2}\Big)\Big(\varepsilon_{zy}^{(n)} - N_y N_{zj}^{(n)}\Big) + \varepsilon_{zx}^{(n)}\varepsilon_{xy}^{(n)} \end{pmatrix}, \tag{5.13}$$

which follows from Eq. (5.7) for eigenvectors. $C_j^{(n)}$ is the corresponding normalization factor. The electric field in each layer can be written as a superposition of these modes, i.e.

$$\vec{E}^{(n)}(z) = \sum_{j=1}^{4} E_{0j}^{(n)} \vec{e}_j^{(n)} \exp\Big[i\omega t - i\frac{\omega}{c}\Big(N_y y + N_{zj}^{(n)}(z - z^{(n)})\Big)\Big], z^{(n-1)} \leq z \leq z^{(n)}. \tag{5.14}$$

The magnetic flux density of the electric field amplitude eigenvectors can be found using the Faraday law, i.e. Eq. (5.2b), as follows:

$$-i\vec{\gamma}_j^{(n)} \times \vec{E}_j^{(n)} + i\omega \vec{B}_j^{(n)} = 0, \tag{5.15}$$

$$\vec{B}_j^{(n)} = \frac{1}{c}\Big(N_y \vec{y} + N_{zj}^{(n)} \vec{z}\Big) \times \vec{E}_j^{(n)}. \tag{5.16}$$

The magnetic flux density in the n-th layer can also be written as such superposition of eigenvectors

$$\vec{B}^{(n)}(z) = \frac{1}{c} \sum_{j=1}^{4} E_{0j}^{(n)} \vec{b}_j^{(n)} \exp\Big[i\omega t - i\frac{\omega}{c}\Big(N_y y + N_{zj}^{(n)}(z - z^{(n)})\Big)\Big], z^{(n-1)} \leq z \leq z^{(n)}, \tag{5.17}$$

where

$$\begin{aligned}\vec{b}_j^{(n)} &= \left(N_y\vec{y} + N_{zj}^{(n)}\vec{z}\right) \times \vec{e}_j^{(n)} && (5.18)\\ &= C_j^{(n)} \begin{pmatrix} \left(\varepsilon_{xx}^{(n)} - N_y^2 - N_{zj}^{(n)2}\right)\left(N_{zj}^{(n)}\varepsilon_{zz}^{(n)} + N_y\varepsilon_{zy}^{(n)}\right) + \varepsilon_{zx}^{(n)}\left(N_y\varepsilon_{xy}^{(n)} + N_{zj}^{(n)}\varepsilon_{xz}^{(n)}\right) \\ N_{zj}^{(n)}\left[-\varepsilon_{xy}^{(n)}\left(\varepsilon_{zz}^{(n)} - N_y^2\right) + \varepsilon_{xz}^{(n)}\left(\varepsilon_{zy}^{(n)} + N_yN_{zj}^{(n)}\right)\right] \\ -N_y\left[-\varepsilon_{xy}^{(n)}\left(\varepsilon_{zz}^{(n)} - N_y^2\right) + \varepsilon_{xz}^{(n)}\left(\varepsilon_{zy}^{(n)} + N_yN_{zj}^{(n)}\right)\right] \end{pmatrix} && (5.19)\end{aligned}$$

is the polarization vector of the j-th magnetic flux density eigenvector in the n-th layer.

5.2 Višňovský-Yeh's 4×4 matrix formalism

Boundary conditions require continuity of the tangential components of the electric field and the magnetic flux density. Therefore, the set of conditions

$$\vec{E}^{(n-1)}(z^{(n-1)}) \cdot \vec{x} = \vec{E}^{(n)}(z^{(n-1)}) \cdot \vec{x}, \tag{5.20a}$$

$$\vec{B}^{(n-1)}(z^{(n-1)}) \cdot \vec{y} = \vec{B}^{(n)}(z^{(n-1)}) \cdot \vec{y}, \tag{5.20b}$$

$$\vec{E}^{(n-1)}(z^{(n-1)}) \cdot \vec{y} = \vec{E}^{(n)}(z^{(n-1)}) \cdot \vec{y}, \tag{5.20c}$$

$$\vec{B}^{(n-1)}(z^{(n-1)}) \cdot \vec{x} = \vec{B}^{(n)}(z^{(n-1)}) \cdot \vec{x}, \tag{5.20d}$$

must be met $\forall n \in \{1, ..., \mathcal{N}+1\}$. Substituting corresponding Eqs. (5.14) and (5.17) to these continuity conditions yields

$$\sum_{j=1}^{4} \vec{E}_{0j}^{(n-1)}(z^{(n-1)})\vec{e}_j^{(n-1)} \cdot \vec{x} = \sum_{j=1}^{4} \vec{E}_{0j}^{(n)}(z^{(n)})\vec{e}_j^{(n)} \cdot \vec{x} \exp\left(i\frac{\omega}{c}N_{zj}^{(n)}d^{(n)}\right), \tag{5.21a}$$

$$\sum_{j=1}^{4} \vec{E}_{0j}^{(n-1)}(z^{(n-1)})\vec{b}_j^{(n-1)} \cdot \vec{y} = \sum_{j=1}^{4} \vec{E}_{0j}^{(n)}(z^{(n)})\vec{b}_j^{(n)} \cdot \vec{y} \exp\left(i\frac{\omega}{c}N_{zj}^{(n)}d^{(n)}\right), \tag{5.21b}$$

$$\sum_{j=1}^{4} \vec{E}_{0j}^{(n-1)}(z^{(n-1)})\vec{e}_j^{(n-1)} \cdot \vec{y} = \sum_{j=1}^{4} \vec{E}_{0j}^{(n)}(z^{(n)})\vec{e}_j^{(n)} \cdot \vec{y} \exp\left(i\frac{\omega}{c}N_{zj}^{(n)}d^{(n)}\right), \tag{5.21c}$$

$$\sum_{j=1}^{4} \vec{E}_{0j}^{(n-1)}(z^{(n-1)})\vec{b}_j^{(n-1)} \cdot \vec{x} = \sum_{j=1}^{4} \vec{E}_{0j}^{(n)}(z^{(n)})\vec{b}_j^{(n)} \cdot \vec{x} \exp\left(i\frac{\omega}{c}N_{zj}^{(n)}d^{(n)}\right), \tag{5.21d}$$

where $d^{(n)} = z^{(n)} - z^{(n-1)}$ is the thickness of the n-th layer. The last step is to rewrite this set of equations into one matrix equation

$$\begin{pmatrix} \vec{e}_1^{(n-1)} \cdot \vec{x} & \vec{e}_2^{(n-1)} \cdot \vec{x} & \vec{e}_3^{(n-1)} \cdot \vec{x} & \vec{e}_3^{(n-1)} \cdot \vec{x} \\ \vec{b}_1^{(n-1)} \cdot \vec{y} & \vec{b}_2^{(n-1)} \cdot \vec{y} & \vec{b}_3^{(n-1)} \cdot \vec{y} & \vec{b}_3^{(n-1)} \cdot \vec{y} \\ \vec{e}_1^{(n-1)} \cdot \vec{y} & \vec{e}_2^{(n-1)} \cdot \vec{y} & \vec{e}_3^{(n-1)} \cdot \vec{y} & \vec{e}_3^{(n-1)} \cdot \vec{y} \\ \vec{b}_1^{(n-1)} \cdot \vec{x} & \vec{b}_2^{(n-1)} \cdot \vec{x} & \vec{b}_3^{(n-1)} \cdot \vec{x} & \vec{b}_3^{(n-1)} \cdot \vec{x} \end{pmatrix} \begin{pmatrix} E_{01}^{(n-1)} \\ E_{02}^{(n-1)} \\ E_{03}^{(n-1)} \\ E_{04}^{(n-1)} \end{pmatrix}$$

$$= \begin{pmatrix} \vec{e}_1^{(n)} \cdot \vec{x} & \vec{e}_2^{(n)} \cdot \vec{x} & \vec{e}_3^{(n)} \cdot \vec{x} & \vec{e}_3^{(n)} \cdot \vec{x} \\ \vec{b}_1^{(n)} \cdot \vec{y} & \vec{b}_2^{(n)} \cdot \vec{y} & \vec{b}_3^{(n)} \cdot \vec{y} & \vec{b}_3^{(n)} \cdot \vec{y} \\ \vec{e}_1^{(n)} \cdot \vec{y} & \vec{e}_2^{(n)} \cdot \vec{y} & \vec{e}_3^{(n)} \cdot \vec{y} & \vec{e}_3^{(n)} \cdot \vec{y} \\ \vec{b}_1^{(n)} \cdot \vec{x} & \vec{b}_2^{(n)} \cdot \vec{x} & \vec{b}_3^{(n)} \cdot \vec{x} & \vec{b}_3^{(n)} \cdot \vec{x} \end{pmatrix} \tag{5.22}$$

$$\times \exp \begin{pmatrix} i\frac{\omega}{c}N_{z1}^{(n)}d^{(n)} & 0 & 0 & 0 \\ 0 & i\frac{\omega}{c}N_{z2}^{(n)}d^{(n)} & 0 & 0 \\ 0 & 0 & i\frac{\omega}{c}N_{z3}^{(n)}d^{(n)} & 0 \\ 0 & 0 & 0 & i\frac{\omega}{c}N_{z4}^{(n)}d^{(n)} \end{pmatrix} \begin{pmatrix} E_{01}^{(n)} \\ E_{02}^{(n)} \\ E_{03}^{(n)} \\ E_{04}^{(n)} \end{pmatrix}.$$

Defining the dynamical matrix

$$\mathbb{D}^{(n)} = \begin{pmatrix} \vec{e}_1^{(n)} \cdot \vec{x} & \vec{e}_2^{(n)} \cdot \vec{x} & \vec{e}_3^{(n)} \cdot \vec{x} & \vec{e}_3^{(n)} \cdot \vec{x} \\ \vec{b}_1^{(n)} \cdot \vec{y} & \vec{b}_2^{(n)} \cdot \vec{y} & \vec{b}_3^{(n)} \cdot \vec{y} & \vec{b}_3^{(n)} \cdot \vec{y} \\ \vec{e}_1^{(n)} \cdot \vec{y} & \vec{e}_2^{(n)} \cdot \vec{y} & \vec{e}_3^{(n)} \cdot \vec{y} & \vec{e}_3^{(n)} \cdot \vec{y} \\ \vec{b}_1^{(n)} \cdot \vec{x} & \vec{b}_2^{(n)} \cdot \vec{x} & \vec{b}_3^{(n)} \cdot \vec{x} & \vec{b}_3^{(n)} \cdot \vec{x} \end{pmatrix} \tag{5.23}$$

and the propagation matrix

$$\mathbb{P}^{(n)} = \begin{pmatrix} e^{i\frac{\omega}{c}N_{z1}^{(n)}d^{(n)}} & 0 & 0 & 0 \\ 0 & e^{i\frac{\omega}{c}N_{z2}^{(n)}d^{(n)}} & 0 & 0 \\ 0 & 0 & e^{i\frac{\omega}{c}N_{z3}^{(n)}d^{(n)}} & 0 \\ 0 & 0 & 0 & e^{i\frac{\omega}{c}N_{z4}^{(n)}d^{(n)}} \end{pmatrix} \tag{5.24}$$

of the n-th layer allows us to write the set of equations arising from the continuity conditions at the interfaces simply as

$$\mathbb{D}^{(n-1)}\vec{E}_0^{(n-1)} = \mathbb{D}^{(n)}\mathbb{P}^{(n)}\vec{E}_0^{(n)}. \tag{5.25}$$

In other words, we derived the relation

$$\vec{E}_0^{(n-1)} = \mathbb{T}^{(n-1,n)}\vec{E}_0^{(n)}, \tag{5.26}$$

connecting complex amplitudes of eigenvectors of both $\vec{E}$ and $\vec{B}$ at the opposite interfaces of the n-th layer via a transfer matrix

$$\mathbb{T}^{(n-1,n)} = \left(\mathbb{D}^{(n-1)}\right)^{-1}\mathbb{D}^{(n)}\mathbb{P}^{(n)}. \tag{5.27}$$

For the amplitudes in the half-space $\mathcal{N}+1$ at the interface $z = z^{(\mathcal{N})}$, the corresponding propagation matrix is the identity matrix, i.e.

$$\vec{E}_0^{(\mathcal{N})} = \mathbb{T}^{(\mathcal{N},\mathcal{N}+1)}\vec{E}_0^{(\mathcal{N}+1)} = \left(\mathbb{D}^{(\mathcal{N})}\right)^{-1}\mathbb{D}^{(\mathcal{N}+1)}\vec{E}_0^{(\mathcal{N}+1)}. \tag{5.28}$$

The recurrent substitution of Eq. (5.26) into itself for $n = 1, \ldots, \mathcal{N}+1$ yields a relation

$$\begin{aligned}\vec{E}_0^{(0)} &= \mathbb{T}^{(0,1)}\vec{E}_0^{(1)} = \mathbb{T}^{(0,1)}\mathbb{T}^{(1,2)}\vec{E}_0^{(2)} = \mathbb{T}^{(0,1)}\mathbb{T}^{(1,2)}\ldots\mathbb{T}^{(\mathcal{N},\mathcal{N}+1)}\vec{E}_0^{(\mathcal{N}+1)} && (5.29)\\ &= \mathbb{M}\vec{E}_0^{(\mathcal{N}+1)}, && (5.30)\end{aligned}$$

binding the amplitudes in the half-spaces 0 and $\mathcal{N}+1$. We have denoted the above matrix product

$$\mathbb{M} = \prod_{n=1}^{\mathcal{N}+1} \mathbb{T}^{(n-1,n)}, \tag{5.31}$$

which we will refer to as the matrix of the multilayer.

5.2.1 Isotropic layers

If the n-th layer (or the half-space) is isotropic, the relative permittivity can be described by a scalar

$$\varepsilon^{(n)} = N^{(n)2} = N_y^2 + N_z^{(n)2} \tag{5.32}$$

that determines the eigenvalues

$$N_{\pm z}^{(n)} = \pm\sqrt{N^{(n)2} - N_y^2} = \pm N^{(n)}\cos\phi^{(n)} \tag{5.33}$$

of the index of refraction for the propagation along the z-axis in the positive (+) and the negative (−) sense. Eq. (5.7) assumes the form

$$\begin{pmatrix} N_y^2 + N_z^{(n)2} - N^{(n)2} & 0 & 0 \\ 0 & N_z^2 - N^{(n)2} & -N_y N_z^{(n)} \\ 0 & -N_y N_z^{(n)} & N_y^2 - N^{(n)2} \end{pmatrix} \begin{pmatrix} E_{0x}^{(n)} \\ E_{0y}^{(n)} \\ E_{0z}^{(n)} \end{pmatrix} = \begin{pmatrix} 0 \\ 0 \\ 0 \end{pmatrix} \tag{5.34}$$

and yields the eigenspaces

$$\mathcal{M}_{\pm}^{\perp} = \left\{ p \begin{pmatrix} 1 \\ 0 \\ 0 \end{pmatrix} + q \begin{pmatrix} 0 \\ \mp\cos\phi^{(n)} \\ \sin\phi^{(n)} \end{pmatrix} \;\middle|\; p, q \in \mathbb{C} \right\}, \tag{5.35}$$

whose elements are orthogonal to the propagation vectors

$$\vec{\gamma}_{\pm}^{(n)} = \frac{\omega}{c} N^{(n)} \begin{pmatrix} 0 \\ \sin\phi^{(n)} \\ \pm\cos\phi^{(n)} \end{pmatrix}, \tag{5.36}$$

respectively. We can choose normalized bases of these eigenspaces, namely

$$\vec{e}_1^{(n)} = \begin{pmatrix} p \\ q\cos\phi^{(n)} \\ -q\sin\phi^{(n)} \end{pmatrix}, \qquad \vec{e}_3^{(n)} = \begin{pmatrix} -q^* \\ p^*\cos\phi^{(n)} \\ -p^*\sin\phi^{(n)} \end{pmatrix} \qquad \in \mathcal{M}_{+}^{\perp}, \tag{5.37}$$

$$\vec{e}_2^{(n)} = \begin{pmatrix} p \\ q\cos\phi^{(n)} \\ q\sin\phi^{(n)} \end{pmatrix}, \qquad \vec{e}_4^{(n)} = \begin{pmatrix} -q^* \\ p^*\cos\phi^{(n)} \\ p^*\sin\phi^{(n)} \end{pmatrix} \qquad \in \mathcal{M}_{-}^{\perp}, \tag{5.38}$$

such that for two numbers $p, q \in \mathbb{C}$ obeying the normalization condition

$$pp^* + qq^* = 1 \tag{5.39}$$

they represents orthonormal polarization vectors $(p\vec{x} + q\vec{y})$ and $(-q^*\vec{x} + p^*\vec{y})$ that are rotated about the x-axis by $\phi^{(n)}$ in the positive sense (anticlockwise when facing the x-axis), in the case of the polarization vectors $\vec{e}_1^{(n)}, \vec{e}_3^{(n)}$ of the forward-propagating modes, or rotated in the negative sense (clockwise when facing the x-axis), in the case of the polarization vectors $\vec{e}_2^{(n)}, \vec{e}_4^{(n)}$ of the backward-propagating modes.

After the computation of the magnetic flux density polarization vectors

$$\vec{b}_1^{(n)} = \begin{pmatrix} -q \\ p\cos\phi^{(n)} \\ -p\sin\phi^{(n)} \end{pmatrix}, \qquad \vec{b}_3^{(n)} = \begin{pmatrix} -p^* \\ -q\cos\phi^{(n)} \\ q^*\sin\phi^{(n)} \end{pmatrix}, \tag{5.40}$$

$$\vec{b}_2^{(n)} = \begin{pmatrix} q \\ -p\cos\phi^{(n)} \\ -p\sin\phi^{(n)} \end{pmatrix}, \qquad \vec{b}_4^{(n)} = \begin{pmatrix} p^* \\ q^*\cos\phi^{(n)} \\ q^*\sin\phi^{(n)} \end{pmatrix} \tag{5.41}$$

from Eq. (5.18), the dynamical matrix of an isotropic layer

$$\mathbb{D}^{(n)} = \begin{pmatrix} p & p & -q^* & -q^* \\ N^{(n)}p\cos\phi^{(n)} & -N^{(n)}p\cos\phi^{(n)} & -N^{(n)}q^*\cos\phi^{(n)} & -N^{(n)}q^*\cos\phi^{(n)} \\ q\cos\phi^{(n)} & q\cos\phi^{(n)} & p^*\cos\phi^{(n)} & p^*\cos\phi^{(n)} \\ -N^{(n)}q & N^{(n)}q & -N^{(n)}p^* & N^{(n)}p^* \end{pmatrix} \tag{5.42}$$

can be obtained.

5.2.2 Eigenmode polarization vector normalization

Omitting the normalization factors in Eqs. (5.13) and (5.19) is equivalent to dividing the normalized vectors by their normalization factors. The denormalized dynamical matrix of the n-th layer

$$\widetilde{\mathbb{D}}^{(n)} = \mathbb{D}^{(n)}\left(\mathbb{C}^{(n)}\right)^{-1} \tag{5.43}$$

relates to the normalized one via the normalization coefficient matrix

$$\mathbb{C}^{(n)} = \begin{pmatrix} C_1^{(n)} & 0 & 0 & 0 \\ 0 & C_2^{(n)} & 0 & 0 \\ 0 & 0 & C_3^{(n)} & 0 \\ 0 & 0 & 0 & C_4^{(n)} \end{pmatrix}. \tag{5.44}$$

Therefore, for the transfer matrix from Eq. (5.27), it follows:

$$\begin{aligned} \mathbb{T}^{(n-1,n)} &= \left(\widetilde{\mathbb{D}}^{(n-1)}\mathbb{C}^{(n-1)}\right)^{-1}\widetilde{\mathbb{D}}^{(n)}\mathbb{C}^{(n)}\mathbb{P}^{(n)} && (5.45) \\ &= \left(\widetilde{\mathbb{C}}^{(n-1)}\right)^{-1}\left(\widetilde{\mathbb{D}}^{(n-1)}\right)^{-1}\widetilde{\mathbb{D}}^{(n)}\mathbb{P}^{(n)}\mathbb{C}^{(n)} && (5.46) \\ &= \left(\mathbb{C}^{(n-1)}\right)^{-1}\widetilde{\mathbb{T}}^{(n-1,n)}\mathbb{C}^{(n)}, && (5.47) \end{aligned}$$

where we have utilized the matrix identity

$$(\mathbb{A}\mathbb{B})^{-1} = \mathbb{B}^{-1}\mathbb{A}^{-1} \tag{5.48}$$

for the product of invertible matrices $\mathbb{A}$ and $\mathbb{B}$ as well as the fact that diagonal matrices commute.

Finally, we can show that the multilayer matrix is dependent only on the normalization coefficients of the two half-spaces surrounding the multilayer, for the rest of the coefficients is canceled out in the product

$$\begin{aligned}
\mathbb{M} &= \prod_{n=1}^{\mathcal{N}+1} \left(\mathbb{C}^{(n-1)}\right)^{-1} \widetilde{\mathbb{T}}^{(n-1,n)} \mathbb{C}^{(n)} && (5.49)\\
&= \left(\mathbb{C}^{(0)}\right)^{-1} \widetilde{\mathbb{T}}^{(0,1)} \mathbb{C}^{(1)} \left(\mathbb{C}^{(1)}\right)^{-1} \widetilde{\mathbb{T}}^{(1,2)} \mathbb{C}^{(2)} \ldots \left(\mathbb{C}^{(\mathcal{N})}\right)^{-1} \widetilde{\mathbb{T}}^{(\mathcal{N},\mathcal{N}+1)} \mathbb{C}^{(\mathcal{N}+1)} && (5.50)\\
&= \left(\mathbb{C}^{(0)}\right)^{-1} \left(\prod_{n=1}^{\mathcal{N}+1}\right) \mathbb{C}^{(\mathcal{N}+1)}. && (5.51)
\end{aligned}$$

5.2.3 Generalized complex ellipsometric parameters

Assuming that the multilayer is illuminated from the half-space 0 and there is no incident light from the half-space $\mathcal{N}+1$ (i.e. $E_{02}^{(\mathbb{N}+1)} = E_{04}^{(\mathbb{N}+1)} = 0$), the complex amplitudes are bound by Eq. (5.29) in the following form:

$$\begin{pmatrix} E_{01}^{(0)} \\ E_{02}^{(0)} \\ E_{03}^{(0)} \\ E_{04}^{(0)} \end{pmatrix} = \begin{pmatrix} M_{11} & M_{12} & M_{13} & M_{14} \\ M_{21} & M_{22} & M_{23} & M_{24} \\ M_{31} & M_{32} & M_{33} & M_{34} \\ M_{41} & M_{42} & M_{43} & M_{44} \end{pmatrix} \begin{pmatrix} E_{01}^{(\mathcal{N}+1)} \\ 0 \\ E_{03}^{(\mathcal{N}+1)} \\ 0 \end{pmatrix}, \tag{5.52}$$

from which global reflection coefficients

$$r_{21} = \left(\frac{E_{02}^{(0)}}{E_{01}^{(0)}}\right)_{E_{03}^{(0)}=0} = \frac{M_{21}M_{33} - M_{23}M_{31}}{M_{11}M_{33} - M_{13}M_{31}}, \tag{5.53a}$$

$$r_{41} = \left(\frac{E_{04}^{(0)}}{E_{01}^{(0)}}\right)_{E_{03}^{(0)}=0} = \frac{M_{41}M_{33} - M_{43}M_{31}}{M_{11}M_{33} - M_{13}M_{31}}, \tag{5.53b}$$

$$r_{43} = \left(\frac{E_{04}^{(0)}}{E_{03}^{(0)}}\right)_{E_{01}^{(0)}=0} = \frac{M_{43}M_{11} - M_{41}M_{13}}{M_{11}M_{33} - M_{13}M_{31}}, \tag{5.53c}$$

$$r_{23} = \left(\frac{E_{02}^{(0)}}{E_{03}^{(0)}}\right)_{E_{01}^{(0)}=0} = \frac{M_{23}M_{11} - M_{21}M_{13}}{M_{11}M_{33} - M_{13}M_{31}} \tag{5.53d}$$

and global transmission coefficients

$$t_{11} = \left(\frac{E_{01}^{(\mathcal{N}+1)}}{E_{03}^{(0)}} \right)_{E_{03}^{(0)}=0} = \frac{M_{33}}{M_{11}M_{33} - M_{13}M_{31}}, \tag{5.54a}$$

$$t_{31} = \left(\frac{E_{03}^{(\mathcal{N}+1)}}{E_{01}^{(0)}} \right)_{E_{03}^{(0)}=0} = \frac{-M_{31}}{M_{11}M_{33} - M_{13}M_{31}}, \tag{5.54b}$$

$$t_{33} = \left(\frac{E_{03}^{(\mathcal{N}+1)}}{E_{03}^{(0)}} \right)_{E_{01}^{(0)}=0} = \frac{M_{11}}{M_{11}M_{33} - M_{13}M_{31}}, \tag{5.54c}$$

$$t_{13} = \left(\frac{E_{01}^{(\mathcal{N}+1)}}{E_{03}^{(0)}} \right)_{E_{01}^{(0)}=0} = \frac{-M_{13}}{M_{11}M_{33} - M_{13}M_{31}} \tag{5.54d}$$

are derived. The above coefficients relate the complex amplitudes of incident ($E_{01}^{(0)}, E_{03}^{(0)}$), reflected ($E_{02}^{(0)}, E_{04}^{(0)}$) and transmitted ($E_{01}^{(\mathcal{N}+1)}, E_{03}^{(\mathcal{N}+1)}$) orthogonal pairs of eigenmodes in one or both half-spaces via the Jones reflection and transmission matrices

$$\begin{pmatrix} E_{02}^{(0)} \\ E_{04}^{(0)} \end{pmatrix} = \begin{pmatrix} r_{21} & r_{23} \\ r_{41} & r_{43} \end{pmatrix} \begin{pmatrix} E_{01}^{(0)} \\ E_{03}^{(0)} \end{pmatrix}, \tag{5.55}$$

$$\begin{pmatrix} E_{01}^{(\mathcal{N}+1)} \\ E_{03}^{(\mathcal{N}+1)} \end{pmatrix} = \begin{pmatrix} t_{11} & t_{13} \\ t_{31} & t_{33} \end{pmatrix} \begin{pmatrix} E_{01}^{(0)} \\ E_{03}^{(0)} \end{pmatrix}. \tag{5.56}$$

The generalized complex ellipsometric parameters in the eigenmode basis[1]

$$\rho_{2343} = \frac{r_{23}}{r_{43}}, \qquad \rho_{4121} = \frac{r_{41}}{r_{21}}, \tag{5.57}$$

$$\rho_{1333} = \frac{t_{13}}{t_{33}}, \qquad \rho_{3111} = \frac{t_{31}}{t_{11}} \tag{5.58}$$

are in exact agreement with Eqs. (4.2) after setting $p = 1, q = 0$ (choosing a linear basis $\mathcal{B}_{xy} = (\vec{x}, \vec{y}) = (\vec{s}, \vec{p})$ of both isotropic half-spaces) and the indices transformation ($1, 2 \to x$ and $3, 4 \to y$), i.e.

$$\rho_{2343} = \frac{r_{xy}}{r_{yy}} = \rho_{xy}, \qquad \rho_{4121} = \frac{r_{yx}}{r_{xx}} = \rho_{yx} \tag{5.59}$$

in the reflection case and

$$\rho_{1333} = \frac{t_{xy}}{t_{yy}} = \rho_{xy}, \qquad \rho_{3111} = \frac{t_{yx}}{t_{xx}} = \rho_{yx} \tag{5.60}$$

in the transmission case.

---

[1] These eigenmodes are the eigenvectors of isotropic half-space and are not to be confused with the eigenpolarizations of the polarization system, in which the reflection and transmission matrices would be diagonal.

6. Experimental Setups and Numerical Computations

This chapter provides information about experimental setups and equipment used for data collection as well as the details of and approximations employed during computations of material properties via a regression analysis.

All our samples consist of 3 layers with plane-parallel boundaries, namely, the NMG layer of various compositions and thicknesses (medium 1), the 20 nm thick Cr layer (medium 2) and the MgO substrate (medium 3). For computation purposes, the surrounding medium (i.e. half-spaces 0 and 4) is considered to be a vacuum, although the ellipsometric measurements themselves were executed at atmospheric pressure.

First, we assume that all layers are homogeneous and isotropic, and the optical constants of both Cr and MgO are known. From the ellipsometric data in the zero external magnetic field, we compute the diagonal elements of the relative permittivity tensor of the NMG layer

$$\hat{\varepsilon}^{(1)}(0) = \begin{pmatrix} \varepsilon_{xx}^{(1)}(0) & 0 & 0 \\ 0 & \varepsilon_{xx}^{(1)}(0) & 0 \\ 0 & 0 & \varepsilon_{xx}^{(1)}(0) \end{pmatrix}. \tag{6.1}$$

Then, we make an assumption that by applying the external magnetic field parallel to the surface normal of the sample (parallel to the z-axis, i.e. in the out-of-plane configuration), the Cr and MgO layers remain unchanged, while the NMG layer is magnetized in the direction of the field. In this way, the symmetry of the relative permittivity tensor of the NMG layer is changed from spherical (a point group denoted in the Schönflies notation as $\mathcal{K}_h$) to that of an axial vector $\vec{M} = (0, 0, M)$ (a point group $\mathcal{C}_{\infty h}$), which corresponds to the form expressed by Eq. (2.9). While also assuming that the magnetically induced anisotropy has a negligible effect on the diagonal elements and manifests itself only in the off-diagonal elements, we can approximate the relative permittivity tensor of the NMG layer as (Višňovský, 2006, Ch. 1.6.1)

$$\hat{\varepsilon}^{(1)}(M) = \begin{pmatrix} \varepsilon_{xx}^{(1)}(M) & \varepsilon_{xy}^{(1)}(M) & 0 \\ -\varepsilon_{xy}^{(1)}(M) & \varepsilon_{xx}^{(1)}(M) & 0 \\ 0 & 0 & \varepsilon_{zz}^{(1)}(M) \end{pmatrix} \approx \begin{pmatrix} \varepsilon_{xx}^{(1)}(0) & \varepsilon_{xy}^{(1)}(M) & 0 \\ -\varepsilon_{xy}^{(1)}(M) & \varepsilon_{xx}^{(1)}(0) & 0 \\ 0 & 0 & \varepsilon_{xx}^{(1)}(0) \end{pmatrix}. \tag{6.2}$$

From this point forward, our references to either diagonal or off-diagonal elements will be meant in the sense of the above approximation.

6.1 Optical spectroscopic RCE

For the determination of the diagonal elements of the relative permittivity tensor of the NMG layer, a commercial ellipsometer J.A. Woollam RC2 with its software CompleteEASE, allowing both hardware control and subsequent data analysis. The ellipsometer has two rotating compensators (both before and after the sample) and a silicon CCD spectrometer combined with an InGaAs diode array, allowing for measurements in the spectral range from 193 nm to 1690 nm (i.e. 0.73 eV to 6.47 eV) with a resolution of 1 nm in the spectral range from 1000 nm to 1690 nm and a resolution of 2.5 nm in the spectral range from 193 nm to 1000 nm.

The spectra of ellipsometric angles $\Psi(\omega), \Delta(\omega)$ were acquired for multiple angles of incidence. CompleteEASE also possesses a library of spectra of the optical constants of many materials (including Cr and MgO) and allows a user to build a model of stratified structure and to account for other parameters, such as roughness or supposed absorption out of the measured spectral range. Through the regression analysis, one gains the spectral dependence of the optical constants of the NMG layer.

6.2 Magneto-optical spectroscopic RAE

A laser-driven lamp Energetiq EQ-99X-FC-S was used as a time-stable source of polychromatic light. It emits in the spectral range from 190 nm to 2500 nm (i.e. 0.50 eV to 6.53 eV) with a broadband optical power of 95 mW.

A sample was mounted on a pole of an electromagnet, which generates a magnetic field oriented parallel to the normal of the surface of the sample, inducing a uniform magnetization (in the same direction) of the originally isotropic NMG layer. In Section 4.2.2, we showed that a sample with general elliptic eigenpolarizations has nonzero generalized complex ellipsometric parameters ρ_{xy} and ρ_{yx} that, in the case of normal incidence, differ only in signs and can be obtained via Eqs. (4.17) and (4.18) from the measurement of the intensity dependence on the analyzer angle described by Eq. (4.15) in both PSA and PSCA configuration. Alternatively, polar MOKE at normal incidence can be described using Eqs. (4.19) and (4.20), by the Kerr azimuth θ_K and the Kerr ellipticity ϵ_K, respectively.

In the RAE ellipsometer, a computer-controlled motorized rotational mount Thorlabs K10CR1/M enables the analyzer angle α to be set with the precision of $\pm 0.14°$. In each of the intervals $[-5°, -2°]$ and $[2°, 5°]$, for 20 evenly equidistantly distributed values of the angle α, intensity spectra were measured using a spectrometer. Namely, for the temperature-dependent measurements (see Sec. 7.1.2), the spectrometer Ocean Insight QE Pro with the spectral range from 196 nm to 990 nm and the full-width at half-maximum (FWHM) resolution of 1.6 nm was used. For the two different composition series of samples with varying thickness (see Sec. 7.2.2), the spectrometer Ocean Optics USB2000+ with the spectral range from 190 nm to 892 nm and the FWHM resolution of 1.6 nm was used. The former of the two spectrometers has a thermoelectric cooling device, which dramatically reduces the effects of thermal noise and provides the spectrometer with an overall stability during longer measurements.

As was demonstrated in Sec. 2.1 from symmetry arguments, the linear polar MOKE and consequently the off-diagonal elements of the permittivity tensor are odd in magnetization. Leveraging this property, measurements were made for magnetic fields ± 1.1 T and the ratio given by Eq. (4.16) was averaged over both field orientations

$$K_{avg} = \frac{1}{2}(K(M) - K(-M)), \tag{6.3}$$

in order to dispose of optical effects that are even in magnetization.

6.3 Off-diagonal element spectra calculation of the NMG layer relative permittivity tensor

Finally, we will employ the model from Chapter 5 to compute the off-diagonal elements via a regression analysis. Fixed input parameters of our model are

1. $d^{(1)}, d^{2)}, d^{(3)}$ – thicknesses of each of the three layers,
2. $\varepsilon^{(2)}(\omega), \varepsilon^{(3)}(\omega)$ – scalar relative permittivity spectra of Cr and MgO layers, respectively,
3. $\varepsilon_{xx}^{(1)}(\omega)$ – spectra of the diagonal elements of the relative permittivity tensor of the NMG layer obtained from the optical spectroscopic RCE measurements and its regression model
4. $\theta_K(\omega), \epsilon_K(\omega)$ Kerr azimuth and Kerr ellipticity spectra from the magneto-optical spectroscopic RAE in polar geometry at normal incidence.

The remaining input material property spectra are the off-diagonal elements of the relative permittivity tensor of the NMG layer $\varepsilon_{xy}^{(1)}(\omega)$. For each energy $E = \hbar\omega$, we set this off-diagonal element to an arbitrary initial value and let it vary as a free parameter until the minimum of the MSE is reached. In this case, the MSE quantifies the difference between measured $\theta_K(\omega), \epsilon_K(\omega)$ and expected values that are obtained from the model generalized complex ellipsometric parameter (5.59) using Equations (4.19) and (4.20).

This model was implemented in a proprietary multi-paradigm programming language and numerical computing environment MATLAB R2021b developed by MathWorks.

7. Discussion of Results

The experimental part of this thesis is concerned with two main objectives. The first objective is to measure and study the optical and magneto-optical responses of a NMG thin film sample upon heating and cooling across the martensitic transformation. The second objective is to extend previous measurements (Makeš, 2021) on NMG films with a varying thickness to different stoichiometric compositions and evaluate their effects on the strain relaxation process.

It is important to point out the limitations imposed by the experimental techniques and the mathematical model described in Chapter 6. This model assumes perfectly homogeneous laterally infinite layers with plane-parallel boundaries and a linear response of each medium. It also considers the sandwitched structure as a whole, but in reality, the penetration depth is in the order of tens of nanometers due to the relatively high absorption that is characteristic of metals, and therefore parts of the structure past the penetration depth influence the optical response in an indirect manner, such as causing a substrate-induced strain in the probed depth (described by the z-axis). Moving on to the other two spatial dimensions (the xy-plane), previous studies (Thomas et al., 2008a; Onderková, 2020) of surface morphology by means of scanning electron microscopy (SEM) and atomic force microscopy (AFM) revealed macroscopic twin variants on a scale of a few micrometers and even finer structures like nanotwinning on a scale of tens of nanometers. With that being said, our light trace in reflection ellipsometry setups is a few mm in diameter, is of different shapes for various angles of incidence (i.e. differently elongated ellipses), and there is also a possible shift of the probed surface area (caused both by the change of shape and by the sample manipulation between experimental setups). As for the temporal dimension, the time periods needed for temperature stabilization, measurement preparation and the measurement itself were in the order of minutes. Hence, we are not taking into account any possible relaxation processes, such as those observed on bulk by Dejneka et al. (2012) that were reported to be in the order of hours. The aforementioned relaxation process of the real part n of the complex refractive index to its equilibrium value n_0 with respect to time t was fitted to an exponential relation

$$n(t) = n_0 \mp n_1 \exp\left(-\frac{t}{\tau}\right), \tag{7.1}$$

where τ is the relaxation time and n_1 is the excitation amplitude. The signs correspond to either heating ($-$) or cooling ($+$). In the same paper, it was shown for the incident light energy of 2 eV that both n_1 and τ tend to decrease with increasing temperature, and while at room temperature and above, τ is in the order of tens of minutes, the excitation amplitude is very small ($n_1 \lesssim 0.01$). Supposing our film sample undergoes both qualitatively and quantitatively identical relaxation process as the one described on bulk, it might cause fluctuations of n up to 0.01 in magnitude for temperatures lower than 42 °C. For higher temperatures, the excitation amplitude becomes zero. However, further investigations into the relaxation process would be necessary for more conclusive results, and the question remains whether the relaxation process in thin films really is analogous to that in bulk. To conclude, we need to keep in mind that all phenomena in the delineated scope of the above space-time imprecision are beyond the resolution of our chosen method.

As we discussed in Sec. 1.3, from the *ab initio* calculations by Entel et al. (2006), the electron transition energies are expected to be at around 1.8 eV and 2.8 eV in the austenite phase, and, in the martensite phase, they are expected to be at around 2 eV and 3 eV. Moreover, a change in the transition intensities during the phase transition is expected as well. These predictions are in agreement with the optical conductivity measurements by Zhou et al. (2002) on bulk Ni_2MnGa, which revealed two electron transitions at the energies of 1.8 eV and 3.2 eV.

7.1 Thermally-induced martensitic transformation in 400 nm thin Ni-Mn-Ga film

For our first objective, a film (grown epitaxially using magnetron sputtering on the 20nm Cr layer and the MgO substrate at 550 °C) with the nominal composition $Ni_{47}Mn_{32}Ga_{21}$ and the nominal thickness of 400 nm was used[1]. The sample was mounted on a Peltier device. The current through the device was manually set using the Keathley 2461 SourceMeter at the beginning and adjusted throughout each measurement, which caused temperature fluctuations of about 0.5 °C. The temperature was measured by the Keithley 2000 multimeter calibrated at room temperature.

A study (Thomas et al., 2008a) of a 470 nm $Ni_{52}Mn_{23}Ga_{25}$ film[2] deposited at 400 °C directly on MgO substrate concluded from XRD results that at 27 °C the film was in the 14M orthorhombic (with a monoclinic distortion of about 2.7°) martensitic phase, and at 63 °C it was in the cubic austenitic phase, therefore, at least some portion of the film undergoes phase transition. Furthermore, it was argued that a complete martensitic transformation is hindered by the presence of the substrate, and a thin constrained austenitic layer remains at the film-substrate interface. The study also found the transformation temperatures from a linear extrapolation of a low-field (0.01 T) magnetization curve. Namely, during heating, the transformation from martensite to austenite starts at 48 °C and ends at 53 °C, and during cooling, it starts at 46 °C and ends at 41 °C. Its Curie temperature was found to be 79 °C.

The magnetometry measurement of our sample, kindly provided by Verbeno (2021), indicates at least a partial phase transition. Using linear extrapolation, the transformation temperatures were determined. In this case, the transformation takes place during heating from 42 °C to 50 °C and during cooling from 44 °C to 36 °C with the temperature hysteresis of 8 °C.

7.1.1 Optical measurements in zero magnetic field

Our temperature-dependent spectra (Figs. 7.1 and 7.2) of the diagonal element of the relative permittivity tensor ε_{xx} in the zero magnetic field exhibit a characteristic metallic behavior (see Sec. 2.3 and Fig. 2.1b). Bound electron transitions

---

[1] Nominal thickness was derived from the epitaxial growth time during magnetron sputtering and the nominal composition is the composition of the crystal used as a target for sputtering.

[2] Thickness was obtained from SEM, and the composition was determined by electron dispersive X-ray (EDX) measurement with the accuracy of about 0.5 at. %.

(see Sec. 2.2 and Fig. 2.1a) are indeed observed at the expected energies. The dissipative behavior of $\operatorname{Im}\varepsilon_{xx}$ in the vicinity of the interband transition of bound electrons at the energies of 1.8 and 3.2 eV is harder to identify by eye, therefore, we will focus our analysis on the $\operatorname{Re}\varepsilon_{xx}$ spectral peaks at the energies of 1.5 eV and 2.7 eV, originating in the dispersive behavior around these transition energies. At these two spectral peaks of $\operatorname{Re}\varepsilon_{xx}$, the temperature-induced changes are the most noticeable. While at 1.5 eV(and practically for all lower energies), the real part tends to increase with increasing temperature, at 2.7 eV it decreases with increasing temperature. The real part spectrum of Beran et al. (2015) exhibits an increase for all energies in the 1.2 eV to 6.5 eV range. The same observation was made by Zhou et al. (2002), i.e. an increase of the real part in the spectral range from 1.2 eV to 4 eV, and in addition, in the spectral range from 0.5 eV to 1.2 eV, a decrease of the real part was observed. In other words, our thin film spectra behave in the opposite way with changing temperature than those measured on bulk, and also the energy, at which the increase becomes a decrease, and vice versa, with increasing temperature, is shifted from 1.2 eV to 1.5 eV. Although our measurements qualitatively differ, as we just explained, the changes are quantitatively similar, roughly 0.6 at the energies of interest (see Figs. 7.3 and 7.4).

By comparing Fig. 7.3a with Fig. 7.3b and Fig. 7.4a with Fig. 7.4b, we can notice that the shape of the hysteresis in the case of the real part is different for each of the two energies, but in the case of the imaginary part, the shape remains roughly the same.

The temperature dependences of the real and imaginary parts of the complex refractive index N (see Fig. 7.5) have the same trends (regardless of the energy) as $\operatorname{Im}\varepsilon_{xx}$. As we can see in Fig. 7.5a, during cooling (blue data points), $\operatorname{Re}N$ at 2 eV follows the same trend (an increase with increasing temperature) as was observed by Dejneka et al. (2012), and the significant non-monotonicity of the trend during heating (red data points) could be caused by the time relaxation discussed earlier.

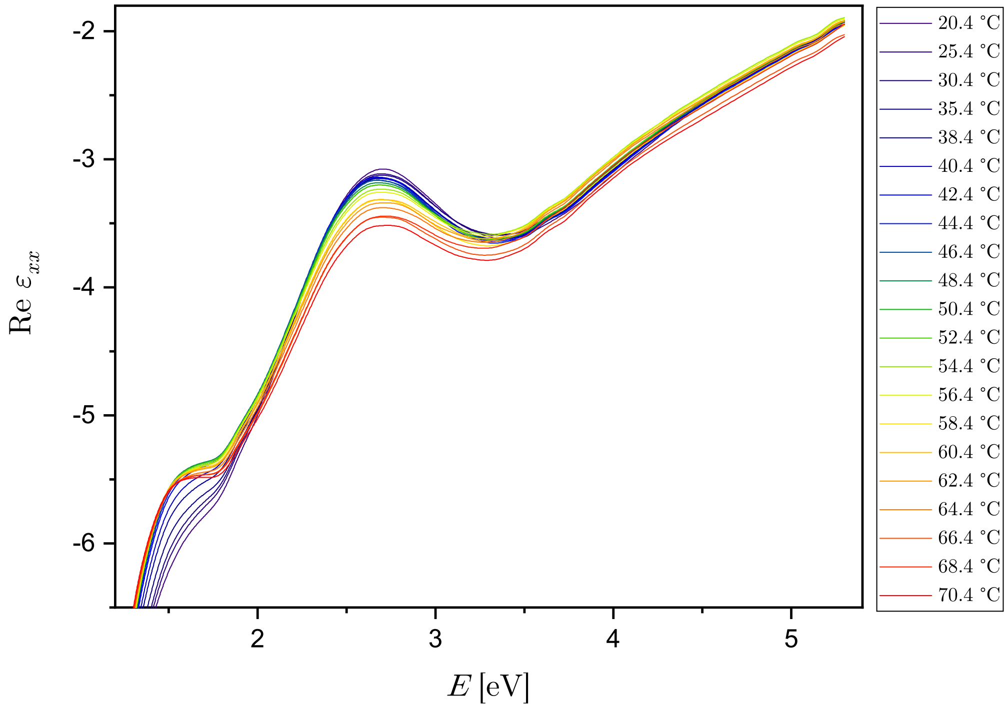

(a) Cooling

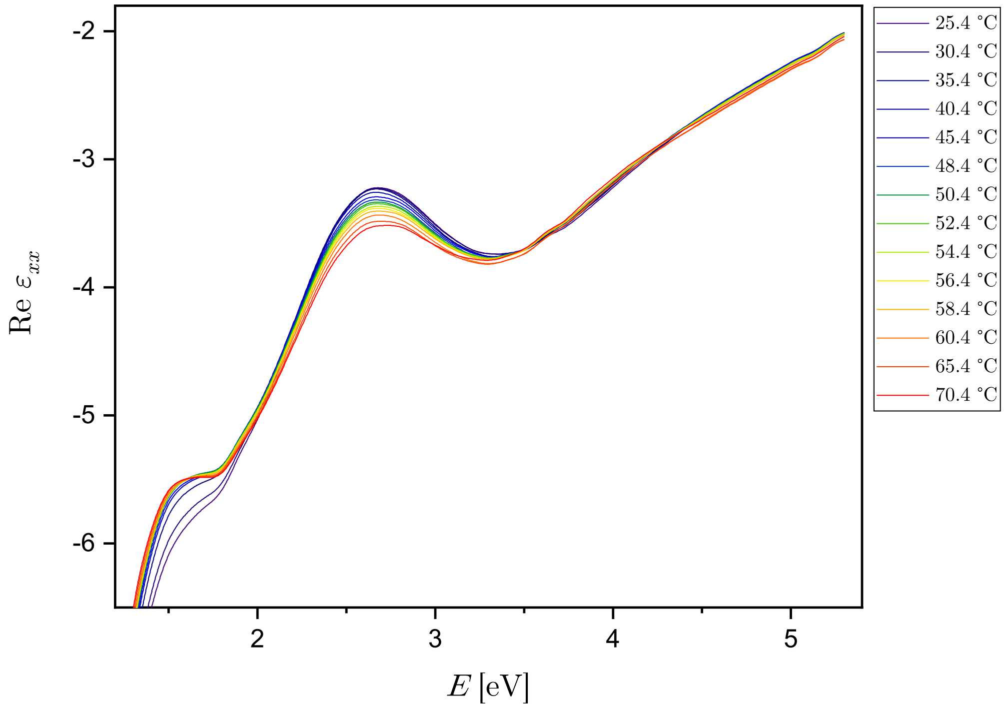

(b) Heating

Figure 7.1: Spectral dependence of the real part of the diagonal element of the relative permittivity tensor upon heating (a) and subsequent cooling (b)

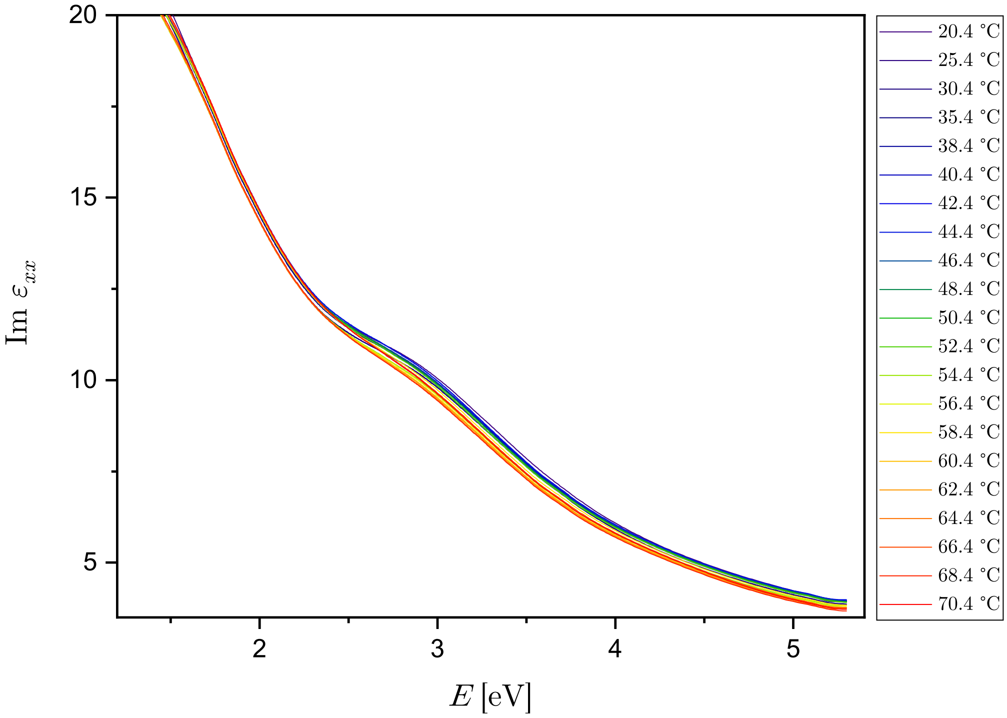

(a)

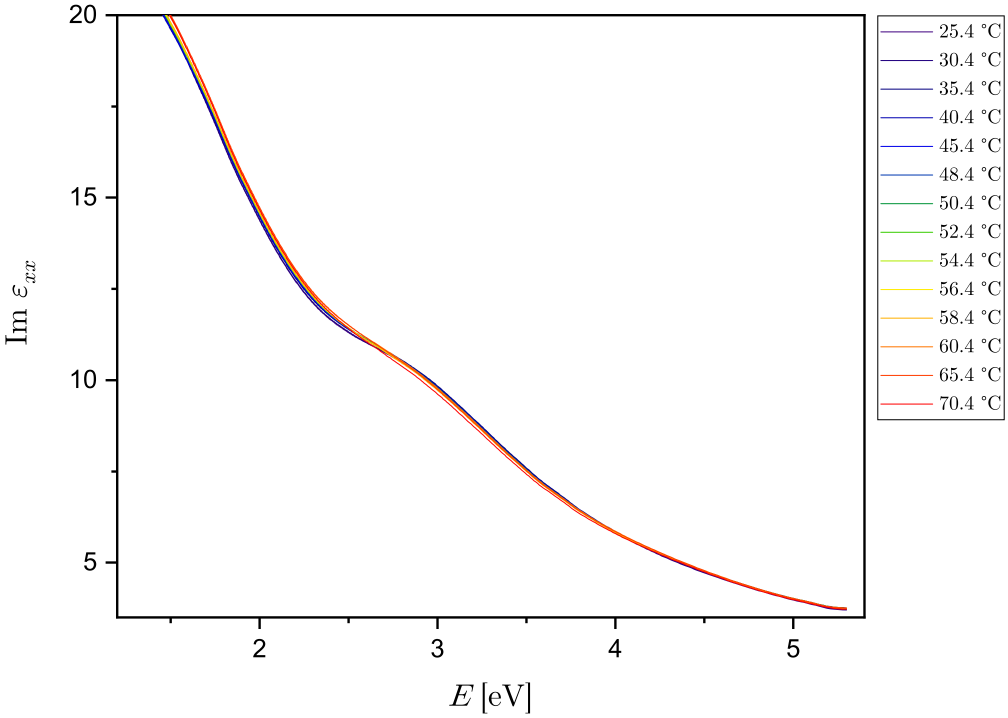

(b)

Figure 7.2: Spectral dependence of the imaginary part of the diagonal element of the relative permittivity tensor upon heating (a) and subsequent cooling (b)

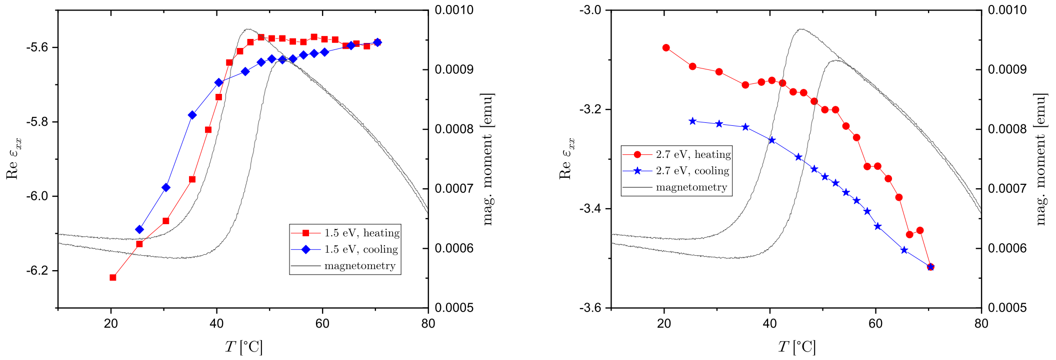

(a) (b)

Figure 7.3: Temperature dependence of the real part of the diagonal element of the relative permittivity tensor at 1.5 eV (a) and at 2.7 eV (b). Magnetometry by Verbeno (2021).

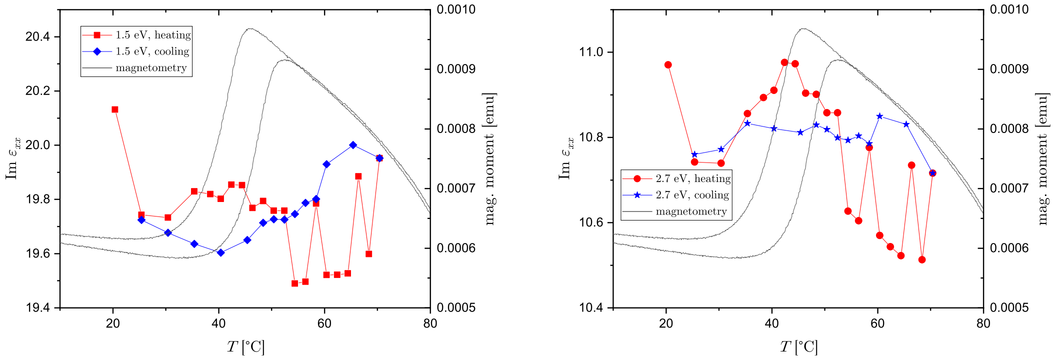

(a) (b)

Figure 7.4: Temperature dependence of the imaginary part of the diagonal element of the relative permittivity tensor at 1.5 eV (a) and at 2.7 eV (b). Magnetometry by Verbeno (2021).

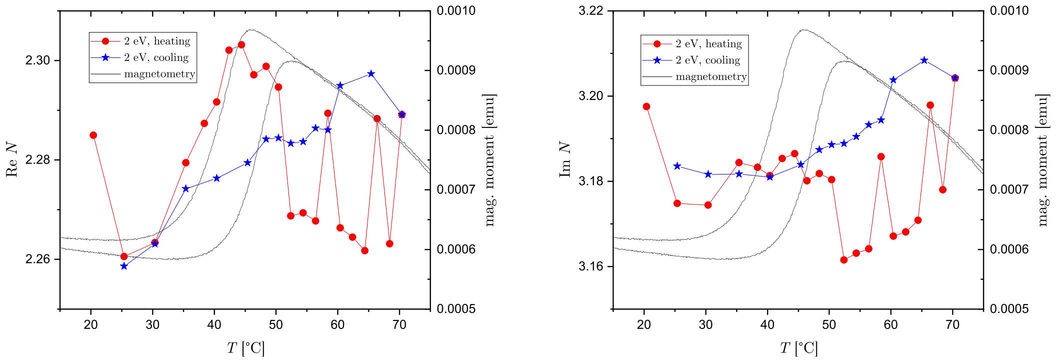

(a) (b)

Figure 7.5: Temperature dependence of the real (a) and the imaginary (b) part of the complex refractive index at 2 eV. Magnetometry by Verbeno (2021).

7.1.2 Magneto-optical measurements in polar geometry

From the temperature-dependent polar MOKE spectra (Figs. 7.6 and 7.7), we can observe three characteristic peaks of the Kerr azimuth at 1.55 eV, 2.6 eV and 3.75 eV, out of which, in our chosen sign convention, the first two are positive and the third one is negative. Similarly, three peaks of the Kerr ellipticity, shifted with respect to the peaks of the Kerr azimuth to higher energies by 0.5 eV, can be observed at 2 eV, 3 eV and 4.3 eV, where again the first two are positive and the third is negative. Both types of the MOKE spectra in the measured spectral interval have one valley, in the case of the Kerr azimuth, it is at 2.16 eV and in case of the Kerr ellipticity, it is at 2.3 eV.

The spectral structure of the Kerr azimuth in polar geometry is very similar both in shape and in magnitude to that reported on bulk $Ni_{50.1}Mn_{28.4}Ga_{21.5}$ crystal in the martensitic phase (Veis et al., 2014; Beran et al., 2015) with an important difference, i.e. bulk spectra have a negative peak at 2.16 eV instead of a positive valley.

The temperature hysteresis is apparent for all of the Kerr azimuth extrema. The peak of the Kerr azimuth at 1.55 eV (see Fig. 7.8a) follows the magnetometry curve provided by Verbeno (2021) the most precisely. During the martensite to austenite transition upon heating, the magnitude of the Kerr azimuth increases by about 0.01° at 1.55 eV, 2.16 eV and 3.75 eV, while at 2.6 eV it decreases only by 0.001 eV. Further heating past the martensitic transformation results in an overall decrease in the magnitude of the Kerr azimuth, which is to be expected since approaching the Curie temperature causes magnetic ordering to gradually disappear together with the magneto-optic effects. The temperature hysteresis of the Kerr ellipticity spectra (Fig. 7.7) is much less apparent due to the chaotic behavior of gradual changes during the heating process at 2 eV and 2.3 eV (Figs. 7.9a and 7.9b, resp.), but it is clearly visible at 3 eV and 4.3 eV (Figs. 7.9c and 7.9d, resp.).

Another thing to notice is that the three Kerr ellipticity spectra belonging to the temperatures 56.4 °C, 58.4 °C and 60.4 °C during heating stand out from their temperature-adjacent measurements (see Fig. 7.7a and the corresponding data points in Fig. 7.9). Interestingly enough, during the cooling process (see Fig. 7.7b), no such striking difference between adjacent temperatures in the Kerr ellipticity spectra was observed.

This sudden spectral change in the Kerr ellipticity during heating could be attributed to increased surface roughness, to which the Kerr ellipticity measurements are more sensitive, as opposed to the Kerr azimuth, due to the presence of the compensator in the experimental setup. The supposed surface roughness might originate from the propagation of the phase boundary from the stress-induced austenite up to the surface, leaving progressively less space for the alignment of the remaining martensitic variants, until the film is fully transformed into the austenitic phase. However, in the zero magnetic field series of measurements, the fitted values of surface roughness are all in the range of 5 nm to 6 nm, and one would also expect to observe an increase in depolarization, which is not the case, as the depolarization at 6.47 eV remains in the range from 1 % to 3 %. Therefore, the supposed increased surface roughness seems to only appear during heating while simultaneously being exposed to the external magnetic field. Another possible explanation might be that the sample, under the aforementioned conditions, finds itself in a metastable state with its properties resembling neither the austenitic nor martensitic phases.

The spectra of the off-diagonal element of the relative permittivity tensor (Figs. 7.10 and 7.11) have similar structure to the previously discussed MOKE spectra, with $\mathrm{Re}\{\varepsilon_{xy}\}$ mirroring the behavior of θ_K and $\mathrm{Im}\{\varepsilon_{xy}\}$ mirroring the behavior of ϵ_K. To be exact, $\mathrm{Re}\{\varepsilon_{xy}\}$ has two positive peaks at 1.5 eV, 2.5 eV, one negative peak at 3.5 eV and a valley at 2.15 eV. $-\mathrm{Im}\{\varepsilon_{xy}\}$ has two positive peaks at 1.9 eV, 3 eV, one negative peak at 4.2 eV and a valley at 2.3 eV. Temperature hystereses of these extrema of both parts (Figs. 7.12 and 7.13) are completely analogous to their corresponding counterparts in MOKE spectra (Figs. 7.8 and 7.9). According to Kramers-Kronig's relations (2.15), one should observe inflection points of the real part at the extrema of the imaginary part and vice versa. Indeed, this requirement is clearly satisfied for all pairs of related spectra.

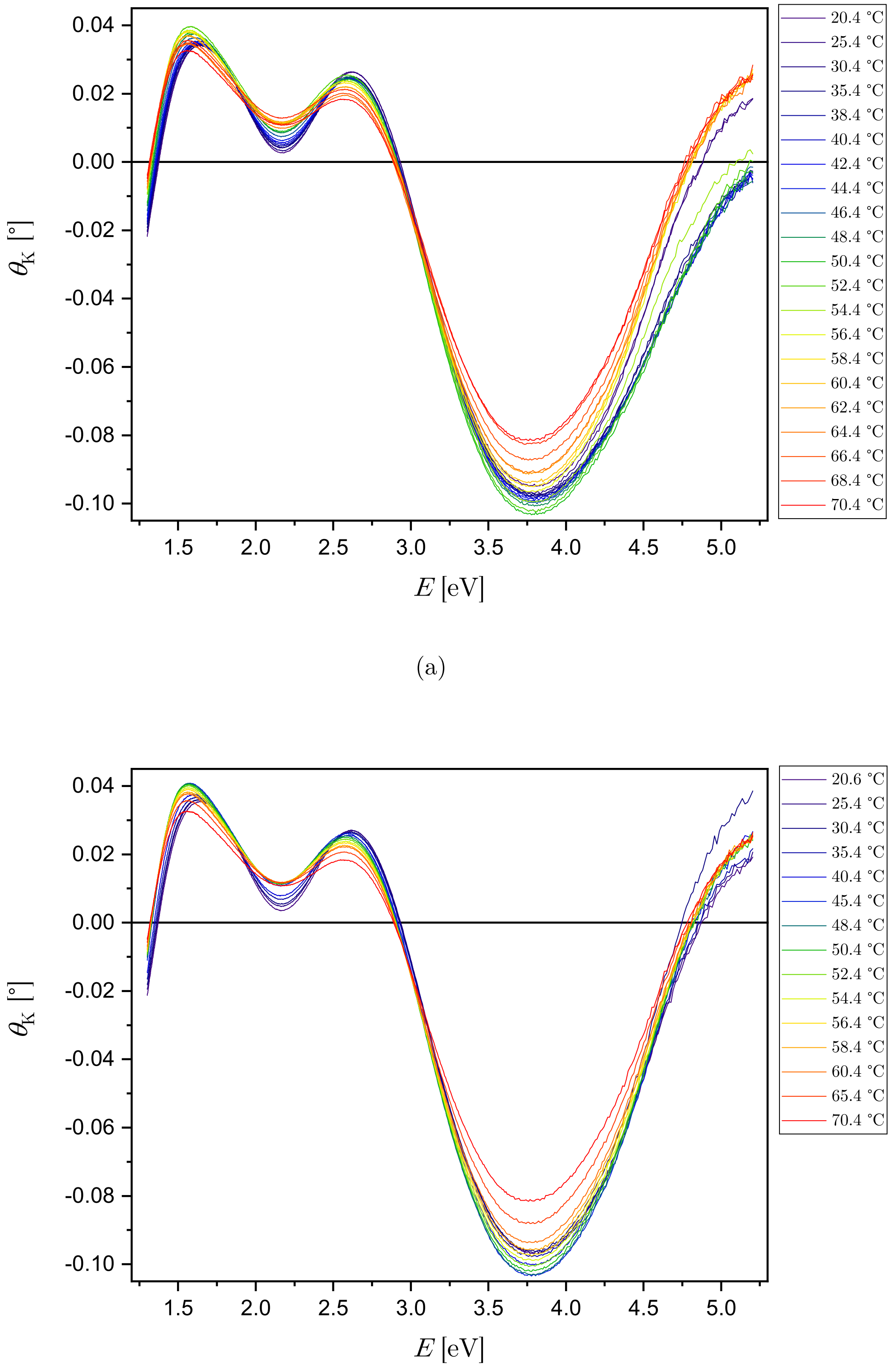

(a)

(b)

Figure 7.6: Temperature dependence of the Kerr azimuth spectra in polar geometry upon heating (a) and subsequent cooling (b)

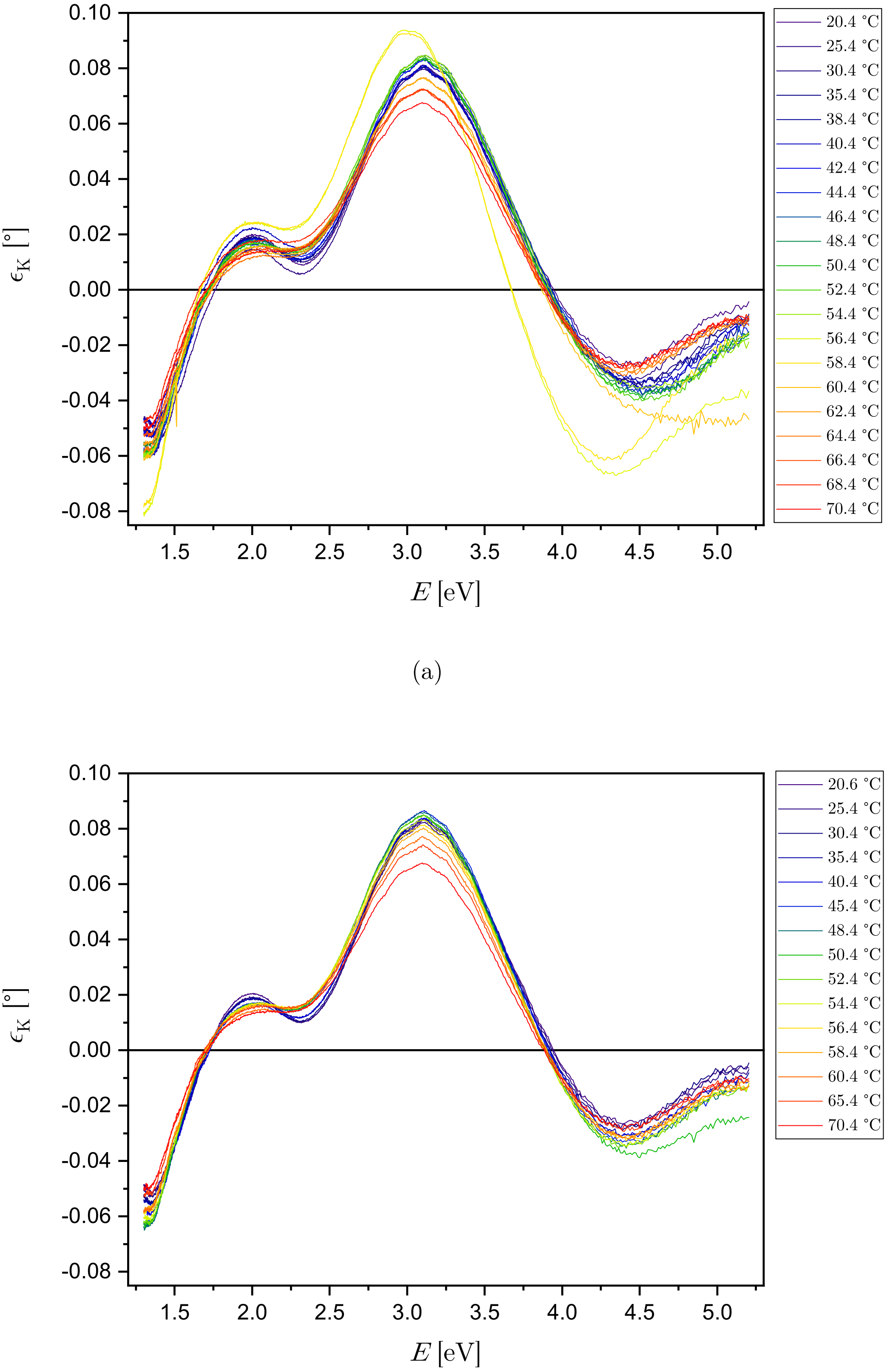

(a)

(b)

Figure 7.7: Temperature dependence of the Kerr ellipticity spectra in polar geometry upon heating (a) and subsequent cooling (b)

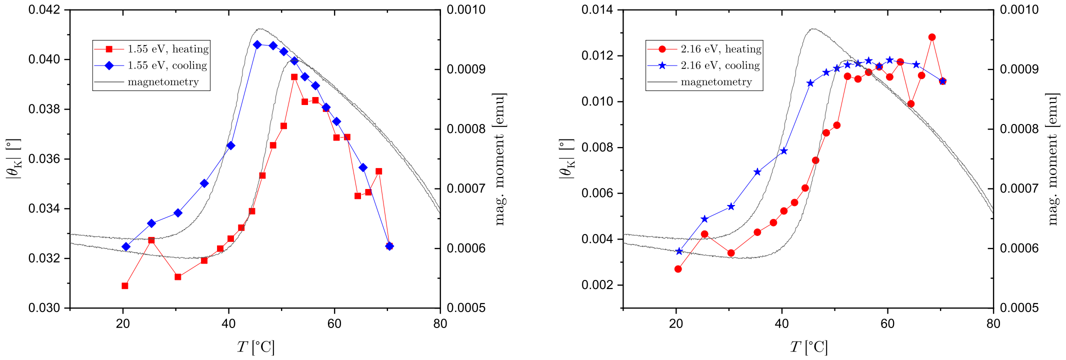

(a) Peak at 1.55 eV

(b) Valley at 2.16 eV

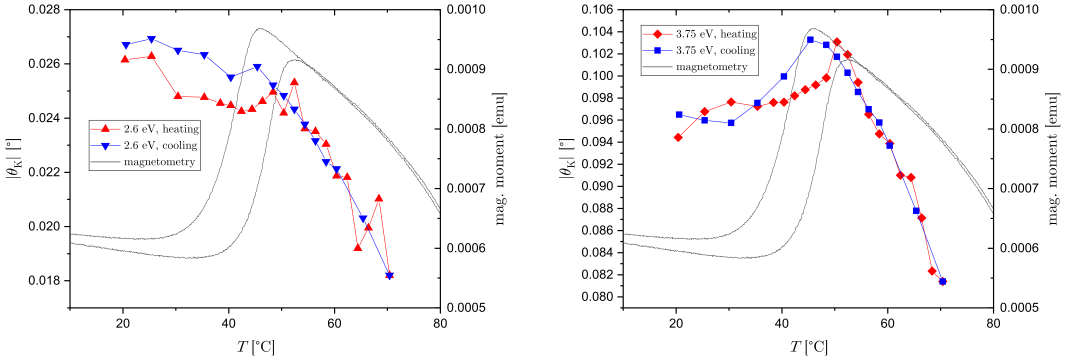

(c) Peak at 2.6 eV

(d) Peak at 3.75 eV

Figure 7.8: Temperature dependence of the absolute value of the Kerr azimuth at the energies of 1.55 eV (a), 2.16 eV (b), 2.6 eV (c) and 3.75 eV (d). Magnetometry by Verbeno (2021).

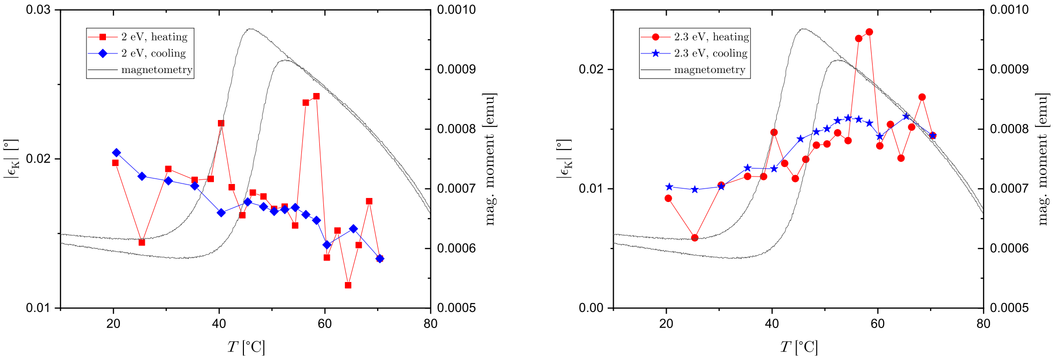

(a) Peak at 2 eV

(b) Valley at 2.3 eV

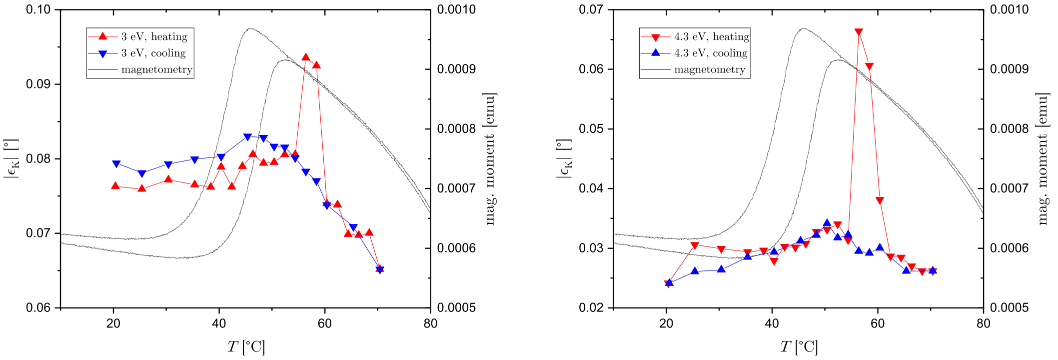

(c) Peak at 3 eV

(d) Peak at 4.3 eV

Figure 7.9: Temperature dependence of the absolute value of the Kerr ellipticity at the energies of 2 eV (a), 2.3 eV (b), 3 eV (c) and 4.3 eV (d). Magnetometry by Verbeno (2021).

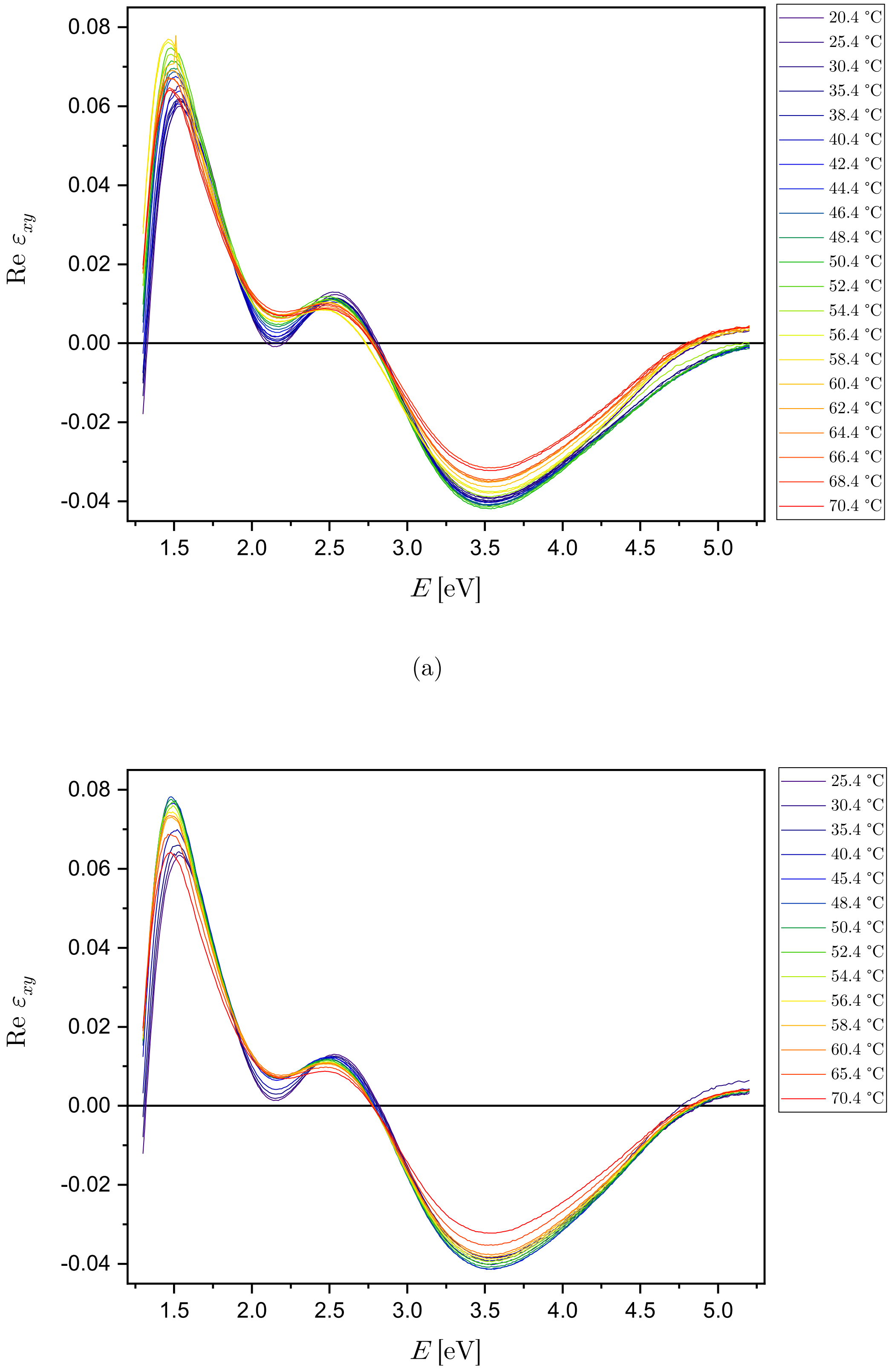

(a)

(b)

Figure 7.10: Spectral dependence of the real part of the off-diagonal element of the relative permittivity tensor upon heating (a) and subsequent cooling (b)

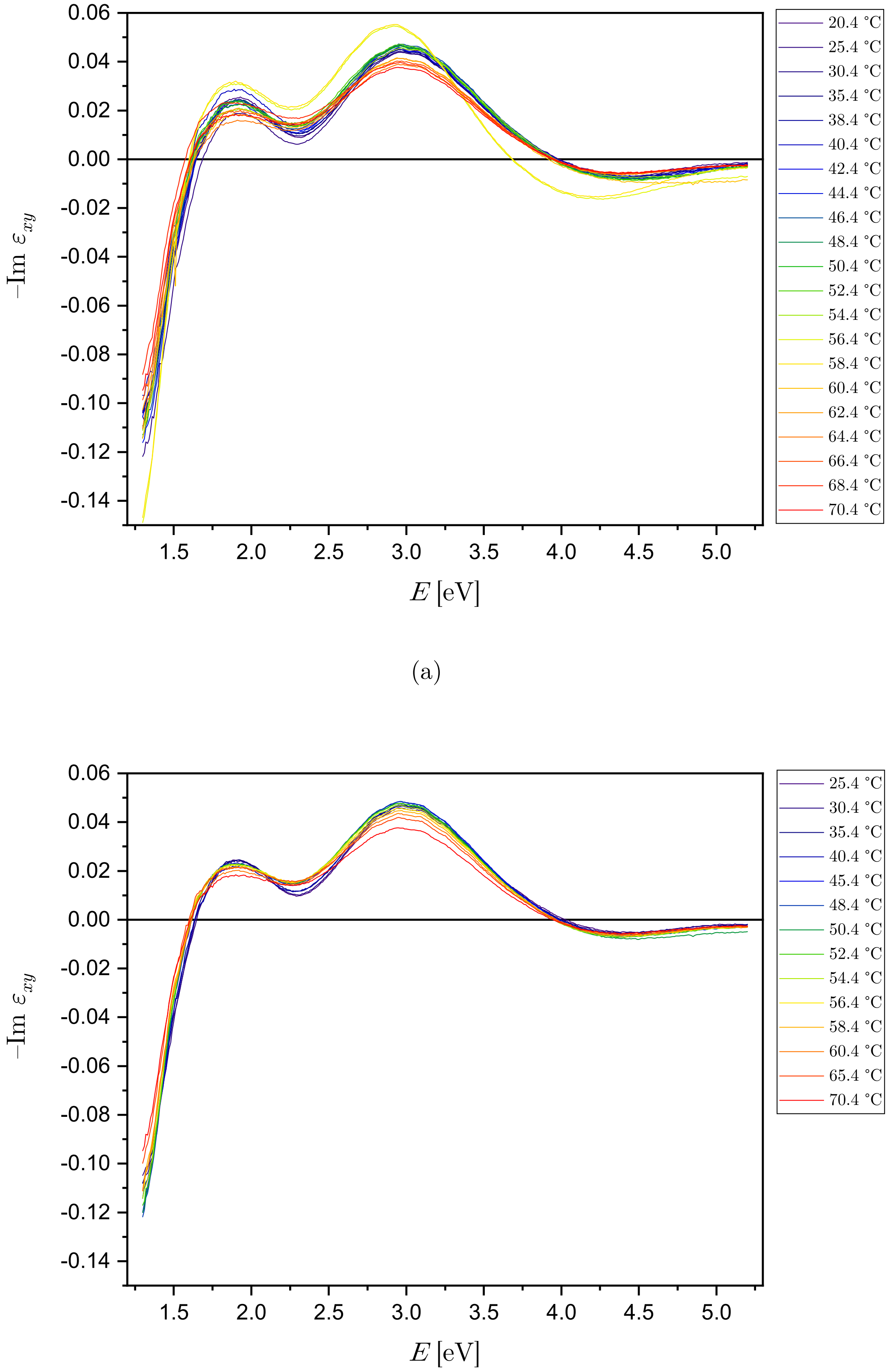

(a)

(b)

Figure 7.11: Spectral dependence of the imaginary part of the off-diagonal element of the relative permittivity tensor upon heating (a) and subsequent cooling (b)

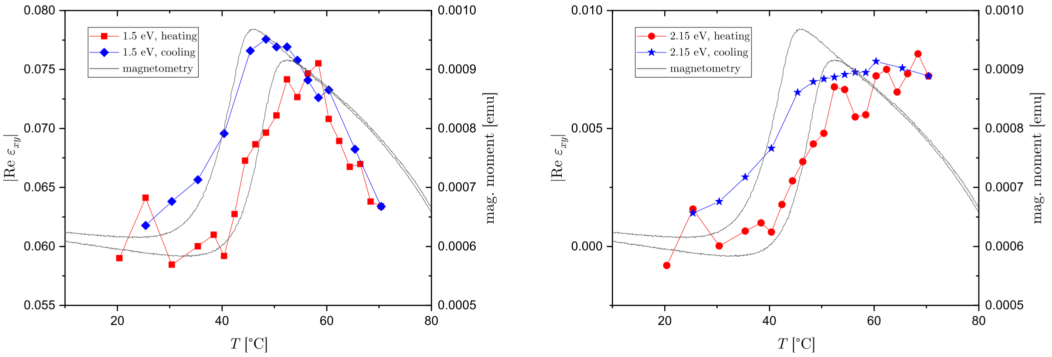

(a) Peak at 1.5 eV

(b) Valley at 2.15 eV

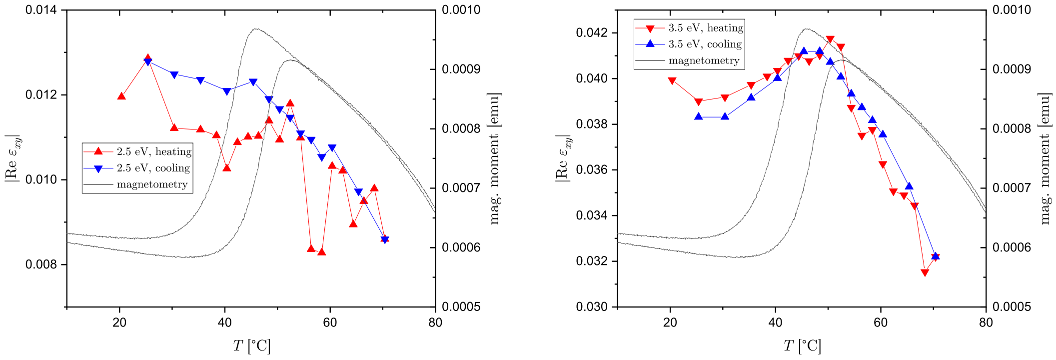

(c) Peak at 2.5 eV

(d) Peak at 3.5 eV

Figure 7.12: Temperature dependence of the absolute value of the real part of the off-diagonal element of the relative permittivity tensor at the energies of 1.5 eV (a), 2.15 eV (b), 2.5 eV (c) and 3.5 eV (d). Magnetometry by Verbeno (2021).

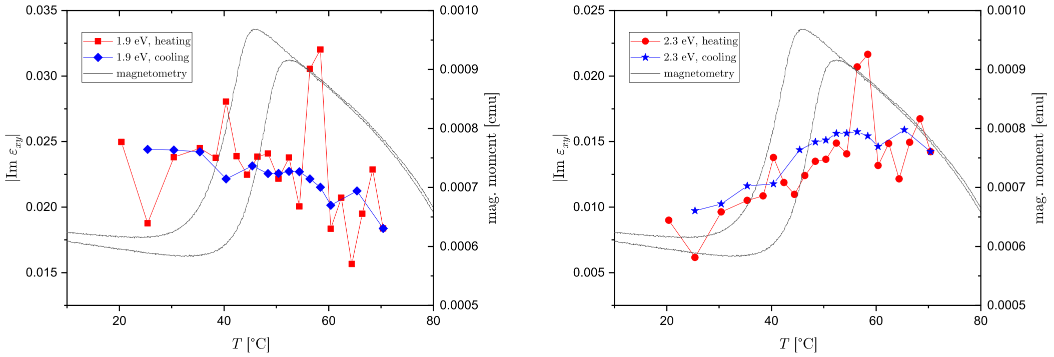

(a) Peak at 1.9 eV

(b) Valley at 2.3 eV

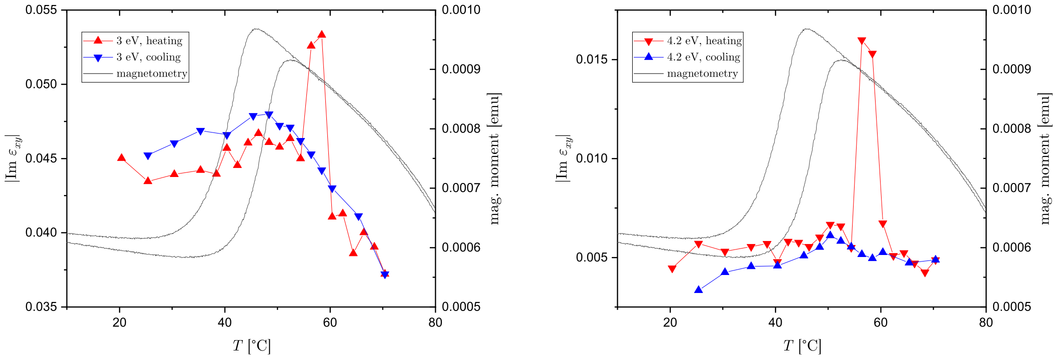

(c) Peak at 3 eV

(d) Peak at 4.2 eV

Figure 7.13: Temperature dependence of the absolute value of the imaginary part of the off-diagonal element of the relative permittivity tensor at the energies of 1.9 eV (a), 2.3 eV (b), 3 eV (c) and 4.2 eV (d). Magnetometry by Verbeno (2021).

7.2 Substrate-induced strain relaxation in thin Ni-Mn-Ga films of various thicknesses and stoichiometric compositions

One of the key differences between single crystal samples and epitaxial films is the presence of a substrate during crystal growth. The character of the substrate-film interface and its following effects on the rest of the film are determined by the choice of materials and the physical conditions during the deposition process.

During magnetron sputtering in high vacuum ($10^{-9}\,\mathrm{Pa}$), by means of which our samples were grown on MgO substrate with a 20 nm thick Cr layer, several factors have a significant influence on the film properties. The deposition temperature influences the phase, the crystallographic quality of the film and also influences the chemical composition of the film, which varies from the chemical composition of the target due to the different enthalpies of vaporization of each element present in the target, specifically (Zhang et al., 2011), the lowest enthalpy of vaporization is $225\,\mathrm{kJ\,mol^{-1}}$ for Mn, then, it is $256\,\mathrm{kJ\,mol^{-1}}$ for Ga and $379\,\mathrm{kJ\,mol^{-1}}$ for Ni. A nominal composition and a nominal thickness are derived from the chemical composition of the target and the deposition time, respectively.

An adaptive X-ray analysis (Thomas et al., 2008b) of the same NMG film on MgO substrate as in the previous paper by Thomas et al. (2008a) revealed a biaxial tensile stress of about 100 MPa (equivalent to a uniaxial compressive stress of 138 MPa). The stress increased the martensistic transformation temperature of about 63 °C and caused a tetragonal distortion of the cubic lattice[3]. At 51 °C, using linear extrapolation of a dependence of lattice parameter on tilt angle towards the surface normal, an in-plane (xy-plane) lattice parameter $a_\parallel = 0.583\,\mathrm{nm}$ and an out-of-plane lattice parameter $a_\perp = 0.579\,\mathrm{nm}$ of constrained austenite with tetragonal distortion were obtained. Therefore, in this case, the in-plane tensile strain

$$\Xi_\parallel = \frac{a_\parallel - a_0}{a_0} \tag{7.2}$$

is approximately 0.2 %. The strain is thought to originate from a substrate-film lattice parameter misfit during deposition as well as from a difference in linear thermal expansion coefficients of each material, changing the strain accordingly to the present temperature.

Taking into account the relationships between unit cell orientations (Backen et al., 2010), i.e. a cube-on-cube growth between the NMG and Cr layers, where Ni-Mn-Ga(100)[001]‖Cr(100)[001], and a 45° relative rotation between the unit cells of Cr and MgO, where Cr(100)[011]‖MgO (100)[001], the in-plane strain originating from the lattice mismatch can be estimated as

$$\Xi_\parallel^{(\mathrm{mismatch})} = \frac{2a_{\mathrm{Cr}} - a_{\mathrm{NMG}}}{a_{\mathrm{NMG}}} + \frac{\sqrt{2}a_{\mathrm{MgO}} - 2a_{\mathrm{Cr}}}{a_{\mathrm{Cr}}}. \tag{7.3}$$

After substituting the cubic lattice parameters $a_{\mathrm{NMG}} = 0.5822\,\mathrm{nm}$ (Martynov and Kokorin, 1992), $a_{\mathrm{Cr}} = 0.2885\,\mathrm{nm}$ (Koumelis, 1973) and $a_{\mathrm{MgO}} = 0.4194\,\mathrm{nm}$ (Thomas et al., 2008a), the two addends in Eq. (7.3) yield the in-plane strain

---

[3] A stress free lattice parameter is $a_0 = 0.582\,\mathrm{nm}$ (Martynov and Kokorin, 1992).

estimations of $-0.9\,\%$ and $2.8\,\%$, respectively. Although the total in-plane strain of $1.9\,\%$ is practically the same as in the case without the Cr layer, i.e.

$$\Xi_{\parallel}^{(\text{mismatch without Cr})} = \frac{\sqrt{2}a_{\text{MgO}} - a_{\text{NMG}}}{a_{\text{NMG}}}, \tag{7.4}$$

supposing at least partial relaxation takes place in the Cr layer by introducing lattice dislocations, the in-plane strain of the NMG layer is reduced.

A study conducted by Ranzieri et al. (2013), using XRD, AFM and trasmission electron microscopy (TEM), found critical ranges of thicknesses for ultra-thin $Ni_{52.5(9)}Mn_{19.5(7)}Ga_{28.0(5)}$ films deposited onto MgO at around 420 °C. Films with thicknesses below 40 nm remain in the austenitic phase. Films with thicknesses in the range from 40 nm to 100 nm contain, besides the austenite, also martensitic orthorhombic 14M variants with their c_{ortho14M} axes perpendicular to the film-substrate interface and in films with thicknesses above 100 nm, the variant of orthorhombic 14M martensite with the c_{ortho14M}-axis parallel to the interface can be then found as well.

Now let us present our findings on two series of samples with varying film thickness. Each series has different nominal composition, namely, $Ni_{47}Mn_{32}Ga_{21}$ and $Ni_{48}Mn_{30}Ga_{22}$, and their nominal thicknesses are in the range from 10 nm to 700 nm. The following spectra were acquired at room temperature.

7.2.1 Optical measurements in zero magnetic field

In all of the following diagonal relative permittivity tensor element spectra ε_{xx} in the zero magnetic field (Figs. 7.14 and 7.15), we can clearly observe a metallic behavior (see Fig. 2.1b) with two bound electron transitions at around the expected energies of 1.8 eV and 3.2 eV for the samples with thicknesses of 100 nm and above. For thinner samples, transition energies are notably higher. This energy shift can be easily identified in the $\operatorname{Re}\varepsilon_{xx}$ spectra.

First of all, the spectral changes with varying thickness seem to be much more dramatic compared to the temperature-induced spectral changes of the 400 nm thick $Ni_{47}Mn_{32}Ga_{21}$ sample discussed in Sec. 7.1.1. To be exact, due to the thickness variation in the range from 10 nm to 700 nm, $\operatorname{Re}\varepsilon_{xx}$ at the energies of 1.5 eV and 2.7 eV changes by approx. 30 and 10, respectively. As can be seen in Fig. 7.16, there is a correlation between the thickness dependences of $\operatorname{Re}\varepsilon_{xx}$ and of the out-of-plane lattice parameter $a_{\perp}$ of the $Ni_{50}Mn_{25}Ga_{25}$ composition series. Both $\operatorname{Re}\varepsilon_{xx}$ and $a_{\perp}$ increase with increasing thickness in the range from 10 nm to 50 nm until the constrained austenite is relaxed enough to allow the formation of the 14M martensite with its short axis c_{ortho14M} perpendicular to the film-substrate interface. However, between 50 nm and 100 nm, $\operatorname{Re}\varepsilon_{xx}$ continues to increase for energies below some critical energy E_c, e.g. at 1.5 eV (Fig. 7.16a), while for higher energies, e.g. at 2.7 eV (Fig. 7.16a), it decreases to the local minimum at 100 nm, following the $a_{\perp}$ trend. In our case, E_c is approx. 2.2 eV and 2.5 eV for the $Ni_{47}Mn_{32}Ga_{21}$ and $Ni_{48}Mn_{30}Ga_{22}$ composition series, respectively. This behavior was previously observed on thin films (Makeš, 2021) with the nominal stoichiometric composition $Ni_{50}Mn_{25}Ga_{25}$ and the critical energy of 1.8 eV. Interestingly enough, bulk $Ni_{50}Mn_{25}Ga_{25}$ spectra (Zhou et al., 2002) exhibit the same behavior when undergoing austenite to martensite transition with the critical energy of 1.2 eV.

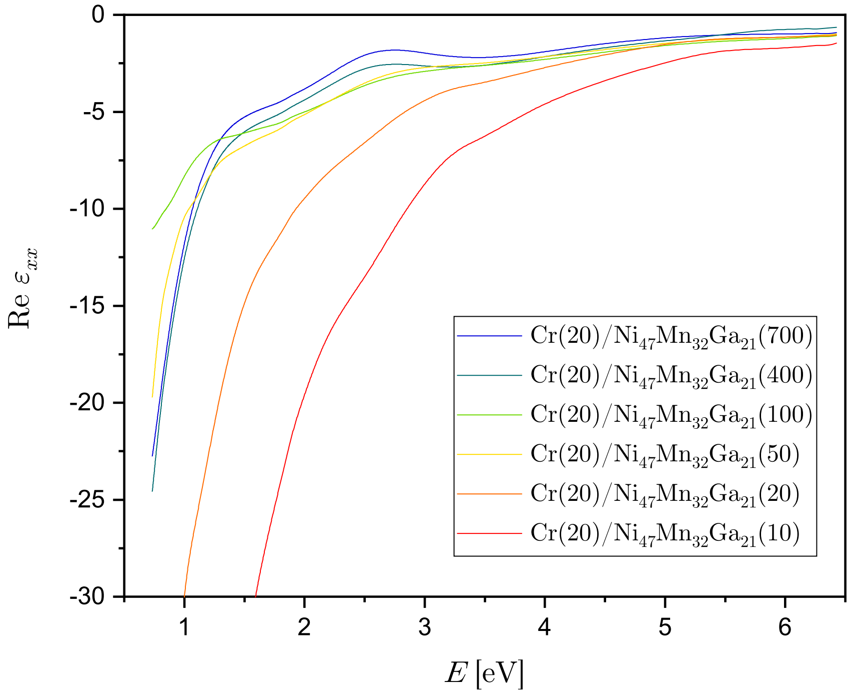

(a) $Ni_{47}Mn_{32}Ga_{21}$ composition series

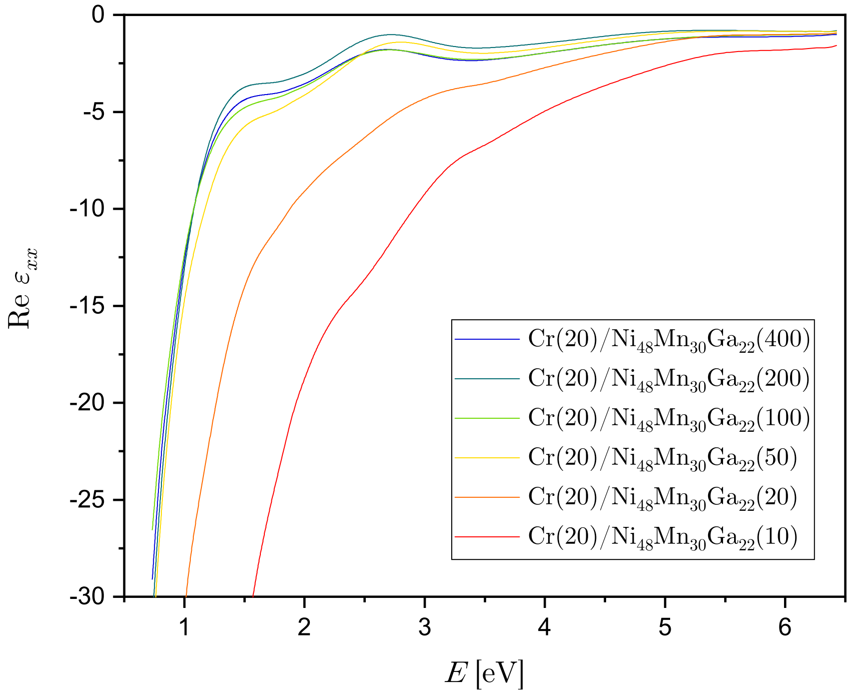

(b) $Ni_{48}Mn_{30}Ga_{22}$ composition series

Figure 7.14: Thickness dependence of the real part of the diagonal element of the relative permittivity tensor spectra for two different composition series of samples

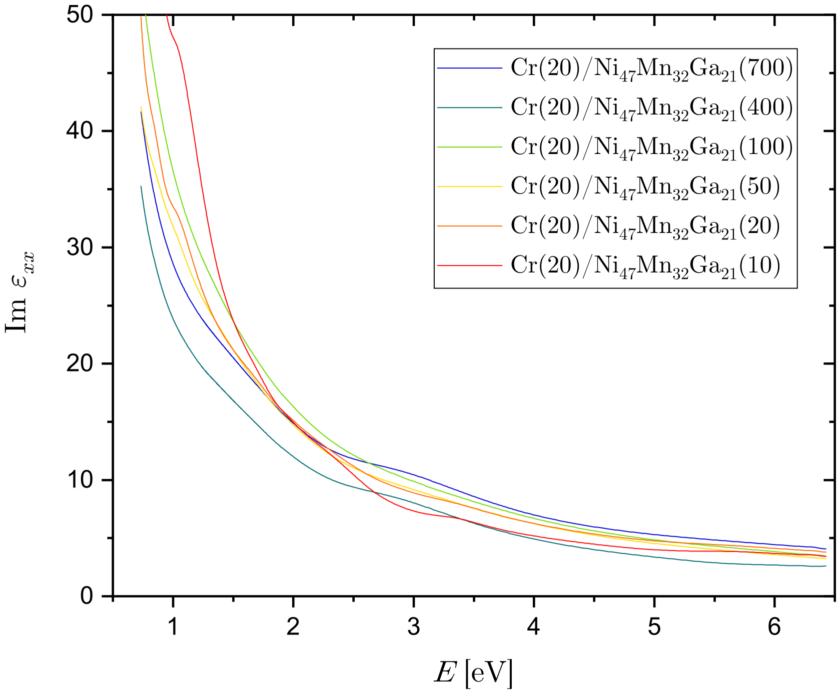

(a) $Ni_{47}Mn_{32}Ga_{21}$ composition series

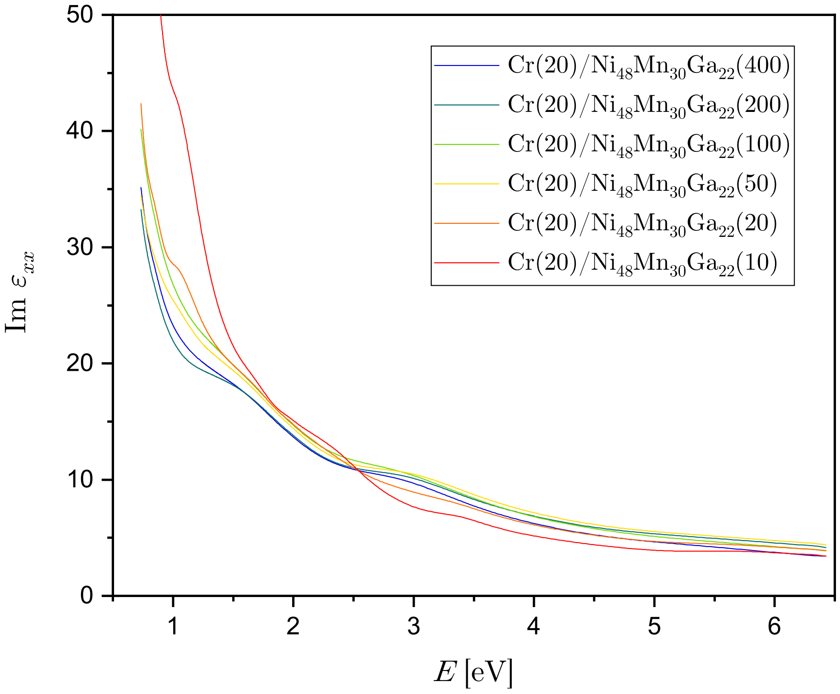

(b) $Ni_{48}Mn_{30}Ga_{22}$ composition series

Figure 7.15: Thickness dependence of the imaginary part of the diagonal element of the relative permittivity tensor spectra for two different composition series of samples

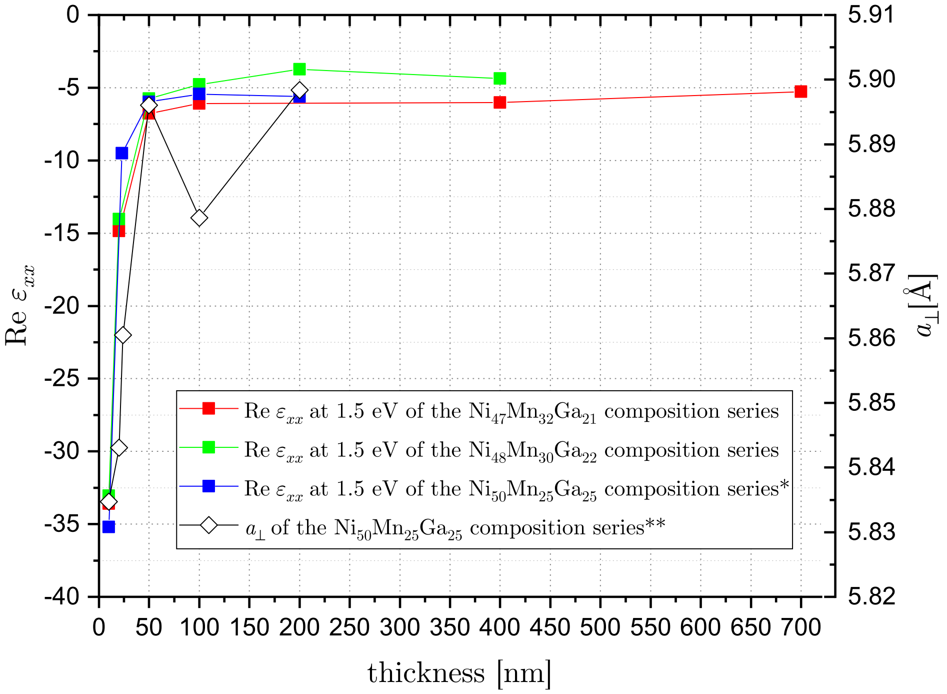

(a) at 1.5 eV

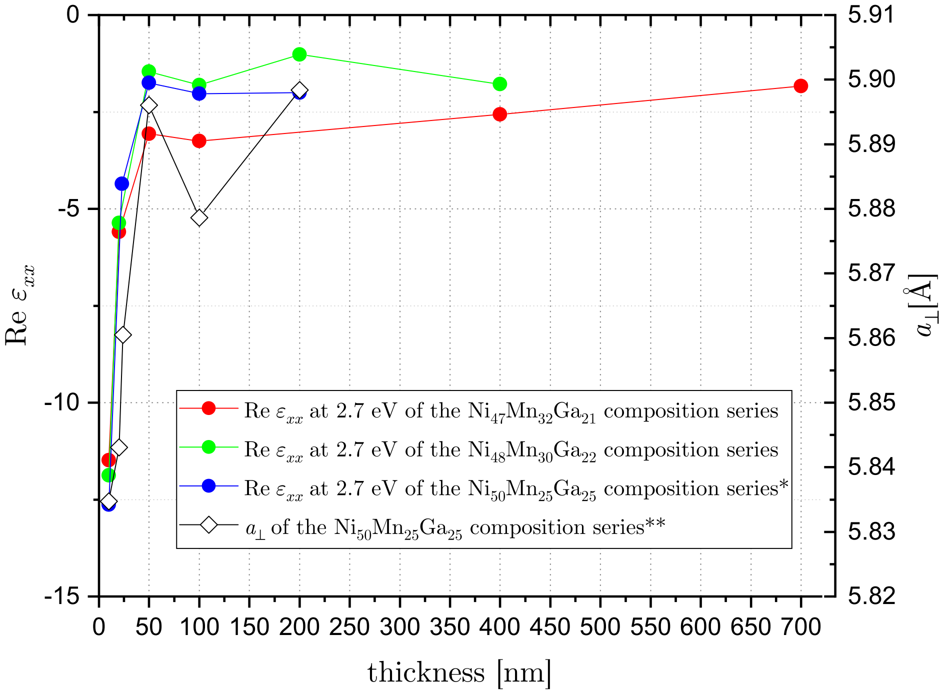

(b) at 2.7 eV

Figure 7.16: Thickness dependence of $\operatorname{Re}\varepsilon_{xx}$ for three different composition series. * marks the data extracted from Makeš (2021), and its XRD measurements (**) of the out-of-plane lattice parameters $a_\perp$ were provided by Heczko (2023).

7.2.2 Magneto-optical measurements in polar geometry

The following polar MOKE spectra (Figs. 7.17 and 7.18) were measured earlier using a different spectrometer (see Sec. 6.2) without a thermoelectric cooling device, thus exhibiting a higher level of noise. Irrespective of the exact thickness and composition, the previously identified Kerr azimuth spectral structure, characterized by two positive peaks and a positive valley in between for lower energies and one broad and high-magnitude negative peak at higher energies, is still recognizable.

On the other hand, we can notice much more dramatic spectral changes caused by the thickness variation as opposed to the temperature-induced spectral changes of the 400 nm $Ni_{47}Mn_{32}Ga_{21}$ in the 20 °C to 70 °C range (see Sec. 7.1.2). For a more rigorous analysis of the Kerr azimuth peak energy shift, the 2nd order polynomial was fitted to the data in the vicinity of the extremum using the Savitzky-Golay method and the corresponding energy obtained by computing the first derivative. Subsequently, in Fig. 7.19, we can see that the thickness dependence of the Kerr azimuth peak energy is strongly (negatively) correlated to the thickness dependence of the out-of-plane lattice parameter as the constrained austenite relaxes up to the critical thickness of 50 nm. The 3rd peak (Fig. 7.19c) is being shifted the most (by about 0.6 eV to 0.8 eV) between 10 nm and 50 nm and its overall thickness dependence fits to the out-of-plane lattice parameter trend the best. Beyond 50 nm, the peak energy changes are much smaller. It is important to note that the MOKE spectral peak energies and their thickness dependeces imperfectly reflect the underlying changes in the magneto-optical transitions. In order to gain a better insight into the nature of the observed spectral changes, one would need to employ a microscopic theory, like the one introduced in Sec. 2.4, to find the specific magneto-optical transitions and their parameters.

Besides the Kerr azimuth peak energy shift, there is also a relative magnitude change between the 1st and 2nd peak. In bulk spectra (Beran et al., 2015), this change was associated to the martensitic tranformation, where in the case of austenite, the 2nd peak was higher, and in the case of 10M martensite, the 1st peak was higher. In our case, the 2nd peak is higher for samples with thicknesses in the range from 10 nm to 50 nm, and in the range from 100 nm to 700 nm, it is the other way around. More specifically, as we can see in Fig. 7.20, the linear interpolations of the 1st and 2nd peak magnitude trends cross each other at approx. 40 nm (Fig. 7.20a) in the $Ni_{47}Mn_{32}Ga_{21}$ case and at approx. 80 nm (Fig. 7.20b) in the $Ni_{48}Mn_{30}Ga_{22}$ case. On the $Ni_{50}Mn_{25}Ga_{25}$ composition series (Makeš, 2021), the crossing was observed at approx. 50 nm. Examining the behavior of each peak magnitude individually, we see that the 1st peak magnitude has an increasing trend (Fig. 7.21a) for lower thicknesses. At the local minimum of $a_\perp$ at 100 nm, depending on the composition series, there is either no local minimum whatsoever or a very shallow one. However, the thickness dependences of the 2nd and 3rd peak magnitudes (Figs. 7.21b and 7.21c) clearly follow the $Ni_{50}Mn_{25}Ga_{25}$ out-of-plane lattice parameter trend with pronounced local minima at 100 nm.

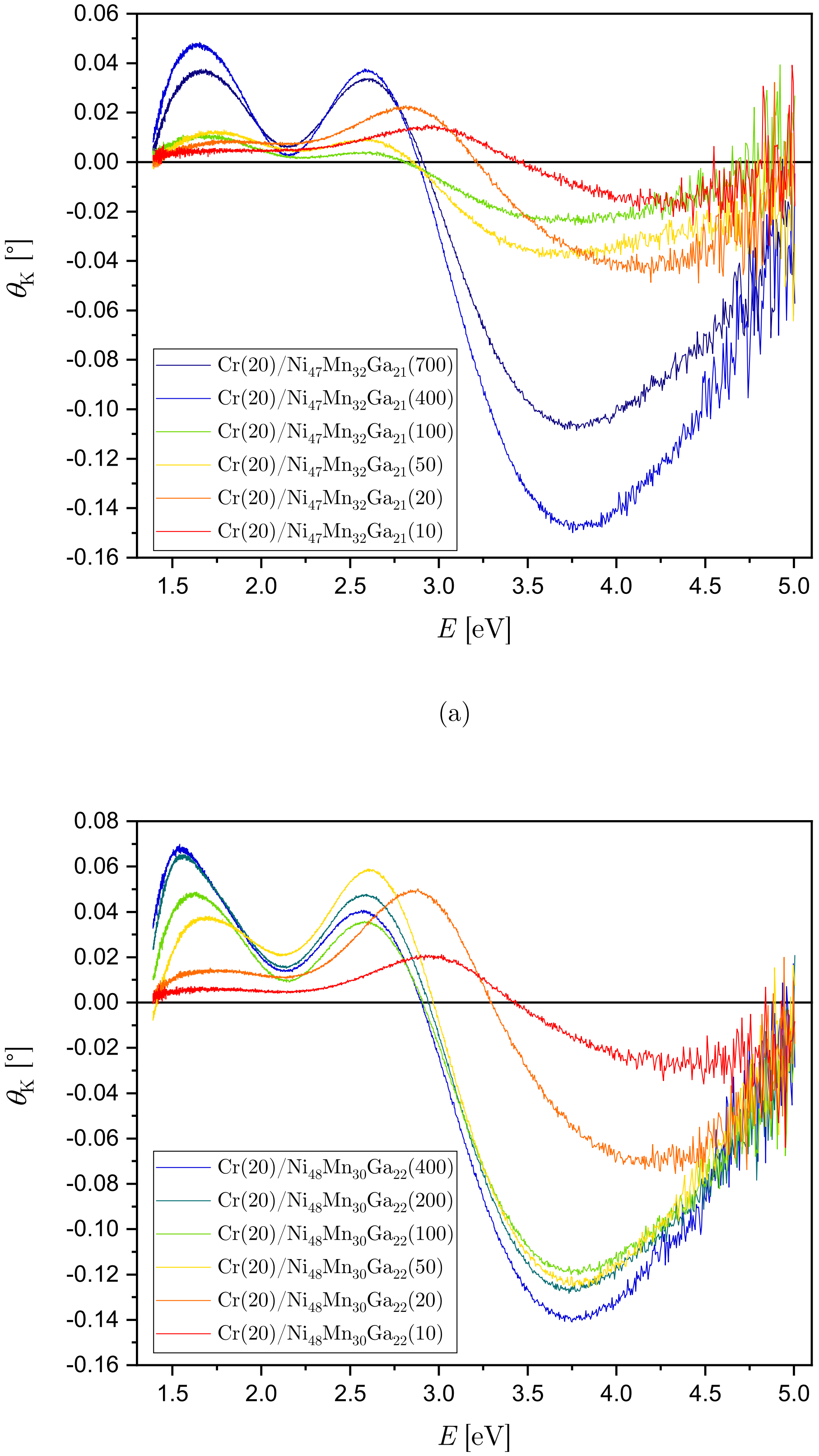

(a)

(b)

Figure 7.17: Thickness dependence of the Kerr azimuth spectra in polar geometry of the $Ni_{47}Mn_{32}Ga_{21}$ (a) and $Ni_{48}Mn_{30}Ga_{22}$ (b) composition series of samples.

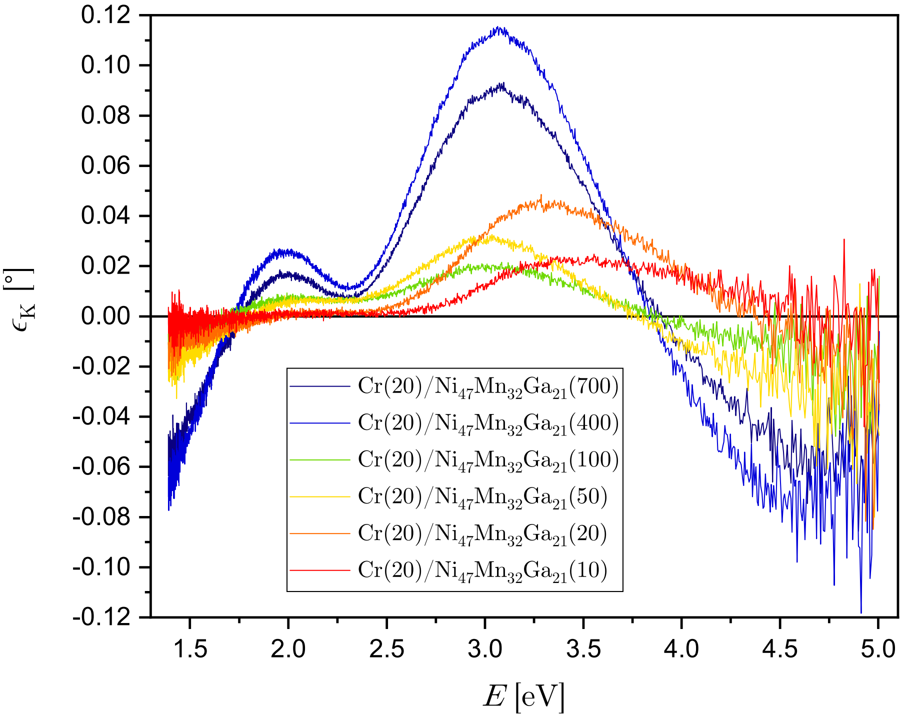

(a)

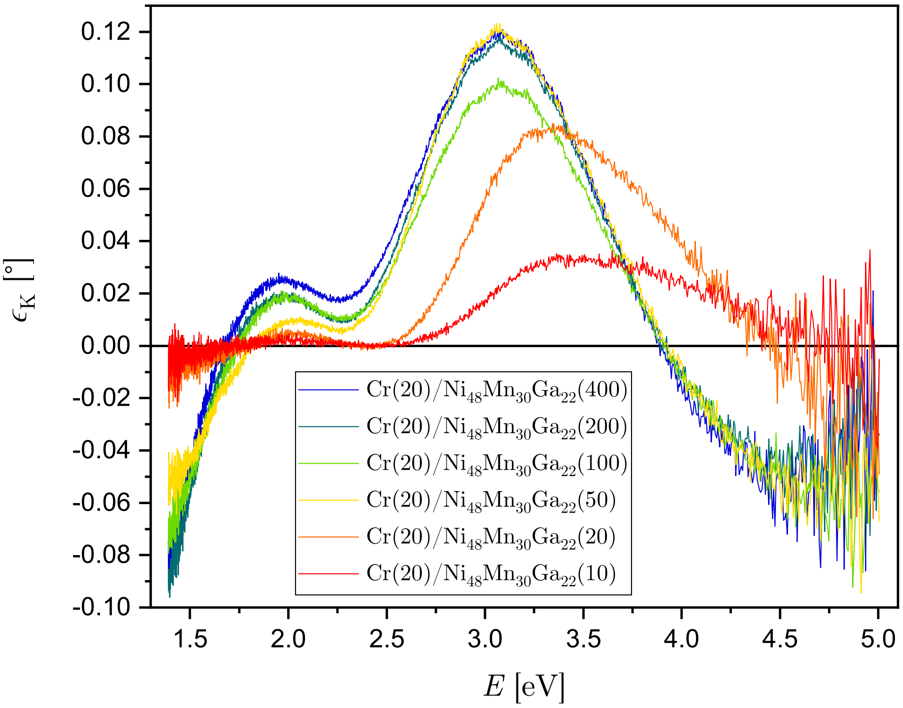

(b)

Figure 7.18: Thickness dependence of the Kerr ellipticity spectra in polar geometry of the $Ni_{47}Mn_{32}Ga_{21}$ (a) and $Ni_{48}Mn_{30}Ga_{22}$ (b) composition series of samples.

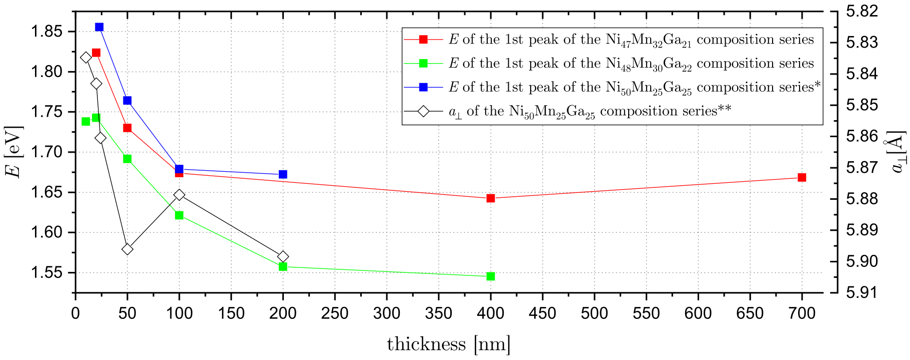

(a) the 1st peak

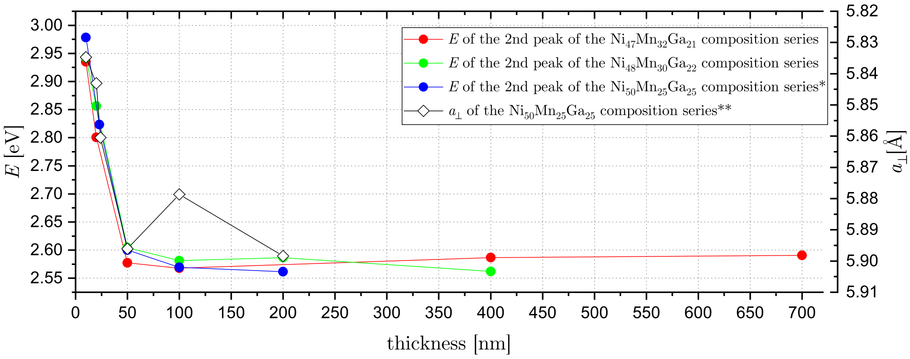

(b) the 2nd peak

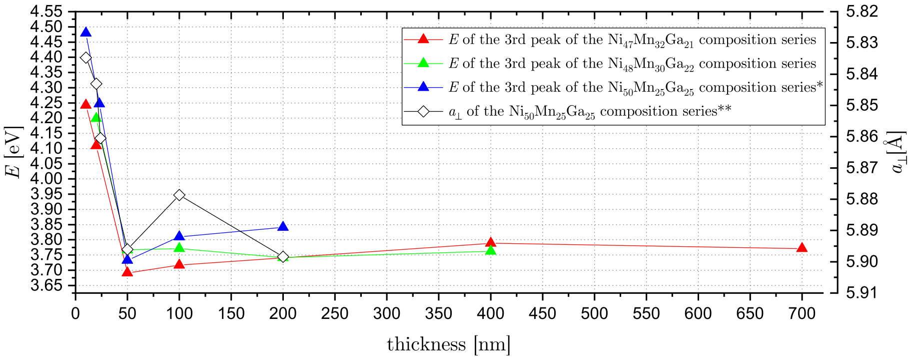

(c) the 3rd peak

Figure 7.19: Thickness dependence of the polar Kerr azimuth peak energy E for three different composition series. * marks the data extracted from Makeš (2021), and its XRD measurements (**) of the out-of-plane lattice parameters $a_\perp$ were provided by Heczko (2023).

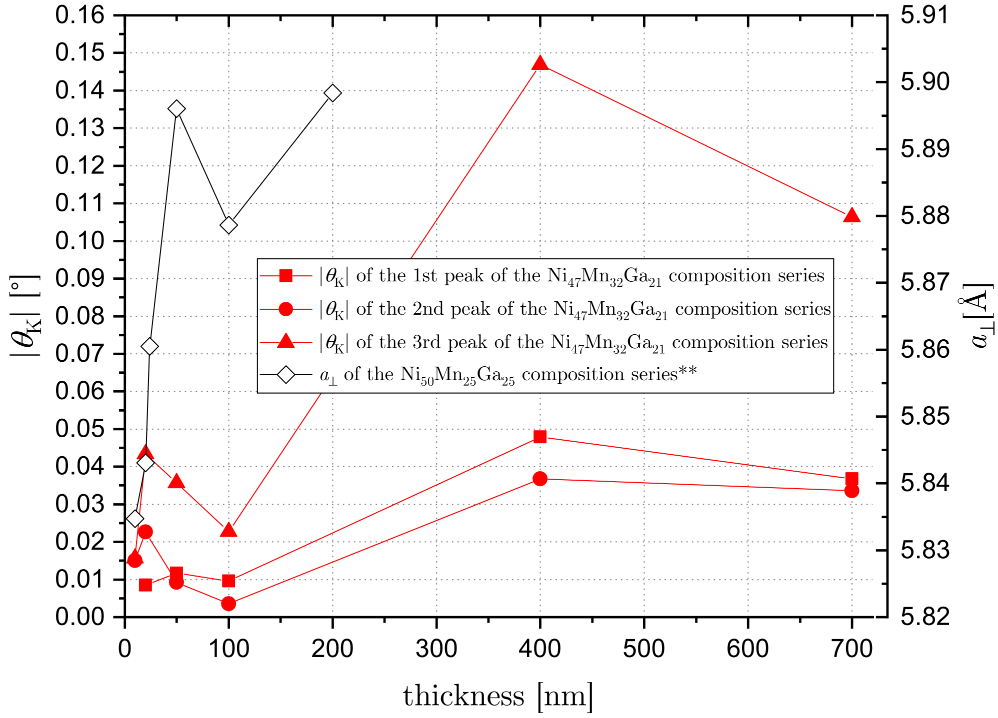

(a) $Ni_{47}Mn_{32}Ga_{21}$ composition series

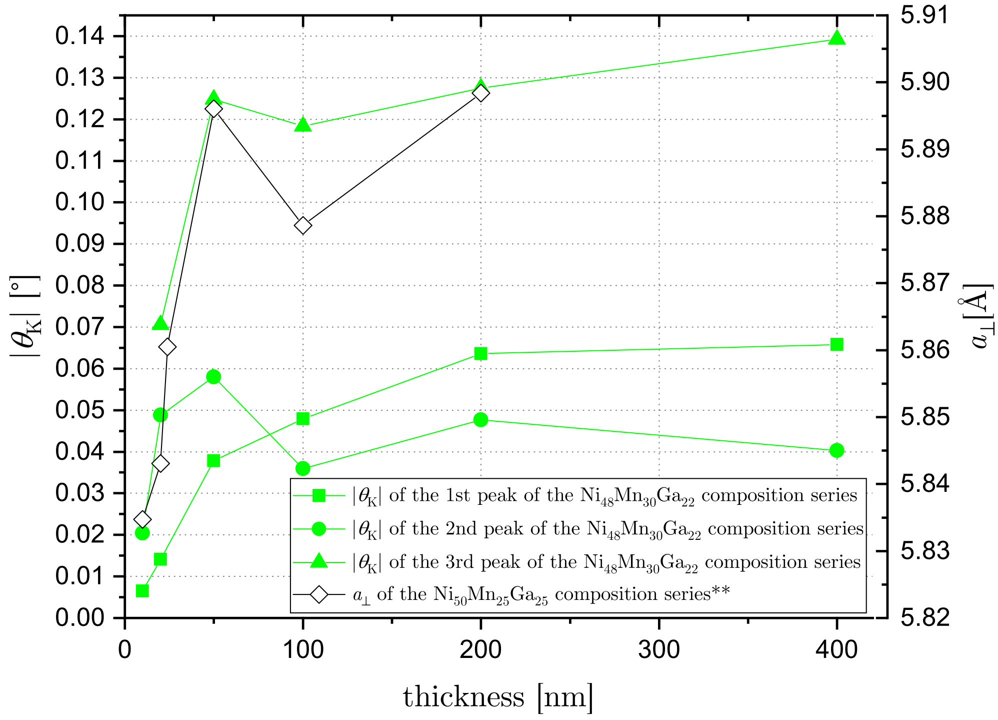

(b) $Ni_{48}Mn_{30}Ga_{22}$ composition series

Figure 7.20: Thickness dependence of the polar Kerr azimuth peak magnitude $|\theta_K|$ for two different composition series. XRD measurements (**) of the $Ni_{50}Mn_{25}Ga_{25}$ out-of-plane lattice parameters $a_\perp$ were provided by Heczko (2023).

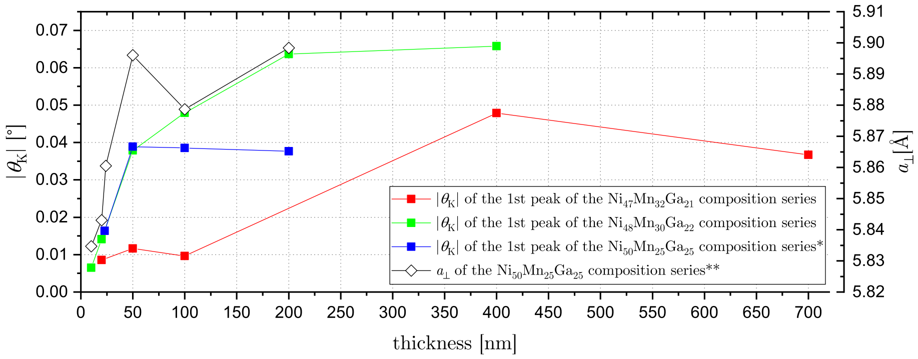

(a) the 1st peak

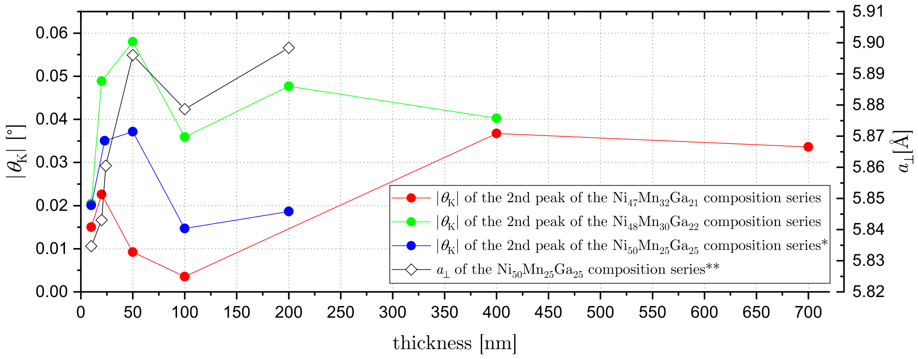

(b) the 2nd peak

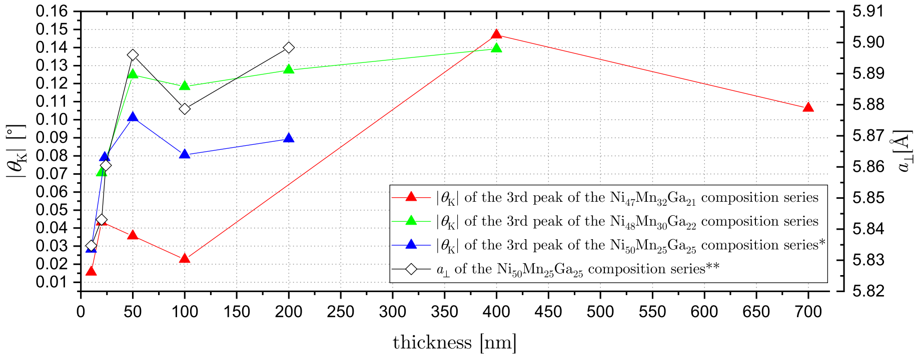

(c) the 3rd peak

Figure 7.21: Thickness dependence of the polar Kerr azimuth peak magnitude $|\theta_K|$ for the $Ni_{47}Mn_{32}Ga_{21}$, $Ni_{48}Mn_{30}Ga_{22}$ and $Ni_{50}Mn_{25}Ga_{25}$ composition series. * marks the data extracted from Makeš (2021), and its XRD measurements (**) of the out-of-plane lattice parameters $a_\perp$ were provided by Heczko (2023).

Conclusion

Numerous optical spectroscopic measurements were performed, both in zero magnetic field and in the out-of-plane (polar) magnetic field configuration, to study the optical and magneto-optical responses of thin Ni-Mn-Ga films, epitaxially grown on the stress-mediating Cr layer and the MgO substrate. From the acquired ellipsometric data within the spectral range from 0.7 eV to 6.4 eV, relative permittivity tensor spectra were computed via regression analyses. Spectral changes were studied in two distinct situations. One of them was a thermally-induced martensitic transformation of a 400 nm thick $Ni_{47}Mn_{32}Ga_{21}$ film in a temperature range from 20 °C to 70 °C. The other situation was a thickness variation of $Ni_{47}Mn_{32}Ga_{21}$ and $Ni_{48}Mn_{30}Ga_{22}$ sample series at room temperature in a thickness range from 10 nm to 700 nm.

Our results agree with previously published studies by exhibiting two apparent bound electron transitions roughly at the energies of 1.8 eV and 3.2 eV. The polar magneto-optical Kerr effect spectra resemble those reported on bulk as well as on epitaxial films.

At several selected energies, temperature dependeces across the phase transition of the 400 nm thick $Ni_{47}Mn_{32}Ga_{21}$ film showed various hysteresis shapes, which were compared to the magnetization curve of this film. The polar magneto-optical Kerr effect and the off-diagonal relative permittivity tensor elements were found to behave in almost identical manner, yet the off-diagonal element spectra will be indispensible for future analyses of the magneto-optical transitions using a microscopic theory.

The thickness-varied spectra exhibit a significant shift of the spectral structures to higher energies for the thinnest of samples. A critical thickness of 50 nm was identified, at which there is a change in the thickness trends. At selected energies or at spectral peaks, these trends were compared to X-ray diffraction measurements of the out-of-plane lattice parameter and a strong correlation was found.

Bibliography

R. M. A. Azzam and N. M. Bashara. *Ellipsometry and Polarized Light.* North-Holland, 1977. ISBN 0720406943,9780720406948.

A. Backen, S. R. Yeduru, M. Kohl, S. Baunack, A. Diestel, B. Holzapfel, L. Schultz, and S. Fähler. Comparing properties of substrate-constrained and freestanding epitaxial Ni–Mn–Ga films. *Acta Materialia*, 58(9):3415–3421, 2010. ISSN 1359-6454. doi: https://doi.org/10.1016/j.actamat.2010.02.016.

L. Beran, P. Cejpek, M. Kulda, R. Antoš, V. Holý, M. Veis, L. Straka, and O. Heczko. Optical and magneto-optical studies of martensitic transformation in Ni-Mn-Ga magnetic shape memory alloys. *Journal of Applied Physics*, 117 (17):17A919, 2015.

M. Born and E. Wolf. *Principles of optics.* Cambridge University Press, 7th edition, 1999. ISBN 9780521642224,0521642221.

P. J. Brown, J. Crangle, T. Kanomata, M. Matsumoto, K. Neumann, B. Ouladdiaf, and K. R. A. Ziebeck. The crystal structure and phase transitions of the magnetic shape memory compound Ni_2MnGa. *Journal of Physics: Condensed Matter*, 14(43):10159, 2002.

V. A. Chernenko, E. Cesari, V. V. Kokorin, and I. N. Vitenko. The development of new ferromagnetic shape memory alloys in Ni-Mn-Ga system. *Scripta metallurgica et materialia*, 33(8):1239–1244, 1995.

A. Dejneka, V. Zablotskii, M. Tyunina, L. Jastrabik, J. I. Pérez-Landazábal, V. Recarte, V. Sánchez-Alarcos, and V. A. Chernenko. Ellipsometry applied to phase transitions and relaxation phenomena in Ni_2MnGa ferromagnetic shape memory alloy. *Applied Physics Letters*, 101(14):141908, 10 2012. ISSN 0003-6951. doi: 10.1063/1.4757393.

P. Entel, V. D. Buchelnikov, V. V. Khovailo, A. T. Zayak, W. A. Adeagbo, M. E. Gruner, H. C. Herper, and E. F. Wassermann. Modelling the phase diagram of magnetic shape memory Heusler alloys. *Journal of Physics D: Applied Physics*, 39(5):865, 2006.

C. Felser and A. Hirohata. *Heusler Alloys*, volume 222. Springer, 2015.

O. Heczko. Magnetic shape memory effect and highly mobile twin boundaries. *Materials Science and Technology*, 30(13):1559–1578, 2014.

O. Heczko. XRD measurements of the out-of-plane lattice parameters. Samples J013, J015, J016, J017, J018, December 2023.

J. N. Hilfiker and H. G. Tompkins. *Spectroscopic ellipsometry : practical application to thin film characterization.* Materials characterization and analysis collection. Momentum Press, 2016. ISBN 1606507273,978-1-60650-727-8,978-1-60650-728-5.

F. J. Kahn, P. S. Pershan, and J. P. Remeika. Ultraviolet magneto-optical properties of single-crystal orthoferrites, garnets, and other ferric oxide compounds. *Physical review*, 186(3):891, 1969.

S. Ö. Kart, M. Uludoğan, I. Karaman, and T. Çağın. DFT studies on structure, mechanics and phase behavior of magnetic shape memory alloys: Ni_2MnGa. *physica status solidi (a)*, 205(5):1026–1035, 2008.

C. N. Koumelis. The thermal expansion coefficient of chromium in the temperature region of 3 to 80 °C. *physica status solidi (a)*, 19(1):K65–K69, 1973. doi: https://doi.org/10.1002/pssa.2210190157.

H. A. Lorentz. The absorption and emission lines of gaseous bodies. In *Knaw, Proceedings*, volume 8, pages 1905–1906, 1906.

M. Makeš. *Optická a magnetooptická spektroskopie tenkých vrstev NiMnGa s martenzitickou transformací.* Bachelor's thesis, Charles University. Faculty of Mathematics and Physics. Institute of Physics, Prague, 2021.

P. Malý and F. Trojánek. *Laserová fyzika a nelineární optika.* MatfyzPress, Prague, 1st edition, 2022. ISBN 978-80-7378-461-4.

V. V. Martynov and V. V. Kokorin. The crystal structure of thermally-and stress-induced martensites in Ni_2MnGa single crystals. *Journal de Physique III*, 2(5): 739–749, 1992.

S. Miyazaki, Y.Q. Fu, and W.M. Huang. *Thin Film Shape Memory Alloys: Fundamentals and Device Applications.* Cambridge University Press, 1 edition, 2009. ISBN 0521885760,9780521885768.

M. Nývlt. *Optical interactions in ultrathin magnetic film structures.* PhD thesis, Charles University. Faculty of Mathematics and Physics. Institute of Physics, Prague, 1996.

K. Onderková. *Martensitické mikrostruktury v tenkých vrstvách a objemových monokrystalech Heuslerových slitin Ni-Mn-Ga.* Master's thesis, Charles University. Faculty of Mathematics and Physics, Department of Surface and Plasma Science, Prague, 2020.

P. Ranzieri, S. Fabbrici, L. Nasi, L. Righi, F. Casoli, V. A. Chernenko, E. Villa, and F. Albertini. Epitaxial Ni–Mn–Ga/MgO (1 0 0) thin films ranging in thickness from 10 to 100 nm. *acta Materialia*, 61(1):263–272, 2013.

A. Sozinov, N. Lanska, A. Soroka, and W. Zou. 12% magnetic field-induced strain in Ni-Mn-Ga-based non-modulated martensite. *Applied Physics Letters*, 102(2):021902, 2013.

M. Thomas, O. Heczko, J. Buschbeck, U. K. Rößler, J. McCord, N. Scheerbaum, L. Schultz, and S. Fähler. Magnetically induced reorientation of martensite variants in constrained epitaxial Ni–Mn–Ga films grown on MgO (001). *New Journal of Physics*, 10(2):023040, 2008a.

M. Thomas, O. Heczko, J. Buschbeck, L. Schultz, and S. Fähler. Stress induced martensite in epitaxial Ni–Mn–Ga films deposited on MgO (001). *Applied Physics Letters*, 92(19), 2008b.

K. Ullakko, J. K. Huang, C. Kantner, R. C. O'handley, and V. V. Kokorin. Large magnetic-field-induced strains in Ni_2MnGa single crystals. *Applied Physics Letters*, 69(13):1966–1968, 1996.

A. N. Vasil'ev, V. D. Buchel'nikov, T. Takagi, V. V. Khovailo, and E. I. Estrin. Shape memory ferromagnets. *Physics-Uspekhi*, 46(6):559, jun 2003. doi: 10.1070/PU2003v046n06ABEH001339.

M. Veis, L. Beran, M. Zahradník, R. Antoš, L. Straka, J. Kopeček, L. Fekete, and O. Heczko. Magneto-optical spectroscopy of ferromagnetic shape-memory Ni-Mn-Ga alloy. *Journal of Applied Physics*, 115(17):17A936, 2014.

C. Verbeno. Magnetometry measurement. Sample J058, 2021.

Š. Višňovský. Magneto-optical ellipsometry. *Czechoslovak journal of physics*, 36 (5), 1986. ISSN 0011-4626.

Š. Višňovský. *Optics in Magnetic Multilayers and Nanostructures.* Optical Science and Engineering. CRC Press, 1 edition, 2006. ISBN 9780849336867,0849336864.

P. J. Webster, K. R. A. Ziebeck, S. L. Town, and M. S. Peak. Magnetic order and phase transformation in Ni_2MnGa. *Philosophical Magazine B*, 49(3):295–310, 1984.

F. Wooten. *Optical Properties of Solids.* Academic Press, 1972. ISBN 978-0-12-763450-0.

P. Yeh. Optics of anisotropic layered media: A new 4 × 4 matrix algebra. *Surface Science*, 96(1):41–53, 1980. ISSN 0039-6028. doi: https://doi.org/10.1016/0039-6028(80)90293-9.

P. Yeh. *Optical Waves in Layered Media.* Wiley-Interscience, 2 edition, 2005. ISBN 0471731927,9780471731924.

Y. Zhang, J. R. G. Evans, and S. Yang. Corrected values for boiling points and enthalpies of vaporization of elements in handbooks. *Journal of Chemical & Engineering Data*, 56(2):328–337, 2011.

Y. Zhou, X. Jin, H. Xu, Y. V. Kudryavtsev, Y. P. Lee, and J. Y. Rhee. Influence of structural transition on transport and optical properties of Ni_2MnGa alloy. *Journal of applied physics*, 91(12):9894–9899, 2002.

A. K. Zvezdin and V. A. Kotov. *Modern Magnetooptics and Magnetooptical Materials.* Condensed Matter Physics. Institute of Physics Publishing, 1 edition, 1997. ISBN 075030362X,9780750303620.

List of Figures

List of Tables